MSc. Thesis
Electrical Engineering
Track: Telecommunications
Delft University of Technology

"The impact of droplets' clustering on the radar backscattering from water clouds"

Athina Argyrouli

July 2012

The impact of droplets' clustering on the radar backscattering from water clouds

BY

Athina Argyrouli

THESIS

submitted in partial fulfillment of the
requirements for the degree of

MASTER OF SCIENCE

in

ELECTRICAL ENGINEERING

Remote Sensing of the Environment
Department of Telecommunication
Faculty EEMCS, Delft University of Technology
Delft, the Netherlands

Supervised by:

Dr. Neil Budko
Prof. dr. Herman W. J. Russchenberg
MSc. Christine M. H. Unal

Delft University of Technology
Mekelweg 4
2628 CD Delft
The Netherlands

Abstract

The goal of this thesis is to investigate the clustering effect of droplets in the water clouds. The initial motivation came from the incapability of millimeter-wave cloud radars to always detect low-level liquid water clouds. The observed discrepancy between the value of radar reflectivity factor estimated by radar measurements and the theoretical one predicted by the standard radar scattering theory set under question the applicability of the incoherent Rayleigh scattering assumption in the case of backscattering from water clouds. A possible reason for the violation of the assumption for incoherent Rayleigh scattering is the formation of clusters inside the cloud volume, which behave as coherent structures. Droplets' clustering has been investigated through three cases: droplets inside the cloud volume totally correlated form one cluster; droplets inside the cloud volume partially correlated form more than one cluster; droplets inside the cloud volume completely uncorrelated do not form any cluster.

The patterns of radar backscattered electric field were visualised in the complex plane by using the Random Walks approach which is a tool for studying the statistical properties of electromagnetic waves backscattered by objects containing few scattering centers. To simulate turbulence inside the cloud volume, four different types of motion for the clusters were introduced. Thus, the turbulence model allows the clusters to shift either horizontally, vertically, towards any direction in 3-dimensional space or rotate about a vertical central axis. The induced velocity and acceleration define clusters' maximum displacement. The particular motions characterized by the maximum displacement, denote various length scales and intensities of turbulence. The impact of these motions on the pattern of backscattered electric field is investigated for the case of totally correlated droplets which form a single cluster.

Low degrees of clustering are explored through the patterns of the radar backscattered electric field, but also from the distribution of power resulting from the coherent summation of the individual backscattered fields. The computational tests showed that the probability density function of coherent power backscattered by n=1, 2, 3 clusters is consistent with the probability density function of the distance from the origin in a single-, two-, three-step isotropic Pearson's random walk over the two-dimensional phase space respectively. Clusters have been considered in alignment to X-axis, Y-axis, Z-axis or randomly arranged in the cloud volume. An analysis on the statistical properties of the backscattered electric field for different arrangements of clusters inside the cloud volume is presented.

The computational results of this research showed that the clustering of droplets results in a radar response which deviates from the one predicted by the standard radar theory. The probability density function of the power backscattered by partially correlated droplets differs from the well-known exponential distribution of completely uncorrelated droplets in the absence of clustering. The systematic discrepancies between the mean coherent and incoherent power imply that radar reflectivity sensitivity of cloud radars may not be sufficient for detecting backscattered signals from water clouds.

Keywords: droplets' clustering; droplets' spatial correlation; radar discrepancy; millimeter-wave cloud radar; Pearson's random walk; coherent radar backscatter; water clouds.

Acknowledgments

The credit of this work goes to the people who were supporting me during my thesis and inspired me to accomplish it. First and foremost, I offer my sincerest gratitude to my supervisor, Dr. Neil Budko, who was leading me to the proper direction throughout my thesis whilst allowing me the room to work in my own way. I attribute the level of my Masters degree to his encouragement and effort and without him this thesis would not have been completed.

Many thanks to my professor Dr. Herman W. J. Russchenberg, chair of the Remote Sensing of the Environment group. Early in the first year of the MSc. program, his lectures initially stimulated my interest for remote sensing. Later, he brought me in contact with Dr. Arnoud Apituley from the Royal Netherlands Meteorological Institute (KNMI) where I did my internship and I got to love more the application of remote sensing on weather and climate studies. Furthermore, he gave me the opportunity to work in the collaboration project Climate City Campus where I developed organisational skills and I had the chance to interact with researchers and students from all faculties of TUDelft. Finally, during my graduation project, he had the overall supervision of my progress and highlighted the core elements consisting a complete project research.

I am grateful to the researcher Christine Unal, who devoted a lot of time to my work and took care of the content and the quality of the report. Throughout my thesis-writing period, she provided encouragement, sound advice and lots of good ideas. Her thorough insight of my work and her regular feedback helped me to significantly improve my final report. I would have been lost without her.

I am indebted to my student colleagues for providing a stimulating and fun environment in which I have learned and grown. In my daily thesis work I have been blessed by the friendly and cheerful group of Geosciences and Remote Sensing. In particular, I am thankful to the Ph.D. student Simone Placidi, who was my officemate and he was motivating me throughout the project.

Last but not least, I want to thank my family who encouraged my decision to study abroad and they were mentally supporting me, regardless the distance. My fianc, Christos Vezyris, was standing by me all this period and helped me to overcome all the difficulties arose during the MSc. program. He was critical about my work and his comments were useful for improving the presentation of my results. I am also thankful to all of my friends, from both Greece and the Netherlands, who were giving me strength and motivation to work hard. There are no words to thank them enough for all the encouragement.

Contents

List of Figures

List of Tables

1 Introduction

Pictures of our planet taken from space show that Earth consists mostly of clouds and oceans. In particular, clouds, covering 60% - 70% of the globe at any given time, are considered as controlling components of Earth's climate. Clouds functioning as modulators of the radiative transfer in the atmosphere are effective on maintaining the Earth's energy balance. Some clouds have a cooling effect, other ones a warming effect. Their influence on the radiative budget of the Earth depends on their macrophysical and microphysical properties. Cloud structure (i.e., macrophysical and microphysical properties) can be investigated by combining different radar measurements.

1.1 The use of radar for atmospheric cloud research

Radars are widely used for extracting useful information about cloud properties. The appropriate instrument or combination of instruments is pertinent to the feature that needs to be measured. The cloud type and macrophysical properties of the cloud, such as cloud thickness and cloud boundaries (i.e., cloud base and cloud top), can be investigated by the synergy of different remote sensors [Wang and Sassen, 2001]. To study the radiative properties of clouds, their micro physical properties should be retrieved. The microphysical properties include estimating the size, shape and phase of the individual cloud particles as well as the particle concentration. These parameters can be estimated mainly by RADARs (Radio Detection and Ranging), rather than LIDARs (Light Detection and Ranging) which are less suitable for measuring cloud microphysical properties because they do not penetrate into the optically thick clouds. The choice of the operating wavelength for the most suitable radar can be made after classifying cloud types and their relevant properties, like the range of their particles' effective radius.

Right after the end of World War II, radars have been used for meteorological applications. The first meteorological radars were operating at centimeter (1-10cm) wavelengths. However, the centimeter-wavelength radar was not sufficient for detecting small cloud particles with diameter in the range of 5-10μm. For the detection of such small cloud particles, radars operating in shorter wavelengths have been required. Thus, millimeter-wavelength radars were developed and they became widely used for predicting precipitation storms and also detecting non-precipitating clouds. Millimeter-wave cloud radars (MMCR) have high temporal and spatial resolutions and they function with antennas which generate nar-

row beamwidths and limited sidelobes.Their portability and compact size are advantageous features that make them suitable for ground-based platforms but also airborne and spaceborne platforms. The MMCR is a vertically pointing Doppler weather radar that operates at a frequency of 35 GHz. Since 1987, when the first 94-GHz Doppler radar (Figure 1.1) was developed by Roger Lhermitte at the University of Miami, it remains as the highest frequency (W-band) meteorological radar in use [Kollias et al., 2007].

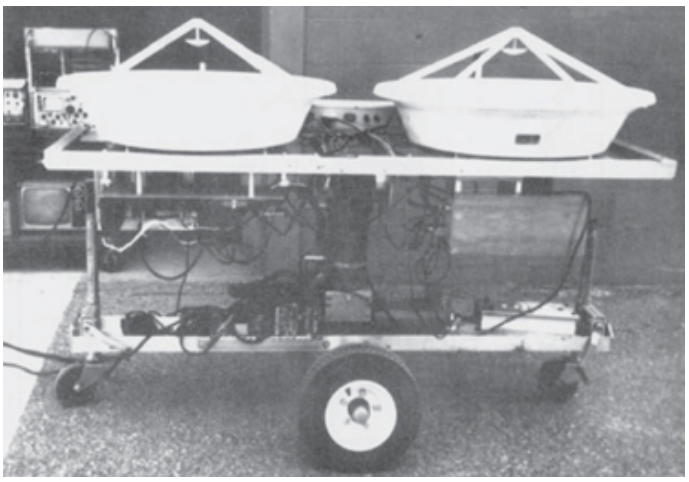

Figure 1.1: *Picture of the first 94-GHz Doppler radar designed by Roger Lhemitte at the University of Miami*

1.1.1 Water clouds

Among the various type of clouds, which differ upon their base altitude, horizontal and vertical extend and lifecycle, the current study is limited to water clouds. The reason why water clouds are investigated in this research is because they are very common and there is still uncertainty on how to measure their properties accurately. Their frequent appearance above the globe has an influence in the global radiative energy balance and makes the retrieval of their microphysical properties a challenging task for the cloud scientists. Furthermore, due to the fact that water clouds are located lower in the atmosphere (i.e., lowest level of troposphere), they can be more easily observed by ground-based instruments compared to the upper-tropospheric clouds (e.g., cirrus). Water clouds are certainly treated as low-level clouds (i.e., $\lesssim 3km$ height in the atmosphere). Therefore, the low-level liquid water clouds contain exclusively liquid water droplets and this feature simplifies the implied physics. However, ice clouds containing both liquid water drops and ice crystals need more complicated scattering methodologies to be studied. This is pretty straightforward if one thinks under which conditions Mie theory is valid. Indeed, since Mie scattering describes the scattering of electromagnetic radiation by a sphere, its validity is satisfied only if spherical droplets are assumed [Turner et al., 2007]. This is a good assumption for cloud water droplets.

Water clouds are mainly measured by radars. In particular, from the available radars used in meteorology, MMCRs are the most appropriate radars for detecting particles of water clouds because they are sensitive to small cloud particles. In general, water clouds are non-precipitating and they might produce precipitation only over oceans. However, it is common that the radar measurements are combined with measurements from microwave radiometer (MWR)[1] and, sometimes, also the synergy of a radar, a MWR and a lidar is required for extracting simultaneously different cloud properties[2] [Erkelens et al., 1999], [Venema, 2000].

[1] The difficulty to retrieve the microphysical properties of a water cloud arises because the radar measures a moment of the Doppler velocity distribution which is proportional to the sixth power of droplet diameter and not directly to the diameter. In some situations, this difficulty can be overcome by combining a vertically pointing millimeter-wave radar and a MWR [Frisch et al., 1999], [Erkelens et al., 1999].

[2] During CLARA campaign, for the retrieval of the cloud top, cloud base and LWP of a stratocumulus cloud, a radar, a lidar and a MWR were operating at the same time [Boers et al., 2000].

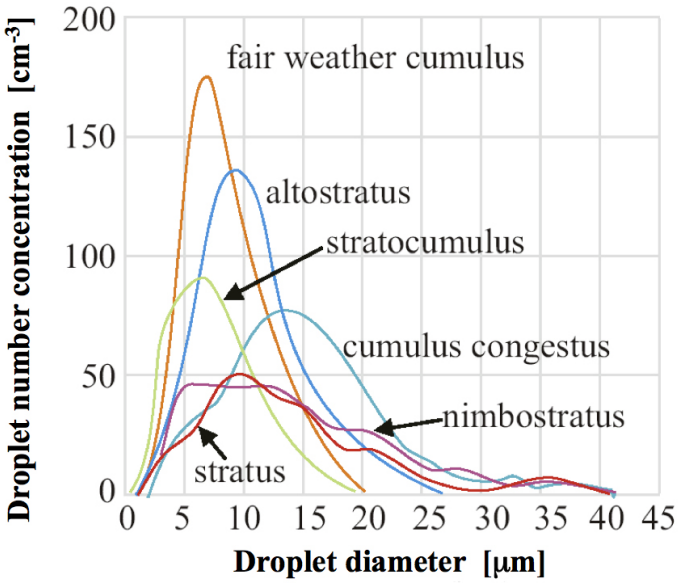

Figure 1.2: *Typical droplet size spectra for different types of water clouds [Quante, 2004]*

The microphysical properties that describe a water cloud are mainly the drop size distribution and the liquid water content (LWC) [Turner et al., 2007], [Mayer et al., 2004]. The drop size distribution is defined as the number density of water drops as a function of drop radius. Then, the LWC is expressed an the integration over the mass of the drop size distribution in g/m^3 or g/kg. Suppose the drop size distribution of clouds changes in a global scale, then the optical properties may affect the global energy budget which consequently might result in a global climate change [Korolev et al., 1999]. In Figure 1.2, a classification for the different types of water clouds is shown based on the droplet number concentration in a cloud as a function of the drop diameter [Quante, 2004]. Nevertheless, for the same type of cloud (e.g. cumulus) the droplet number concentration with respect to the relevant drop radius differs for maritime and continental clouds (Figure 1.3) [Wallace and Hobbs, 2006]. Marine cumulus have fewer droplets than continental cumulus, but marine droplets are larger in radius. Indeed, this is generally true for other type of clouds too. Since clouds over oceans contain less particles but of larger radius compared to the same type of clouds over continents, the total LWC is approximately the same for both environments [Linacre and Geerts, 1999]. The LWC is related to the cloud optical depth, which is the most fundamental property for understanding the cloud interaction with shortwave (i.e., radiation from the sun) and longwave (i.e., sun radiation re-emitted by the Earth) radiation. The cloud optical depth depends on the LWC, the density of liquid water and the droplet effective radius. The effective radius is the area-weighted mean radius of the cloud droplets which is also called extinction-weighted mean radius in the case of water clouds [Mayer et al., 2004]. The most representative effective radius for continental and maritime water cloud droplets is 6μm and 12μm respectively [Turner et al., 2007].

Apart from the microphysical structure, the radiative properties of a water cloud are related to its dynamic properties, like the velocity structure. Explicitly, the most frequent dynamic properties under investigation are the horizontal and vertical wind components and the terminal fall velocity of cloud's hydrometeors. By introducing an earth-relative coordinate system (Fig. 1.4), the radial, measured by a radar, velocity V_r of a cloud, located at a distance r from the radar, is expressed as the contribution of the horizontal wind component $V_{||}(r)$ and the summation of vertical air velocity $w(r)$ (velocity is positive upward) and the terminal fall speed $V_t(r)$ of the hydrometeors. The mathematical expression for the radial velocity is given by the following formula:

$$V_r(r) = V_{||}(r)\delta\cos(el) + (V_t(r) + w(r))\sin(el), \tag{1.1}$$

where $\delta = +1$, when the antenna points in the heading direction and $\delta = -1$, when it points in the opposite direction. Variable el indicates the radar beam direction in elevation [Protat et al., 2002]. Hence, for a

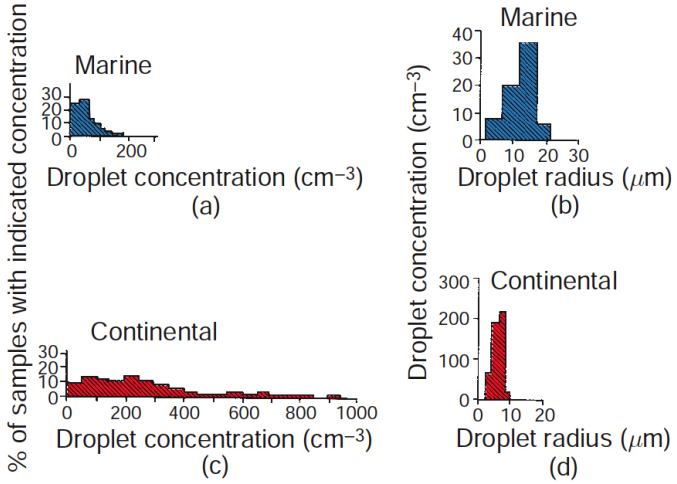

Figure 1.3: *Typical observed cloud droplet number concentration for cumuli in maritime and continental environments [Wallace and Hobbs, 2006]. (a),(c): Percentage of marine respective to continental cumuli with indicated droplet concentrations. (b),(d): Droplet size distribution in marine respectively continental cumuli. Note the different scale for the vertical axes of (b),(d). Marine cumulus contain fewer droplets than continental cumulus, but since marine droplets are larger in radius, the total liquid water content is approximately the same for both environments.*

pointing-vertically Doppler cloud radar, $el = 90^o$ and, thus, the horizontal wind component $V_{\|}(r)$ is not included in the radial velocity measurement.

A better understanding of the dynamics of particles behavior will provide a more thorough insight into evolutionary processes of clouds, which mainly occur over continents [Moran et al., 2012]. The velocity structure varies for the different types of water clouds. For tiny droplets (i.e., in the range of 1-20μm in diameter) present in water clouds, the terminal fall velocity in Eq. (1.1) can be neglected, since it never exceeds the value of $1cms^{-1}$ which is relatively small [Beard, 1976]. By neglecting the terminal fall velocity contribution in Eq. (1.1), the radial velocity, measured from a pointing-vertically Doppler cloud radar, only contains information about the vertical air velocity $w(r)$. In [Ghate et al., 2010], an indication of wind speed variations for non-precipitating boundary layer (BL) continental stratocumulus clouds[3] is provided. The observed mean wind speed lies in the range of $2-10ms^{-1}$ with an average of $5.5ms^{-1}$. Indeed, in [Tokuno, 1996] the low-level cloud motion winds, observed by satellites, never get stronger than $10ms^{-1}$.

1.1.2 The observed radar discrepancy in the case of water clouds

It has been observed that low-level liquid water clouds are often invisible by cloud radars [Clothiaux et al., 1995]. The reason for not being detected by radars, such as millimeter-wave cloud radars operating at $35GHz$ and $94GHz$, is that the measured radar reflectivity factor has lower value compared to the expected one. The so-called radar discrepancy term refers to this deviation between the value of radar reflectivity factor estimated by radar measurements and the theoretical one predicted by the standard radar scattering theory. In [Russchenberg et al., 2009], for a water cloud with expected mean value of $-26dBZ$ radar reflectivity factor, the actual, measured by both $35GHz$ and $94GHz$ radars, mean value of radar reflectivity factor is $\sim -39dBZ$, which makes the radar discrepancy equal to $-13dBZ$. In Figure 1.5, the black curve shows the distribution of radar reflectivity factor for a water cloud as it is estimated by the theory, whereas the green and blue curves represent the distribution of radar reflectivity factor as it was calculated by $35GHz$ and $94GHz$ radar measurements respectively.

[3]Non-precipitating BL stratocumulus clouds studied in [Ghate et al., 2010] have a cloud top lower than $4km$, an in-cloud temperature greater than -5^oC and consist of exclusively liquid water droplets.

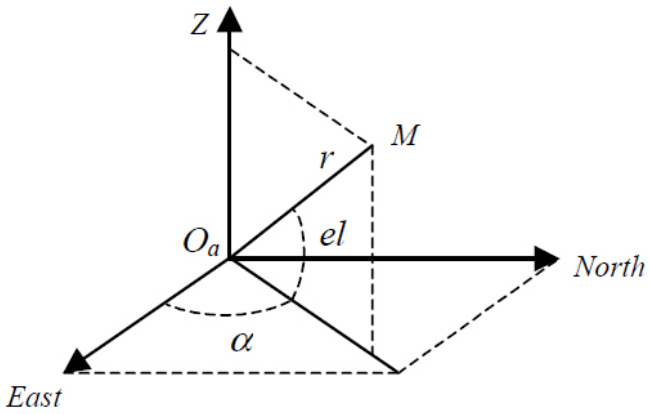

Figure 1.4: *In an earth-relative coordinate system where the radar is located at the point of origin O_α, the radar beam direction is defined by azimuth α and el angle. Range r is the distance between the radar and the cloud target [Protat et al., 2002].*

1.1.3 Possible reasoning of radar discrepancy

Since the concept of the radar discrepancy in water clouds has arisen, the revision of fundamental concepts of radar scattering theories, which are used for the understanding of atmospheric processes, is recently discussed. The reason for this issue is that, in most cases, the incoherent Rayleigh scattering assumption is not valid for water clouds. In water clouds, the concentration of particles is of the order of several hundred droplets per cm^3, which denotes that if the cloud radar operational wavelength is of the mm order, inter-particle distance between droplets may be less than a wavelength. The last statement implies that the phase difference uniform distribution assumption is violated and, indeed, randomness condition required for incoherent scattering theory is not satisfied. The field of statistics and stochastic processes is a useful tool to understand the notion of randomness in a cloud.

The classical radar theory only considers incoherent backscattered radiation by liquid water droplets. However, recently, cloud researchers are interested in the concept of "coherence". According to the definition of Battan [Battan, 1973], a target consisting of many scattering centers, which can move relatively fast with respect to each other, is regarded as incoherent and this is why droplets of a liquid water cloud are expected to produce incoherent radar returns. Nevertheless, since atmospheric turbulence in the cloud may initiate particles' clustering, the positions of cloud particles cannot be considered as perfectly random. The randomness of the particle position ensures the validity of the assumption for uniform distribution of the phase difference of electric fields scattered by the individual droplets. The non-prefect randomness implies spatially correlated particles and, hence a coherent backscatter contribution to the total backscattered power [Jameson and Kostinski, 2010]. The validity of the incoherent scattering assumption may be violated in turbulent conditions. Together with the uniform distribution assumption, the second requirement for incoherent summation of the individual particle backscattered power indicates that droplets inside the illuminated cloud volume move fast enough to change the inter-particle distance by more than a wavelength. The latter requirement is also violated since external forces, such as turbulence, randomize the cloud droplet velocities. The major effect of turbulence is the clustering effect, which means that in the presence of turbulence cloud droplets form small parcels. These parcels behave coherently because the position of their particles do not change randomly enough to result in uniformly distributed phase difference [Russchenberg et al., 2009].

1.2 What is studied in this thesis?

Under the assumption that clouds are not perfectly random, the propagation and scattering of electromagnetic radiation through clouds should be linked to the spatial and temporal distribution of droplets.

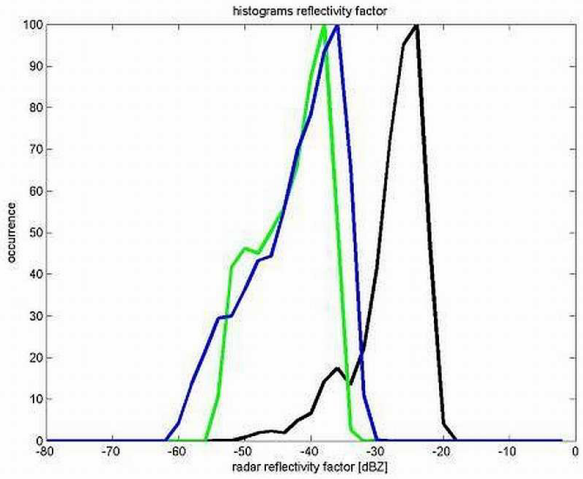

Figure 1.5: *The observed radar discrepancy for the case of non-precipitating stratocumulus clouds [Russchenberg et al., 2009]. Deviation between the measured radar reflectivity factor and the theoretical value. Black curve: the expected radar reflectivity factor by standard scattering theory. Green, Blue curves: the distribution of radar reflectivity factor measured by* $35GHz$ *and* $94GHz$ *radars respectively.*

The incoherent and coherent scattering of electromagnetic radiation are discussed in Chapter 2. Then, the notion of randomness is introduced in Chapter 3. Suppose that the number of droplets inside the cloud volume is a random variable, but still countable. Then, the perfect randomness for a collection of particles can be considered as a statistically homogeneous Poisson process where the position of particles is uniformly distributed in the cloud volume and completely uncorrelated (i.e. statistically independent). On the other hand, in case of non-statistically independent particle positions due to the clustering effect of turbulence, the random process is still statistically homogeneous but not spatial uncorrelated any more. Statistical homogeneity of this random process denotes that the mean particle density is spatially independent and non-deterministic. As a result, in case of turbulent clustering, the randomness is not perfect since the positions of particles are correlated. Thus, it is obvious that spatial correlation implies a deviation from perfect randomness [Shaw, 2003]. In this case study, the spatial correlation of droplets in turbulent clouds and the clustering effect of turbulence are explored through the random walks approach, which is described in Chapter 4. The latter is a tool in stochastic processes which is used for extracting the statistical properties of electromagnetic waves scattered by objects containing few scattering centers.

In particular, the total backscattered electric field measured by the radar is considered as the coherent summation of the individual electric fields. Then, the backscattered field is studied for spatial correlated cloud particles that undergo different types of motion and a comparative analysis between the backscattered fields is provided. The results are fruitful for understanding the sensitivity of the radar backscattered field under various scales of turbulence (i.e. small or/and large eddies). The degree of position particles' correlation is pertinent to the number of clusters present in the illuminated cloud volume. The radar backscattered electric field and the corresponding backscattered power are investigated for several number of clusters. The radar backscattered power distributions are explored with respect to random walks theory. The computational model and the results from the simulations are explicitly discussed in Chapters 5, 6 and 7. Finally, the conclusions of this study are given in Chapter 8, where recommendations for further research are also presented.

2 Scattering theory

The scattering characteristics of an electromagnetic wave in the presence of cloud droplets are investigated in this chapter. The following approach starts with deriving the Electric Field Volume Integral Equation (EFVIE) from the Maxwell's equations. Then, the scattered field by a single droplet is estimated through discretization of the EFVIE and, hence, the scattered field by a collection of N cloud droplets is approximated by the summation of the N individual scattered fields. Furthermore, the intensity of the field scattered by randomly distributed cloud droplets is separated into a coherent and incoherent part. These field intensities relate to the corresponding coherent and incoherent scattered power.

2.1 Electromagnetic wave in interaction with the scatterer

The analysis will be given in the frequency-domain assuming $exp(-i\omega t)$ time dependence. The source generates electromagnetic wave which travels inside a volume where a scatterer is present. Define D as the domain of the total illuminated volume (i.e., background medium+scattering object) and D_{sc} as the domain of scatterer's volume, such as $D_{sc} \subset D$. The contrast-source Maxwell's equations in differential form are:

$$-\nabla \times \mathbf{H}(\mathbf{x},\omega) + \eta(\mathbf{x},\omega)\mathbf{E}(\mathbf{x},\omega) = -\mathbf{J}(\mathbf{x},\omega), \tag{2.1}$$

$$\nabla \times \mathbf{E}(\mathbf{x},\omega) + \zeta(\mathbf{x},\omega)\mathbf{H}(\mathbf{x},\omega) = -\mathbf{K}(\mathbf{x},\omega), \tag{2.2}$$

where $\mathbf{J}(\mathbf{x},\omega)$ and $\mathbf{K}(\mathbf{x},\omega)$ indicate the external and magnetic current respectively. Variables $\mathbf{E}$ and $\mathbf{H}$ are the unknown total electric and magnetic fields respectively. For any $\mathbf{x} \in D \setminus D_{sc}$, the total fields are given as the summation of incident and scattered fields. Incident fields are present at any observation point $\mathbf{x} \in D$, while scattered fields only exist outside the scattering volume, at points $\mathbf{x} \in D \setminus D_{sc}$.

For an isotropic[1] medium, the transverse admittance η and impedance ζ are expressed as:

$$\eta(\mathbf{x},\omega) = \sigma(\mathbf{x},\omega) - i\omega\epsilon(\mathbf{x},\omega), \tag{2.3}$$

[1] A medium is called isotropic if its physical properties stay unchanged in any direction.

$$\zeta(\mathbf{x},\omega) = -i\omega\mu(\mathbf{x},\omega), \tag{2.4}$$

where ϵ is the dielectric permittivity, μ is the magnetic permeability and σ is the conductivity of the medium.

Suppose that the volume illuminated by the source contains only the homogeneous[2] background medium, without the presence of any scatterer, so as $D_{sc} = \emptyset$. Now, the only existing fields are the incident fields. Then, Maxwell's equations for the same sources would become:

$$-\nabla \times \mathbf{H}^{\text{in}}(\mathbf{x},\omega) + \eta_b(\omega)\mathbf{E}^{\text{in}}(\mathbf{x},\omega) = -\mathbf{J}(\mathbf{x},\omega), \tag{2.5}$$

$$\nabla \times \mathbf{E}^{\text{in}}(\mathbf{x},\omega) + \zeta_b(\omega)\mathbf{H}^{\text{in}}(\mathbf{x},\omega) = -\mathbf{K}(\mathbf{x},\omega), \tag{2.6}$$

where the transverse admittance and impedance $\eta_b(\omega)$ and $\zeta_b(\omega)$ of the homogeneous background medium are constants.

Since the scattered fields can be found by subtracting the incident fields from total fields, the mathematical expressions of scattered electric and magnetic field are introduced by subtracting Eq. (2.5), (2.6) from Eq. (2.1), (2.2):

$$-\nabla \times \mathbf{H}^{\text{sc}}(\mathbf{x},\omega) + \eta_b(\omega)\mathbf{E}^{\text{sc}}(\mathbf{x},\omega) = -[\eta(\mathbf{x},\omega) - \eta_b(\omega)]\mathbf{E}(\mathbf{x},\omega), \tag{2.7}$$

$$\nabla \times \mathbf{E}^{\text{sc}}(\mathbf{x},\omega) + \zeta_b(\omega)\mathbf{H}^{\text{sc}}(\mathbf{x},\omega) = -[\zeta(\mathbf{x},\omega) - \zeta_b(\omega)]\mathbf{H}(\mathbf{x},\omega), \tag{2.8}$$

where the difference between the constitutive parameters of the scatterer and the background medium is called 'the contrast'.

Let's introduce:

1. the wavenumber of the background medium

$$k_b^2(\omega) = -\eta_b(\omega)\zeta_b(\omega) = \omega^2\epsilon_b(\omega)\mu_b(\omega) + i\omega\sigma_b(\omega)\mu_b(\omega), \tag{2.9}$$

2. the scalar green function, for $\mathbf{x} \in D$ and $\mathbf{x}' \in D_{sc}$

$$g(\mathbf{x}-\mathbf{x}',\omega) = \frac{e^{ik_b(\omega)|\mathbf{x}-\mathbf{x}'|}}{4\pi|\mathbf{x}-\mathbf{x}'|}, \tag{2.10}$$

3. and the normalized electric contrast

$$\chi_e(\mathbf{x},\omega) = \frac{\eta(\mathbf{x},\omega)}{\eta_b(\omega)} - 1. \tag{2.11}$$

Under the assumption that the magnetic contrast is zero, by combining equations Eq. (2.5), (2.6), (2.7) and (2.8), the so-called Electric Field Volume Integral Equation (EFVIE) can be estimated as:

$$\begin{aligned}\mathbf{E}^{\text{in}}(\mathbf{x},\omega) = \mathbf{E}(\mathbf{x},\omega) - \\ [k_b^2(\omega) + \nabla\nabla\cdot] \int\limits_{\mathbf{x}'\in D_{sc}} g(\mathbf{x}-\mathbf{x}',\omega)\chi_e(\mathbf{x}',\omega)\mathbf{E}(\mathbf{x}',\omega)dV.\end{aligned} \tag{2.12}$$

The entire derivation of EFVIE is explicitly given in [Budko, 2005-2008]. Once the total field is known, the incident field is estimated by Eq. (2.12) and, thus, the scattered electric field can be given by:

$$\begin{aligned}\mathbf{E}^{\text{sc}}(\mathbf{x},\omega) &= \mathbf{E}(\mathbf{x},\omega) - \mathbf{E}^{\text{in}}(\mathbf{x},\omega) \\ &= [k_b^2(\omega) + \nabla\nabla\cdot] \int\limits_{\mathbf{x}'\in D_{sc}} g(\mathbf{x}-\mathbf{x}',\omega)\chi_e(\mathbf{x}',\omega)\mathbf{E}(\mathbf{x}',\omega)dV.\end{aligned} \tag{2.13}$$

[2] A medium is called homogeneous if its physical properties stay unchanged at any location.

2.2 Scattering by cloud droplets

The principles of scattering theory are discussed for a basic meteorological radar set-up, as the one illustrated in Figure 2.1. The radar uses the same transmit and receive antenna located at a distance $\mathbf{x}_R = \mathbf{x}_S$ from the origin of the Cartesian coordinate system. $\mathbf{P}_S$ is the unit vector in the direction of the current flow times the length of the source. By convention, in the following analysis, polarization vector $\mathbf{P}_S$ is directed along the x_1-axis of the reference system and with unit magnitude $|\mathbf{P}_S| = 1$. Suppose that the total number of particles inside the illuminated cloud volume is N. Then,the n^{th} particle, $n = 1, 2, ..., N$, located at distance $\mathbf{x}_n$ with respect to the origin, is $|\mathbf{x}_R - \mathbf{x}_n| = |\mathbf{x}_n - \mathbf{x}_S|$ far from the radar. Θ_n^R denotes the unit vector along the *(n^{th} particle-receiver)*-direction. Then, the tensor[3] $\mathbb{Q}_n^R$ can be expressed as:

$$\mathbb{Q}_n^R = \Theta_n^R(\Theta_n^R \cdot) = \frac{(\mathbf{x}_R - \mathbf{x}_n)(\mathbf{x}_R - \mathbf{x}_n)^\top}{|\mathbf{x}_R - \mathbf{x}_n|^2} \tag{2.14}$$

Similarly, Θ_S^n denotes the unit vector along the *(source-n^{th} particle)*-direction and, thus, the tensor $\mathbb{Q}_S^n$ can be expressed as:

$$\mathbb{Q}_S^n = \Theta_S^n(\Theta_S^n \cdot) = \frac{(\mathbf{x}_n - \mathbf{x}_S)(\mathbf{x}_n - \mathbf{x}_S)^\top}{|\mathbf{x}_n - \mathbf{x}_S|^2} \tag{2.15}$$

The scattering by the n^{th} particle is considered only at the backward direction, at an angle β_n, since radar uses the same source and receiver. Apparently, $\mathbb{Q}_n^R = \mathbb{Q}_R^n = \mathbb{Q}_S^n$.

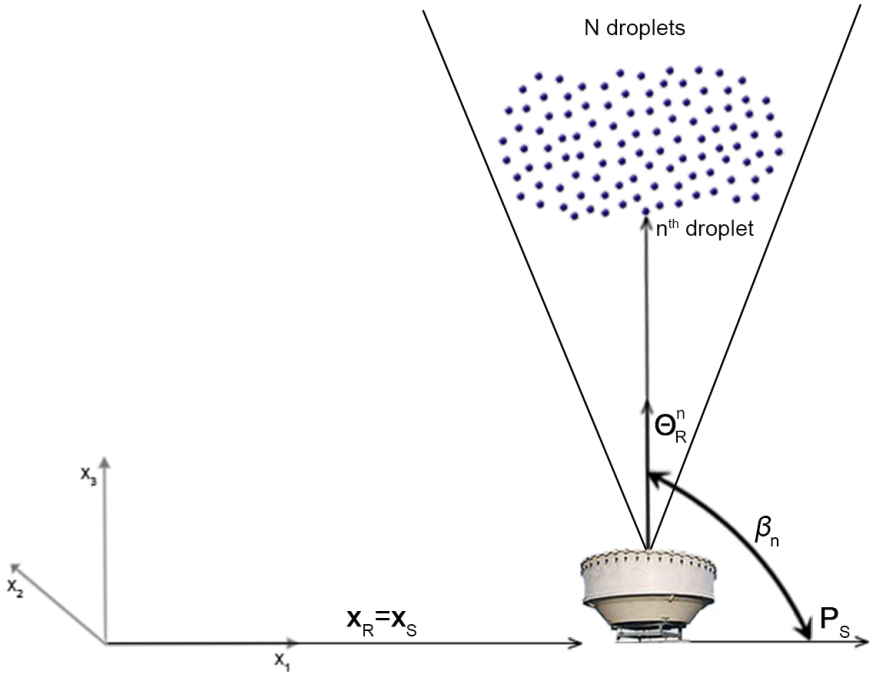

Figure 2.1: *Cloud-radar representation. The ground radar is looking into a cloud volume filled with N droplets. The radar is located at a distance $\mathbf{x}_R = \mathbf{x}_S$ from the reference coordinate system. Θ_R^n is the unit vector along the (receiver-n^{th} particle)-direction. $\mathbf{P}_S$ is the polarization unit vector of the point-source. Here, its orientation is along the x_1-axis of the reference system. β_n denotes the n^{th} backscattering angle.*

The fundamentals of a radar backscattered field can be well-understood through the scattering of a plane electromagnetic wave by a single cloud droplet, which is considered as a perfect sphere. Let

[3] A tensor is a geometric object which describes linear relations between vectors, scalars and other tensors.

$\mathbf{E}^{\text{in}}(\mathbf{x}_S, \mathbf{x}_n)$ be the incident field acting on the n$^{\text{th}}$ droplet and $\mathbf{E}^{\text{sc}}(\mathbf{x}_R, \mathbf{x}_n)$ be the scattered field by the individual droplet. Then, since the total scattered field at the receiver is expressed as the summation of the individual contributions from all N scatterers, the scattered field under the Rayleigh approximation due to the n$^{\text{th}}$ particle in the far field should be initially derived. The Rayleigh approximation holds for particles small compared to the operational wavelength. As mentioned in Chapter 1, Mie scattering expresses the scattering of electromagnetic radiation by a sphere as a solution to Maxwell's equations. By defining the size parameter of a scattering spherical particle as the ratio $x = \frac{2\pi r}{\lambda}$, where r is the effective radius of the sphere, Mie scattering reduces to Rayleigh approximation for very small $x << 1$.

2.2.1 Scattered field by a single droplet

The integral in Eq. (2.12) and (2.13) has been taken over a continuous scatterer (i.e., $\mathbf{x}'$ gets continuous values inside the domain of the scattering object D_{sc}). However, a cloud can only be considered as a discontinuous scattering object since the droplets are discrete and, hence, the variable $\mathbf{x}'$ can take N discrete values. This is why the integral should be approximated by a numerical integration (i.e., such as a sum). The numerical expression of Eq. (2.12) is derived in [Budko, 2005-2008] through a discretization method. Thus, if α denotes the effective radius of the spherical droplet, the numerical expression for the incident field acting at the n$^{\text{th}}$ particle is given as:

$$\begin{aligned}\mathbf{E}^{\text{in}}(\mathbf{x}_s, \mathbf{x}_n, \omega) &= \mathbf{E}(\mathbf{x}_R, \mathbf{x}_n, \omega) - \left[\frac{2}{3}(1 - ik_b(\omega)\alpha)e^{ik_b(\omega)\alpha} - 1\right]\chi(\mathbf{x}_n, \omega)\mathbf{E}(\mathbf{x}_R, \mathbf{x}_n, \omega) \\ &= \mathbf{E}(\mathbf{x}_R, \mathbf{x}_n, \omega)\left[1 - \left(\frac{2}{3}(1 - ik_b(\omega)\alpha)e^{ik_b(\omega)\alpha} - 1\right)(\epsilon_n(\omega) - 1)\right],\end{aligned} \tag{2.16}$$

where $\mathbf{E}(\mathbf{x}_R, \mathbf{x}_n, \omega)$ denotes the total electric field measured at the position of the receiver ($\mathbf{x}_R$) and the normalized electric contrast $\chi(\mathbf{x}_n, \omega) = \frac{\eta(\mathbf{x}_n, \omega)}{\eta_b(\omega)} - 1 = \epsilon_n(\omega) - 1$ with ϵ_n denoting the relative dielectric permitivity of the n$^{\text{th}}$ particle.
By omitting the frequency dependence, Eq. (2.16) becomes:

$$\mathbf{E}^{\text{in}}(\mathbf{x}_s, \mathbf{x}_n) = \mathbf{E}(\mathbf{x}_R, \mathbf{x}_n)\left[1 - \left(\frac{2}{3}(1 - ik_b\alpha)e^{ik_b\alpha} - 1\right)(\epsilon_n - 1)\right] \tag{2.17}$$

and since the expression in brackets is a scalar, the total field acting on the n$^{\text{th}}$ particle equals:

$$\mathbf{E}(\mathbf{x}_R, \mathbf{x}_n) = \frac{\mathbf{E}^{\text{in}}(\mathbf{x}_s, \mathbf{x}_n)}{1 - \left(\frac{2}{3}(1 - ik_b\alpha)e^{ik_b\alpha} - 1\right)(\epsilon_n - 1)} \tag{2.18}$$

Furthermore, the numerical expression of the scattered electric field measured at the position of the receiver ($\mathbf{x}_R$) due to the n$^{\text{th}}$ cloud droplet, n=1,2,...,N is approximated by the formula:

$$\mathbf{E}^{\text{sc}}(\mathbf{x}_R, \mathbf{x}_n) \approx \mathbb{G}(\mathbf{x}_R - \mathbf{x}_n)(\epsilon_n - 1)\mathbf{E}(\mathbf{x}_R, \mathbf{x}_n)V_n, \tag{2.19}$$

where V_n denotes the volume of the n$^{\text{th}}$ droplet.
By substituting equation (2.18) in equation (2.19):

$$\mathbf{E}^{\text{sc}}(\mathbf{x}_R, \mathbf{x}_n) = \mathbb{G}(\mathbf{x}_R - \mathbf{x}_n)(\epsilon_n - 1)\frac{\mathbf{E}^{\text{in}}(\mathbf{x}_s, \mathbf{x}_n)}{1 - \left(\frac{2}{3}(1 - ik_b\alpha)e^{ik_b\alpha} - 1\right)(\epsilon_n - 1)}V_n, \tag{2.20}$$

where the expression for the Green tensor is given by:

$$\begin{aligned}\mathbb{G}(\mathbf{x}_R - \mathbf{x}_n) = g(\mathbf{x}_R - \mathbf{x}_n)\Bigg[&\left(-k_b^2 - \frac{i3k_b}{|\mathbf{x}_R - \mathbf{x}_n|} + \frac{3}{|\mathbf{x}_R - \mathbf{x}_n|^2}\right)\mathbb{Q}(\mathbf{x}_R - \mathbf{x}_n) + \\ &+\left(k_b^2 + \frac{ik_b}{|\mathbf{x}_R - \mathbf{x}_n|} - \frac{1}{|\mathbf{x}_R - \mathbf{x}_n|^2}\right)\mathbb{I}\Bigg],\end{aligned} \tag{2.21}$$

where $\mathbb{I}$ is the Cartesian unit tensor δ_{nm} and the green function is reformulated as:

$$g(\mathbf{x}_\mathrm{R}-\mathbf{x}_\mathrm{n}) = \frac{e^{ik_b|\mathbf{x}_\mathrm{R}-\mathbf{x}_\mathrm{n}|}}{4\pi\,|\mathbf{x}_\mathrm{R}-\mathbf{x}_\mathrm{n}|}. \tag{2.22}$$

2.2.2 Far-field approximation

Suppose d denotes the droplet diameter and λ the radar operational wavelength, within a short distance between the n^{th} particle and the radar $|\mathbf{x}_\mathrm{R}-\mathbf{x}_\mathrm{n}| < \frac{d^2}{\lambda}$. Then, the scattered field has complicated amplitude and phase variations because of the interference between contributions from different parts of the droplet. The observation point $\mathbf{x}_\mathrm{R}$ is thought to be in the near field of the particle. However, when distance $|\mathbf{x}_\mathrm{R}-\mathbf{x}_\mathrm{n}| > \frac{d^2}{\lambda}$, the observation point $\mathbf{x}_\mathrm{R}$ is thought to be in the far field of the particle [Ishimaru, 1997]. In general, this means that $|\mathbf{x}_\mathrm{n}| >> |\mathbf{x}_\mathrm{R}|$ and, subsequently, $|\mathbf{x}_\mathrm{R}-\mathbf{x}_\mathrm{n}| >> 1$. The scattered field behaves as a spherical wave in the far field of the particle since the Green's tensor is approximated as:

$$\mathbb{G}(\mathbf{x}_\mathrm{R}-\mathbf{x}_\mathrm{n}) \approx g(\mathbf{x}_\mathrm{R}-\mathbf{x}_\mathrm{n})(-k_b^2)[\mathbb{Q}(\mathbf{x}_\mathrm{R}-\mathbf{x}_\mathrm{n})-\mathbb{I}]. \tag{2.23}$$

Therefore, by substituting equations (2.23) and (2.22) in equation (2.20):

$$\mathbf{E}^{\mathrm{sc}}(\mathbf{x}_\mathrm{R},\mathbf{x}_\mathrm{n}) = \frac{e^{ik_b|\mathbf{x}_\mathrm{R}-\mathbf{x}_\mathrm{n}|}}{4\pi\,|\mathbf{x}_\mathrm{R}-\mathbf{x}_\mathrm{n}|}\underbrace{\frac{-k_b^2V_\mathrm{n}(\epsilon_n-1)}{1-\left(\frac{2}{3}(1-ik_b\alpha)e^{ik_b\alpha}-1\right)(\epsilon_n-1)}}_{A}[\mathbb{Q}(\mathbf{x}_\mathrm{R}-\mathbf{x}_\mathrm{n})-\mathbb{I}]\mathbf{E}^{\mathrm{in}}(\mathbf{x}_\mathrm{s},\mathbf{x}_\mathrm{n}), \tag{2.24}$$

where the quantity A can be rearranged as:

$$\begin{aligned} A &= 1-\left[\frac{2}{3}(1-ik_b\alpha_\mathrm{n})e^{ik_b\alpha_\mathrm{n}}-1\right](\epsilon_n-1) = 1+\left[\frac{2}{3}(1-ik_b\alpha_\mathrm{n})e^{ik_b\alpha_\mathrm{n}}-1\right](1-\epsilon_n) \\ &= 1+\frac{2}{3}(1-ik_b\alpha_\mathrm{n})e^{ik_b\alpha_\mathrm{n}}(1-\epsilon_n)-1+\epsilon_n = \underbrace{-\frac{2}{3}ik_b\alpha_\mathrm{n}e^{ik_b\alpha_\mathrm{n}}(1-\epsilon_n)}_{A1(\alpha_\mathrm{n})}+\underbrace{\frac{2}{3}e^{ik_b\alpha_\mathrm{n}}(1-\epsilon_n)+\epsilon_n}_{A2(\alpha_\mathrm{n})}. \end{aligned} \tag{2.25}$$

2.2.3 Rayleigh approximation

The scattering characteristics of a small particle are called Rayleigh scattering. Let's consider that the droplet is a dielectric sphere, whose size is much smaller than a wavelength. Since the drop size is very small $\alpha_\mathrm{n} << 1(\sim \mu m)$, the contribution A1 of Eq. (2.25) converges to:

$$\lim_{\alpha_\mathrm{n}\to 0} A1(\alpha_\mathrm{n}) = \lim_{\alpha_\mathrm{n}\to 0}\left(\frac{2}{3}ik_b\alpha_\mathrm{n}e^{ik_b\alpha_\mathrm{n}}(1-\epsilon_n)\right) = \lim_{\alpha_\mathrm{n}\to 0}\left(ik_b\alpha_\mathrm{n}\Big(\cos(k_b\alpha_\mathrm{n})+i\sin(k_b\alpha_\mathrm{n})\Big)(1-\epsilon_n)\right) = 0. \tag{2.26}$$

Given that $\lim_{\alpha_\mathrm{n}\to 0}\left(e^{ik_b\alpha_\mathrm{n}}\right) = 1$, the contribution A2 of Eq. (2.25) is limited to the following expression:

$$A2(\alpha_\mathrm{n}) = \frac{2}{3}e^{ik_b\alpha_\mathrm{n}}(1-\epsilon_n)+\epsilon_n \simeq \frac{2}{3}-\frac{2}{3}\epsilon_n+\epsilon_n = \frac{1}{3}(\epsilon_n+2). \tag{2.27}$$

Finally, since $A = \frac{1}{3}(\epsilon_n+2)$, equation (2.24) of the scattered electric field is expressed as:

$$\mathbf{E}^{\mathrm{sc}}(\mathbf{x}_\mathrm{R},\mathbf{x}_\mathrm{n}) = \frac{3k_b^2V_\mathrm{n}(\epsilon_n-1)}{4\pi(\epsilon_n+2)}\frac{e^{ik_b|\mathbf{x}_\mathrm{R}-\mathbf{x}_\mathrm{n}|}}{|\mathbf{x}_\mathrm{R}-\mathbf{x}_\mathrm{n}|}[\mathbb{I}-\mathbb{Q}_\mathrm{n}^\mathrm{R}]\mathbf{E}^{\mathrm{in}}(\mathbf{x}_\mathrm{S},\mathbf{x}_\mathrm{n}), \tag{2.28}$$

and the incident field acting on the nth particle equals:

$$\mathbf{E}^{\text{in}}(\mathbf{x}_\text{S}, \mathbf{x}_\text{n}) = \frac{e^{ik_b|\mathbf{x}_\text{S}-\mathbf{x}_\text{n}|}}{4\pi|\mathbf{x}_\text{S}-\mathbf{x}_\text{n}|}[\mathbb{I}-\mathbb{Q}_\text{S}^\text{n}]\mathbf{P}_\text{S}, \tag{2.29}$$

with magnitude of polarization vector $\|\mathbf{P}_\text{S}\| = 1$.
By substituting equation (2.29) in (2.28):

$$\begin{aligned}\mathbf{E}^{\text{sc}}(\mathbf{x}_\text{R}, \mathbf{x}_\text{n}) &= \frac{3k_b^2 V_\text{n}(\epsilon_n - 1)}{(\epsilon_n + 2)} \frac{e^{i2k_b|\mathbf{x}_\text{R}-\mathbf{x}_\text{n}|}}{(4\pi)^2|\mathbf{x}_\text{R}-\mathbf{x}_\text{n}|^2}[\mathbb{I}-\mathbb{Q}_\text{n}^\text{R}][\mathbb{I}-\mathbb{Q}_\text{S}^\text{n}]\mathbf{P}_\text{S} \\ &= \frac{3k_b^2 V_\text{n}}{(4\pi)^2} \frac{(\epsilon_n - 1)}{(\epsilon_n + 2)} \frac{e^{i2k_b|\mathbf{x}_\text{R}-\mathbf{x}_\text{n}|}}{|\mathbf{x}_\text{R}-\mathbf{x}_\text{n}|^2}[\mathbb{I}-\mathbb{Q}_\text{n}^\text{R}]\mathbf{P}_\text{S},\end{aligned} \tag{2.30}$$

since the tensor $[\mathbb{I}-\mathbb{Q}_\text{n}^\text{R}]$ is a projector[4] with the property $[\mathbb{I}-\mathbb{Q}_\text{n}^\text{R}]^2 = [\mathbb{I}-\mathbb{Q}_\text{n}^\text{R}]$.

2.2.4 Scattered field by the total number of droplets

In section 2.2.3, the scattered field under the Rayleigh approximation due to the nth small particle in the far field was approximated by Eq. (2.30). Then, the kth component (k=1,2,3) of the total scattered field at the receiver will be given as the summation of the scattered field contributions of all N cloud droplets:

$$\mathbf{E}_k^{\text{sc}}(\mathbf{x}_\text{R}) = \sum_{\text{n}=1}^{N} \mathbf{E}_k^{\text{sc}}(\mathbf{x}_\text{R}, \mathbf{x}_\text{n}) = \sum_{\text{n}=1}^{N} \underbrace{\frac{3k_b^2 V_\text{n}}{(4\pi)^2|\mathbf{x}_\text{R}-\mathbf{x}_\text{n}|^2}\left|\frac{\epsilon_n - 1}{\epsilon_n + 2}\right| \boldsymbol{D}_{kn}}_{amplitude} e^{\overbrace{i(2k_b|\mathbf{x}_\text{R}-\mathbf{x}_\text{n}| + \phi_\text{n})}^{phase}}, \tag{2.31}$$

given that the ratio $\frac{\epsilon_n-1}{\epsilon_n+2} = \left|\frac{\epsilon_n-1}{\epsilon_n+2}\right| e^{i\phi_n}$ is a complex number and vector $\boldsymbol{D}_{kn}$ is expressed as:

$$\boldsymbol{D}_{kn} = \Big([\mathbb{I}-\mathbb{Q}_\text{n}^\text{R}]\mathbf{P}_\text{S}\Big)_\text{k} = \delta_\text{km}\mathbf{P}_\text{m}^\text{S} - \Theta_\text{k}^\text{n}\Theta_\text{m}^\text{n}\mathbf{P}_\text{m}^\text{S} = \mathbf{P}_\text{k}^\text{S} - \Theta_\text{k}^\text{n}\Big[|\Theta_\text{m}^\text{n}||\mathbf{P}_\text{m}^\text{s}| \cdot \cos(\beta_\text{n})\Big] = \mathbf{P}_\text{k}^\text{S} - \Theta_\text{k}^\text{n}\cos(\beta_\text{n}), \tag{2.32}$$

where β_n the nth backscattering angle.

2.3 Coherent and Incoherent Fields

In case of random discrete scatterers, the particles are randomly distributed in positions, shapes, sizes and orientations so that the scattered fields are fluctuating randomly. Indeed, Eq. (2.31) shows that the scattered field is a random function of position. For this reason, the scattered fields are called random fields, which are induced by random media.

Cloud is considered as a random medium and thus, the scattered, by its droplets, fields and intensities are expected to fluctuate from one realization to the other just due to the motion of the droplets, often in clusters [Tsang and Ding, 2000]. Although for deterministic scattering problems there is a unique solution for all the realizations, for random media problems, the solution is unique only for a single realization. Assume that, between realizations, the positions of particles change randomly enough to result in uniformly distributed scattered electric field phase difference. Then, the solution can be considered unique for all the realizations. This type of random media, with a unique solution for their scattering problem, are called perfectly random media. After many realizations, the kth component of the total scattered field can be expressed as the summation of an average field $\langle\mathbf{E}\rangle$ and the fluctuating field $\mathcal{E}$:

[4]Projection is a linear transformation P from a vector space to itself such that $P^2 = P$. Actually, it leaves its image unchanged.

$$\sum_{n=1}^{N} \mathbf{E}_k^{\mathrm{sc}}(\mathbf{x}_\mathrm{R}, \mathbf{x}_\mathrm{n}) = \mathbf{E}_k^{\mathrm{sc}}(\mathbf{x}_\mathrm{R}) = \langle \mathbf{E}_k^{\mathrm{sc}}(\mathbf{x}_\mathrm{R}) \rangle + \mathcal{E}_k^{\mathrm{sc}}(\mathbf{x}_\mathrm{R}) \tag{2.33}$$

$$\langle \mathcal{E}_k^{\mathrm{sc}}(\mathbf{x}_\mathrm{R}) \rangle = 0. \tag{2.34}$$

The average field indicates that the position of the particles do not change randomly enough to result in uniformly distributed phase difference. Thus, an ensemble averaging of all scattered fields should be considered. However, the fluctuating field ignores spatial correlation between particles and, hence, the ensemble averaging of the fluctuating field is zero. The average field is called coherent field and the fluctuating field is called incoherent field.

The intensity of the scattered field can be given as the expression:

$$\mathbf{I}_k = \mathbf{E}_k^{\mathrm{sc}}(\mathbf{x}_\mathrm{R}) \mathbf{E}_k^{\mathrm{sc}}(\mathbf{x}_\mathrm{R})^* = \langle \mathbf{E}_k^{\mathrm{sc}}(\mathbf{x}_\mathrm{R}) \rangle \langle \mathbf{E}_k^{\mathrm{sc}}(\mathbf{x}_\mathrm{R})^* \rangle + \langle \mathbf{E}_k^{\mathrm{sc}}(\mathbf{x}_\mathrm{R}) \rangle \mathcal{E}_k^{\mathrm{sc}}(\mathbf{x}_\mathrm{R})^* + \langle \mathbf{E}_k^{\mathrm{sc}}(\mathbf{x}_\mathrm{R})^* \rangle \mathcal{E}_k^{\mathrm{sc}}(\mathbf{x}_\mathrm{R}) + \mathcal{E}_k^{\mathrm{sc}}(\mathbf{x}_\mathrm{R}) \mathcal{E}_k^{\mathrm{sc}}(\mathbf{x}_\mathrm{R})^*. \tag{2.35}$$

Then, by taking the average of Eq. (2.35)

$$\begin{aligned} \langle \mathbf{I}_k \rangle = \langle \mathbf{E}_k^{\mathrm{sc}}(\mathbf{x}_\mathrm{R}) \mathbf{E}_k^{\mathrm{sc}}(\mathbf{x}_\mathrm{R})^* \rangle &= \langle \mathbf{E}_k^{\mathrm{sc}}(\mathbf{x}_\mathrm{R}) \rangle \langle \mathbf{E}_k^{\mathrm{sc}}(\mathbf{x}_\mathrm{R})^* \rangle + \langle \mathcal{E}_k^{\mathrm{sc}}(\mathbf{x}_\mathrm{R}) \mathcal{E}_k^{\mathrm{sc}}(\mathbf{x}_\mathrm{R})^* \rangle \\ &= |\langle \mathbf{E}_k^{\mathrm{sc}}(\mathbf{x}_\mathrm{R}) \rangle|^2 + \langle |\mathcal{E}_k^{\mathrm{sc}}(\mathbf{x}_\mathrm{R})|^2 \rangle = \mathbf{I}_k^{\mathrm{c}} + \mathbf{I}_k^{\mathrm{f}}. \end{aligned} \tag{2.36}$$

Hence, if $\overline{N}$ denotes the mean total number of particles in a sample cloud volume V, the electric field intensity has a coherent $\mathbf{I}_k^{\mathrm{c}} = |\langle \mathbf{E}_k^{\mathrm{sc}}(\mathbf{x}_\mathrm{R}) \rangle|^2 \propto \overline{N}^2$ and an incoherent $\mathbf{I}_k^{\mathrm{f}} = \langle |\mathcal{E}_k^{\mathrm{sc}}(\mathbf{x}_\mathrm{R})|^2 \rangle \propto \overline{N}$ part. In [Jameson and Kostinski, 2009], mathematical expressions for the incoherent and coherent part of intensity are given while explaining how the incoherent and coherent part is proportional to $\overline{N}$ and $\overline{N}^2$ respectively. In particular, the coherent part is derived through the coherent Bragg scatter from distributed particles. Hence, the mathematical formulas for the coherent part of intensity contains the pair-correlation function which means that spatial correlation among particles is considered. Pair-correlation function will be introduced in Chapter 3.

2.4 Coherent and Incoherent Power

The actual quantity measured by the radar is the backscattered power. Scattered power is estimated by the intensity of the scattered field. Since intensity has a coherent and incoherent part, power can be also distinguished as coherent or incoherent power.

The incoherent scattering theory assumes zero mutual interaction between the cloud droplets. The positions of particles change randomly enough to result in uniformly distributed phase difference. Therefore, the incoherent scattering problem has one unique solution for all realizations. Hence for an incoherent scattering problem, scattered field of Eq. (2.33) gets limited to:

$$\mathbf{E}_k^{\mathrm{sc}}(\mathbf{x}_\mathrm{R}) = \mathcal{E}_k^{\mathrm{sc}}(\mathbf{x}_\mathrm{R}) \tag{2.37}$$

From the incoherent part of Eq. (2.36), one understands that the incoherent power will be given as the summation of the intensities of the N individual scattered fields:

$$\mathbf{P}_{inc} \cong \sum_{n=1}^{N} \|\mathbf{E}^{\mathrm{sc}}(\mathbf{x}_\mathrm{R}, \mathbf{x}_\mathrm{n})\|^2 = \sum_{k=1}^{3} \sum_{n=1}^{N} |\mathbf{E}_k^{\mathrm{sc}}(\mathbf{x}_\mathrm{R}, \mathbf{x}_\mathrm{n})|^2. \tag{2.38}$$

However, in coherent scattering theory, the interaction between adjacent droplets is taken into consideration. From the coherent part of Eq. (2.36), one understands that the coherent power will be given as the intensity of the total scattered field calculated as the summation of the N individual scattered fields:

$$\mathbf{P}_c \cong \left\| \sum_{n=1}^{N} \mathbf{E}^{\mathrm{sc}}(\mathbf{x}_\mathrm{R}, \mathbf{x}_\mathrm{n}) \right\|^2 = \sum_{k=1}^{3} \left| \sum_{n=1}^{N} \mathbf{E}_k^{\mathrm{sc}}(\mathbf{x}_\mathrm{R}, \mathbf{x}_\mathrm{n}) \right|^2. \tag{2.39}$$

In the above formulas, square norm of the vector $\mathbf{E}^{\mathrm{sc}}(\mathbf{x}_{\mathrm{R}},\mathbf{x}_{\mathrm{n}})$ denotes the summation of all k^{th} components of field intensities:

$$\|\mathbf{E}^{\mathrm{sc}}(\mathbf{x}_{\mathrm{R}},\mathbf{x}_{\mathrm{n}})\|^2=\sum_{k=1}^{3}|\mathbf{E}_k^{\mathrm{sc}}(\mathbf{x}_{\mathrm{R}},\mathbf{x}_{\mathrm{n}})|^2=|\mathbf{E}_1^{\mathrm{sc}}(\mathbf{x}_{\mathrm{R}},\mathbf{x}_{\mathrm{n}})|^2+|\mathbf{E}_2^{\mathrm{sc}}(\mathbf{x}_{\mathrm{R}},\mathbf{x}_{\mathrm{n}})|^2+|\mathbf{E}_3^{\mathrm{sc}}(\mathbf{x}_{\mathrm{R}},\mathbf{x}_{\mathrm{n}})|^2, \tag{2.40}$$

when the k^{th} field intensity is:

$$\begin{aligned}|\mathbf{E}_k^{\mathrm{sc}}(\mathbf{x}_{\mathrm{R}})|^2&=\left(\sum_{n=1}^{N}\mathbf{E}_k^{\mathrm{sc}}(\mathbf{x}_{\mathrm{R}},\mathbf{x}_{\mathrm{n}})\right)\left(\sum_{n=1}^{N}\mathbf{E}_k^{\mathrm{sc}}(\mathbf{x}_{\mathrm{R}},\mathbf{x}_{\mathrm{n}})\right)^{*}\\&=\sum_{n=1}^{N}|\mathbf{E}_k^{\mathrm{sc}}(\mathbf{x}_{\mathrm{R}},\mathbf{x}_{\mathrm{n}})|^2+2\sum_{n=1}^{N}\sum_{\substack{m=1\\n\neq m}}^{N}Re\left\{\left(\mathbf{E}_k^{\mathrm{sc}}(\mathbf{x}_{\mathrm{R}},\mathbf{x}_{\mathrm{n}})\right)\left(\mathbf{E}_k^{\mathrm{sc}}(\mathbf{x}_{\mathrm{R}},\mathbf{x}_{\mathrm{m}})\right)^{*}\right\},\end{aligned} \tag{2.41}$$

and, thus, the coherent power becomes:

$$\mathbf{P}_c\approx\|\mathbf{E}^{\mathrm{sc}}(\mathbf{x}_{\mathrm{R}})\|^2=\sum_{n=1}^{N}\|\mathbf{E}^{\mathrm{sc}}(\mathbf{x}_{\mathrm{R}},\mathbf{x}_{\mathrm{n}})\|^2+2\sum_{k=1}^{3}\sum_{n=1}^{N}\sum_{\substack{m=1\\n\neq m}}^{N}Re\left\{\left(\mathbf{E}_k^{\mathrm{sc}}(\mathbf{x}_{\mathrm{R}},\mathbf{x}_{\mathrm{n}})\right)\left(\mathbf{E}_k^{\mathrm{sc}}(\mathbf{x}_{\mathrm{R}},\mathbf{x}_{\mathrm{m}})\right)^{*}\right\}, \tag{2.42}$$

Therefore, the difference between coherent Eq. (2.42) and incoherent Eq. (2.38) power expresses the interference term due to the mutual interaction between adjacent droplets. The existence of this interference term in the expression of the coherent scattered power implies that the coherent radiation is much stronger dependent on the properties of the medium than the incoherent radiation [Tishkovets et al., 2011].

$$\begin{aligned}\mathbf{P}_{int}=\mathbf{P}_c-\mathbf{P}_{inc}&=\left\|\sum_{n=1}^{N}\mathbf{E}^{\mathrm{sc}}(\mathbf{x}_{\mathrm{R}},\mathbf{x}_{\mathrm{n}})\right\|^2-\sum_{n=1}^{N}\|\mathbf{E}^{\mathrm{sc}}(\mathbf{x}_{\mathrm{R}},\mathbf{x}_{\mathrm{n}})\|^2\\&=2\sum_{k=1}^{3}\sum_{n=1}^{N}\sum_{\substack{m=1\\n\neq m}}^{N}Re\left\{\left(\mathbf{E}_k^{\mathrm{sc}}(\mathbf{x}_{\mathrm{R}},\mathbf{x}_{\mathrm{n}})\right)\left(\mathbf{E}_k^{\mathrm{sc}}(\mathbf{x}_{\mathrm{R}},\mathbf{x}_{\mathrm{m}})\right)^{*}\right\}\end{aligned} \tag{2.43}$$

It is often in radar meteorology that the interference term of Eq. (2.43) can be neglected , and therefore, the coherent and incoherent power are approximately equal. This is the assumption under which the classical radar theory is applicable. For the case of a randomly distributed assortment of scatterers, the ($m\neq n$)-terms give negligible contribution to the sum and they are eliminated. However, for a large collection of scatterers which are not perfectly random distributed in the medium, the contribution of the terms mixing $\mathbf{E}_k^{\mathrm{sc}}(\mathbf{x}_{\mathrm{R}},\mathbf{x}_{\mathrm{n}})$ and $\mathbf{E}_k^{\mathrm{sc}}(\mathbf{x}_{\mathrm{R}},\mathbf{x}_{\mathrm{m}})$, where $\mathbf{x}_{\mathrm{n}}$ and $\mathbf{x}_{\mathrm{m}}$ are sufficiently close, becomes essential. This is the case when some adjacent droplets come very close, form clusters and, hence, behave coherently.

Consequently, when the interference term is negligible and coherent power is approximately equal to incoherent power, the estimated power yields the same intensity as the one of a single sphere multiplied by N. However, when the interference term is not negligible, the coherent backscattered power contains structural information about the particular random medium and creates its distinctive scattering pattern [Huffman, 2011].

3 Spatial distribution of turbulent clouds

Turbulent clouds illustrate the great range of spatial scales and the sharp boundaries characteristic of such systems. Similarly, a series of pictures taken in succession would illustrate the large range of temporal scales. Particles' mixing due to the presence of turbulence in clouds implies the existence of correlation, the so-called droplets preferential concentration. The notion of turbulent clustering can be approached by a statistical homogeneous spatial correlated random process. This serves as motivation for quantifying correlations in droplet positions as a function of spatial scale.

3.1 Atmospheric turbulence

By definition, atmospheric turbulence is considered as small-scale irregular air-motions characterized by winds that vary in speed and direction. Turbulence is important because it mixes the atmosphere and, consequently, water vapor, smoke and cloud droplets, as well as energy, become distributed both vertically and horizontally [Britannica, accessed April 18, 2012]. Turbulence is responsible for the clouds formation and their precipitation events. The causes of turbulence differ in heights/ layers of the atmosphere.

1. Low-level turbulence, such as the mechanical Boundary Layer Turbulence is mainly produced due to the terrain topography. Mechanical turbulence is the effect of the wind shear due to orographic changes in the surface. Wind shear occurs when wind changes speed or direction. A series of mountains or any high-altitude mountain may cause the so-called Mountain wave turbulence. Waves develop on the mountain or on the leeward side. Extraordinary clouds are formed as the result of high velocity winds forced over a mountain. The air starts moving in wave-like layers. If the air contains sufficient moisture, altocumulus standing lenticular (ACSL) clouds will form. In the vicinity of lenticular formations and mountain wave activity, rotor clouds may form at a lower altitude that the mountain ridge. These clouds are small cumulus-like clouds [Reynolds, 2011].

2. In low altitudes, convective currents are also a common cause of low-level turbulence. These currents are ascending and descending localized vertical air movements. The downward currents have lower vertical speed than the rising currents. The unstable heated at the surface air forces warm air masses

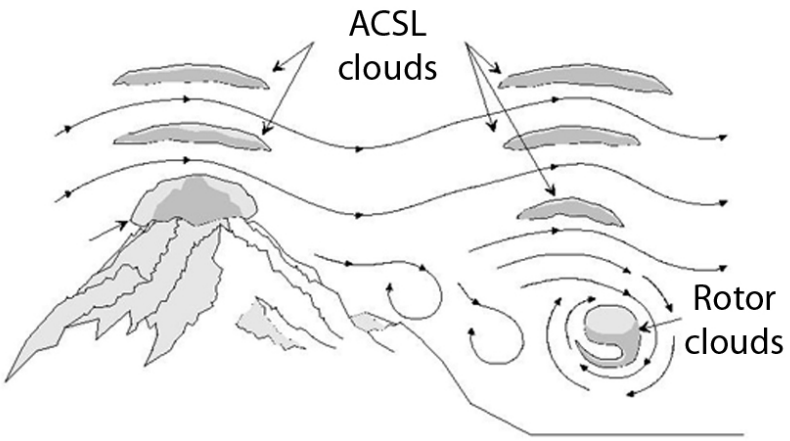

Figure 3.1: *Mountain wave turbulence. Mountain waves result in the development of altocumulus standing lenticular (ACSL) clouds over the mountain, while, close to the lenticular formations, rotor clouds form at altitudes lower than the mountain ridge.*

upwards. While surface heating increases, convection increases to higher heights. As convective current keeps on moving upwards until its temperature reaches the surrounding air temperature. If it cools to the saturation point, a cloud forms. More severe type of convective turbulence is caused when convective currents form cumulus or cumulonimbus clouds [FAA, 1975].

3. The most frequent medium or high-level turbulence is the Clear-air turbulence (CAT). CAT is produced by erratic air currents that occur in cloudless air between altitudes of 7-12km. In general, CAT is caused by two mechanisms: the Kelvin-Helmholtz instability and mountain waves. Kelvin-Helmholtz waves develop in the presence of large vertical wind shear and their breaking causes turbulence [Overeem, 2002].

4. Another type of turbulence which can be visible is the wake turbulence created by the motion of airplanes or helicopters. Large clouds are formed over the wings just after the airplane takes off or during landing. Mainly, wake turbulence is the product from the formation of wake vortices. The latter occur when air moves outwards under the wing, towards the wingtip and curl up and over the upper surface of the wing [CAA, 2007].

Figure 3.2: *Wake turbulence as it was captured in this picture when a British Airways flight was descending through thin clouds near London in July 2006 [Stellin, 2007].*

Elements of turbulent motion, the so-called eddies, appear at different length-time scales, from centimeters and seconds to kilometers and days. Most of kinetic energy of turbulent motion is contained in the large-scale structures. However, the large motions tend to break down in smaller-scale motions and this process, which is called 'turbulent cascade', creates a hierarchy of eddies. The different length scales of eddies are characterized by the turbulence spectrum. The turbulence spectrum is a plot of the energy distribution of eddies according to the wavelength or frequency. The dependence of eddies on the frequency results into the classification of turbulence at macro-, meso- and micro turbulence [Foken, 2008]. The spectral range of atmospheric turbulence is depicted in Fig.3.3. Microturbulence occurs at frequencies larger than $10^{-3}Hz$, where there is production of energy and is separated by the rest spectra by a distinctive minimum, the so-called spectral gap [Weber, 2007].The cascading process terminates when viscous dissipation of energy takes place. This is the smallest spatial-temporal scale, the so-called Kolmogorov microturbulence, which happen at the highest frequencies of the turbulence spectrum. Especially in Kolmogorv spectrum, turbulence is considered locally isotropic and homogeneous [Kolmogorov, 1991].

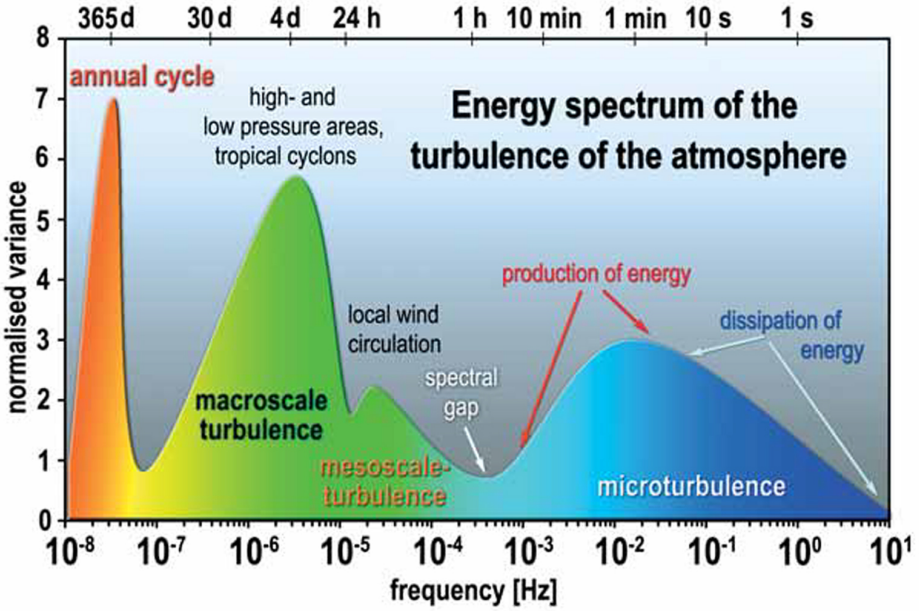

Figure 3.3: *Schematic plot of turbulence spectra of a 3-year atmospheric turbulence variations. The part of spectrum, called microturbulence, where there is energy production, is separated by the rest spectra by a distinctive minimum, the so-called spectral gap. Microturbulence appears for frequencies larger than* $10^{-3}Hz$ *and the time spam of microturbulence is limited from hours to seconds [Weber, 2007].*

In general, turbulence develops in a fluid when the *Reynolds number* exceeds a certain critical value (i.e., transition from laminar to turbulent flow) [Kanda, 2007]. *Reynolds number* is an important dimensionless number characterizing turbulent fluids and gases [Dullemond, 2011]:

$$Re = \frac{LV}{v}, \tag{3.1}$$

where V is the flow velocity, v is the kinematic viscosity of the fluid and L it the characteristic length. The kinematic viscosity of air depends on many parameters, such as the air temperature and density. The largest Reynolds numbers present in the atmosphere are in the range 10^6 to 10^8.

3.2 Turbulence effects

The existence of turbulence in clouds can affect their lifetime. This is a matter of clouds efficiency to form rain (i.e., how fast rain develops from cloud droplets). More specifically, turbulence results in acceleration

of rain initiation. According to a large part of the cloud physicists community, clouds efficiency to produce rain through the faster evolution of drop size distribution is enhanced by particle-turbulence interactions. In [Shaw, 2003], the effect of particle-turbulence interactions on the microphysical properties of clouds is investigated in two levels: the growth of large drops through collision-coalescence and the growth of cloud droplets by condensation. Primarily research showed that the influence of turbulence on the condensation process seems limited and, most consensus has been grown on the influence of turbulence on collision rates. Especially, small-scale turbulence is prone to be more effective on collision-coalescence rates.

The process of collision and coalescence allows droplets to grow to a size large enough to fall from a cloud as rain. The community of cloud scientists is divided upon the influence of turbulence on collision rate of droplets due to change in collision and coalescence efficiencies between droplets [Frankin, 2009]. In [Koziol and Leighton, 1996], the effect of small-scale turbulence on collision rates of small droplets is very weak and, most possibly negligible. Nevertheless, the interaction of cloud particles with turbulence is possible to have an impact on the growth of large drops through collision-coalescence [Shaw, 2003]. Therefore, there are open questions on whether or not turbulence influences the droplet growth and the size distribution in clouds through broadening of the drop size spectra. In particular, scientific research on the potential broadening of the droplet spectrum during the early stages of the cloud formation showed that the turbulence-induced mechanisms among clouds result in broader drop size spectra while turbulence decreases the minimum size of droplets, able to collide with smaller drops [Pinsky and Khain, 1997]. Turbulence results in changes in the droplet velocities because of the change in drop size distribution. One mechanism that possibly leads to different drop size distribution is the inertia-induced relative velocities between drops falling within the turbulent cloud. The maximal broadening of cloud spectrum occurs in areas of high turbulence intensity in clouds. Since terminal fall velocity is thought to be a function of drop mass, the larger drops fall faster than smaller drops. Due to this difference in terminal fall velocities, collisions between droplets of indifferent size take place in the vertical direction. The gravitational collision rates may be enhanced in the presence of eddies.

Even though it is almost widely accepted that drop growth evolves faster in clouds when turbulence is present, this does not guarantee that collision efficiencies[1] and coalescence efficiencies[2] increase. In general, collisions of droplets mainly occur through the differential response of droplets to gravitational forces. However, for the formation of precipitation, and more specifically for rain formation, collision process is not enough. Coalescence should follow after the collision. When a pair of droplets collide, the possible scenarios are:

1. they may bounce apart,

2. they may coalesce and remain permanently united,

3. they may coalesce temporarily and separate, apparently retaining their initial identities,

4. they may coalesce temporarily and then break into a number of small drops.

Which of the above scenarios is prone to happen, strongly depends on the drop sizes and the collision trajectories, but it is also influenced by other factors, like the existing electrical and aerodynamical forces. The existence of turbulent motions is also another crucial factor. Finally, the growth of a droplet by collision-coalescence process is governed by the collection efficiency, which is the product of collision efficiency and coalescence efficiency [Rogers, 1979].

[1] Collision efficiency is the ratio of the actual number of collisions to the number for complete geometric sweep-out. Sweep-outs occur because when a drop falls, it collides with only a fraction of the droplets in its path and the rest is swept aside in the airstream around the drop. Collision efficiency is primarily dependent on the size of the collector drop and, secondly, on the sizes of the collected droplets [Rogers, 1979].

[2] Coalescence efficiency is the ratio of the number of coalescences to the number of collisions [Rogers, 1979].

3.2.1 Effect of turbulent clustering on the rain formation

The debate over whether turbulence significantly enhance the collision-coalescence process reinforce the interest of scientists on providing evidence of droplets preferential concentration, the so-called turbulent clustering. Droplets of different size tend to cluster in different regions of the cloud because of their differing inertial responses to flow accelerations, both gravitational and turbulent accelerations [Franklin et al., 2006]. This means that turbulence causes inhomogeneous distribution of droplets in the cloud. Droplets' clustering is strongly dependent on the scale of existing turbulence in the cloud. More specifically, small-scale turbulence with high Reynolds number is pertinent to significant preferential concentration [Kostinski and Shaw, 2001].

The acceleration of rain initiation due to the fast growth of droplets was discussed in 3.2. However, the role of turbulent clustering in the increase of collision-coalescence rates is not further explained. Turbulent clustering attracted a lot of attention from cloud scientists because of the existing assumption of zero correlation between cloud droplets in the collision-coalescence process. In other words, the condition for calculating the probability of a collision is the memoryless nature of droplets. This simply means that the collision-coalescence rates are computed under the assumption of non-correlated particles. In particular, the expected time that is required for any droplet r to experience collision with another droplet r' is given when spatial structure of clouds is described as a perfect random process. Suppose $n_{r'}$ denotes the number density of droplets of size r' and $\kappa(r,r')$ is the collision kernel, which expresses the exact functional form depending on the physical mechanism causing the collisions[3]. Then, the expected time for a collision to occur is defined as [Reif, 1980]:

$$\tau = (n_{r'}\kappa(r,r'))^{-1}, \tag{3.2}$$

and the probability density of collision times is exponentially distributed:

$$p(t) = \frac{1}{\tau} exp\Big(-\frac{t}{\tau}\Big). \tag{3.3}$$

After each collision, $\tau(r)$ must be recalculated because the droplet radius has changed and the collision kernel changed too. Finally, after n_r droplets that experience collision, the total collision rate N_c, which denotes the number of collisions per time, per volume is:

$$N_c = n_r n_{r'} \kappa(r,r'). \tag{3.4}$$

Therefore, it is straightforward that if the assumption of zero correlation is violated, Eq (3.2) and (3.3) are not valid, and the total collision rate given by Eq. (3.4) is not accurately predicted. The deviation of the actual collision rate from the theoretical value calculated by Eq. (3.4) is most probably due to the presence of spatial correlation and, thus the clustering effect of turbulence.

3.2.2 Effect of turbulent clustering on the energy budget

The large impact of clouds on the radiative heat budget of Earth is well-known. For improving the predictions of climate change, the uncertainties in evaluation of cloud radiation should be eliminated. This is a reason why the effect of turbulence on cloud radiation has been an issue under investigation recently. For calculating the radiative transfer, the spatial structure of turbulent clouds, and the relevant sizes and phases of their droplets are important to be estimated [Bartello et al., 2010]. In particular, the well-understanding of clustering effect on radiative transfer is a research question of high importance.

The radiative transfer is expressed by considering two kinds of radiation: the shortwave and the long-wave radiation. Shortwave radiation (i.e., visible light) can travel through a cloud without being absorbed by its particles, however long-wave radiation (i.e., infrared radiation) is partially absorbed by cloud particles. Therefore, the impact of atmospheric turbulence on the radiative properties of clouds is linked to the

[3]Here, the term collisions is used for simplicity instead of the word "collection", which refer to the combination of collision and coalescence

spatially-correlated particle distribution. Researchers have mostly studied the effect of turbulent clustering on radiative transfer in a theoretical level. In practice, the effect of turbulent clustering on radiative transfer can be evaluated by two numbers related to clouds radiative properties, the Reynolds number and the Stokes number[4]. Nevertheless, some primary computational results presented in [Matsuda et al., 2011] showed that turbulent clustering does not influence the total transmittance of visible radiation while it increases the total transmittance of infrared radiation. The scientists, who performed the simulations, give the interpretations for these results. They claim that the clustering of droplets allows more photons to pass through clouds without being scattered than in the case of the random dispersion of droplets. The simulations proved that the effect of turbulent clustering on radiative transfer decreases as the turbulent Reynolds number increases, while Stokes number decreases.

3.3 Statistics for the position of droplets inside the cloud volume

In any random medium consisting of particles, the positions of particles is an indication of the random medium. Since clouds are considered as random media, the propagation and scattering of electromagnetic radiation through clouds should be linked to the spatial and temporal distribution of droplets. The spatial distribution of droplets in a cloud can be statistically characterized. Firstly, the notion of randomness should be introduced to this study. Assume that the number of droplets inside the cloud volume is a random variable, but still countable. Then, the perfect randomness for a collection of particles can be considered as a statistically homogeneous Poisson process where the position of particles is uniformly distributed in the cloud volume and completely uncorrelated (i.e. statistically independent). On the other hand, in case of non-statistically independent particle positions (i.e., turbulent clustering), the random process is still statistically homogeneous but not spatial uncorrelated any more. Statistical homogeneity of this random process denotes that the mean particle density is spatially independent and non-deterministic. As a result, in case of turbulent clustering, the randomness is not perfect since the positions of particles are correlated. Thus, it is obvious that spatial correlation implies a deviation from perfect randomness.

3.3.1 The notion of random process

For the understanding of fundamental processes in atmospheric clouds, the stochastic structure of clouds should be well-demonstrated. The random distribution of cloud particles in space can be considered as a homogeneous but correlated random process. Let n be the random variable for the number of droplets in a given unit volume. Then, a random process is characterized as statistically homogeneous if and only if the moments of the random process $n(\mathbf{x})$ (such as the mean and the variance) are unaffected by shifts in the choice of origin. Fine-scale physical inhomogeneities (like patchiness of clouds) do not imply statistical inhomogeneity [Kostinski and Jameson, 2000].

The patchiness of clouds is caused by the mixing of droplets by turbulence or droplet-turbulence interactions. Patchiness violates the perfect randomness assumption which denotes statistically uniform and independently distributed positions of droplets in homogeneous unmixed clouds. The assumption of cloud droplets spatially distributed in a perfect random manner has been considered a presupposition for the development of various cloud physical theories. For instance, the stochastic collection equation describing the growth of droplets via collision coalescence has been demonstrated under the perfect randomness assumption [Telford, 1955].

A statistically homogeneous but correlated random process can be better understood through the following statement [Landau et al., 1980]:
" The assertion of the particles of a homogeneous isotropic body (liquid or gas) are equally likely to be at any position in space, applies to each separate particles on condition that all the other particles can have arbitrary positions. This assertion certainly does not contradict the fact that, owing to their interaction, there must exist

[4]Stokes number (Sk) is a dimensionless parameter that describes a particle's flow in a particular fluid (e.g., snow in air) [Nguyen and Wereley, 2002].

some correlation between the relative positions of the different particles. This means that if we consider, say, two particles at the same time, then for a given position of one particle, different positions of the other will not be equally probable".
Therefore, the so-called small-scale inhomogeneities mentioned in cloud physics are manifestation of correlation. The stochastic structure of clouds can be materialized through the pair-correlation function. Let two volume elements dV_1 and dV_2 be sufficiently small such as they contain either zero or one particle. Because of the small volumes, the probability of containing two or more particles is negligible. Thus, for a fixed local mean concentration $\overline{c}$, the average number of particles $\overline{c}dV$ expresses the probability that a particle is in the volume element dV [Landau et al., 1980].

In general, for a statistically homogeneous random process, the joint probability $P(1,2)$ of finding two particles in the two volumes dV_1 and dV_2 (i.e. each of the volumes contains one particle):

$$P(1,2) = \overline{c}^2 dV_1 dV_2[1 + \eta(l)], \tag{3.5}$$

where $\eta(l)$ is the pair correlation function, and l is the separation distance between two volumes. The pair correlation function is defined as:

$$\eta(l) = \frac{[\overline{n(l)n(0)} - \overline{n}^2]}{(\overline{n})^2} = \frac{\overline{n(l)n(0)}}{(\overline{n})^2} - 1, \tag{3.6}$$

where $n = cV$ and V is the test volume.

3.3.2 Perfect randomness: Poisson process

The state of perfect randomness is represented by the particle positions being independently distributed with uniform probability in the cloud volume. In terms of the fluctuating number of droplets, this state corresponds to the homogeneous Poisson process. The Poisson process is ideally random in the sense that only in the case of the Poisson process no blobs or voids of any length scale are present inside the cloud. Thus, the Poisson field is as even as randomness allows.

The assumption of perfect randomness which requires statistical independence of particles' positions in non-overlapping volumes is ensured if and only if Eq.(3.5):

$$P(1,2) = P(1)P(2) = \overline{c}dV_1\overline{c}dV_2 = \overline{c}^2 dV_1 dV_2. \tag{3.7}$$

Hence, perfect randomness implies that pair correlation function is zero.

In the current report, the term perfectly random is used to characterize a random, countable variable that is described by a Poisson probability density function (p.d.f.) with no correlations at any scale. Suppose that at a given cloud volume δV sufficiently small such as the probability of detecting more than one droplet is vanishingly small and the position of cloud droplet is a random countable variable. The counting random process is a Poisson process under the following assumptions [Ochi, 1990]:

1. all particle positions are uniformly and identically distributed random variables,
2. the process is statistically homogeneous,
3. particle positions are statistically independent of each other at any length scale.

Then, the random number of particles $n = n(V)$, in a test volume V, is distributed according to:

$$p(n) = \frac{\overline{n}^n exp(-\overline{n})}{n!}, \tag{3.8}$$

where $p(n)$ is the probability of finding n particles in a test volume and $\overline{n} = \overline{n(V)}$ is the mean number of particles in V. In Fig. 3.4 a statistically homogeneous Poisson process is depicted, where particle positions are uniformly, identically and independently distributed random variables. Actually, Fig. 3.4 provides the standard of "perfect randomness" for dilute systems of particles.

As a property of the Poisson distribution, the variance of the number of particles in V is equal to the mean $\sigma_n^2 = \overline{n}$.

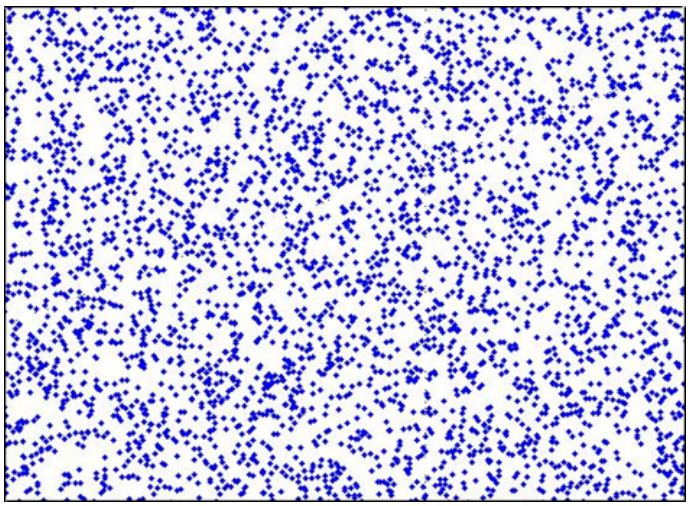

Figure 3.4: *Statistically homogeneous Poisson process. Particle positions are uniformly, identically and independently distributed random variables. It provides the standard of "perfect randomness" for dilute systems of particles.*

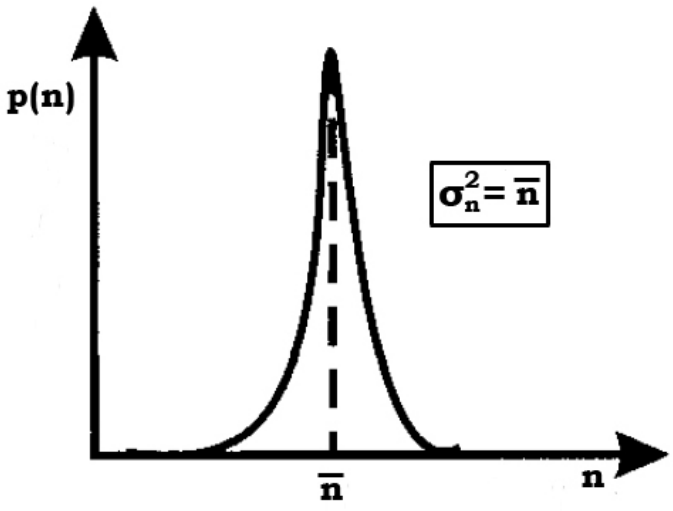

Figure 3.5: *Probability density function of Poisson distribution. The probability $p(n)$ of finding n droplets in a test cloud volume V is illustrated here. The mean number of droplets $\overline{n}$ is equal to the variance.*

3.3.3 Spatial correlation: Non-Poisson process

Lack of statistical independence in particle positions allows the formation of voids. The presence of voids results in violation of the third assumption for the validity of the Poisson process. Thus, the spatial correlation lead to a deviation from the Poisson random process because the particle positions cannot be considered as independent random variables. The position of voids are not predictable, but they are uniformly distributed random variables [Shaw et al., 2002]. The process is called statistically homogeneous but spatially correlated (Non-Poisson) random process and it is illustrated in Fig.3.6.

3.4 Deviation from perfect randomness: A measure for droplet clustering

Generally, in a random process, any dispersion about the mean value is considered as a measure of randomness. Since the number of droplets in a given cloud volume is a random process, any deviation from perfect randomness results in a dispersion about the mean number of droplets $\overline{n}$. In Fig.3.7, the left plot represents the Poisson process where there is lack of correlation between droplets, whilst fluctuation around the

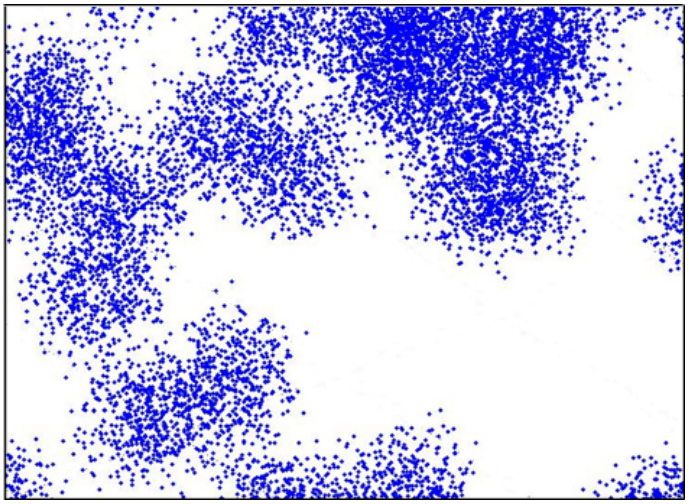

Figure 3.6: *Statistically homogeneous but spatially correlated (not Poisson) random process. Particle positions are uniformly distributed but not independent random variables. Voids are present. However, their centers are uniformly distributed random variables. This figure is obtained by the code developed for the purposes of this research, as well as Fig. 3.4.*

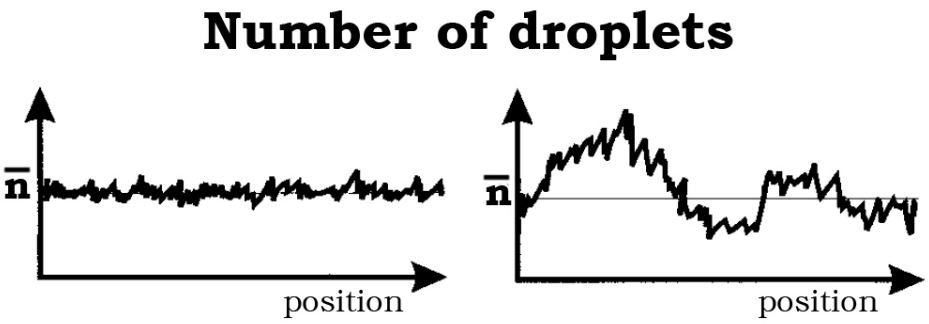

Figure 3.7: *Measure of randomness in a random process. Any dispersion about the mean value is considered as a measure of randomness. Hence, for a number of droplets random process, any deviation from perfect randomness results in a dispersion about the mean number of droplets $\overline{n}$ at a given cloud volume V. The left plot represents the Poisson process where there is lack of correlation between droplets, whilst the right plot shows a spatially-correlated (Non-Poisson) random process with fluctuations around the mean value. Original figure is taken in [Kostinski and Jameson, 2000], but it is modified according to the notation used in this thesis.*

mean value depicted in the right plot implies a spatially-correlated (Non-Poisson) random process.

The deviation from perfect randomness and the homogeneous Poisson random process is defined as "patchiness". The pair correlation function described in Eq.(3.6) is a measure for quantifying "patchiness". The pair-correlation function is zero for perfect randomness. It has a lower bound of -1 for spatial scales smaller than the diameter of impenetrable particles. If the pair-correlation function is greater than zero, it implies that if a droplet is encountered at a given position in a cloud, there is an enhanced probability of finding another droplet at a distance l. In Fig.3.8, a comparison between the pair correlation functions with respect to the separation distance l is illustrated. The left plot depicts the constant zero pair correlation function for the case of perfect randomness, when there is absence of spatial correlation between droplets. On the contrary, the right plot shows the fluctuating non-zero pair correlation function for patchy clouds, with correlated droplets [Kostinski and Jameson, 2000]. Pair correlation function can be either positive as long as the separation distance between two droplets is smaller than the one of the perfect randomness case or negative for larger separation distances. Therefore, positive and negative correlation regions may appear simultaneously inside the cloud volume.

The pair-correlation function is related to the radial distribution function $g(l)$, which measures the

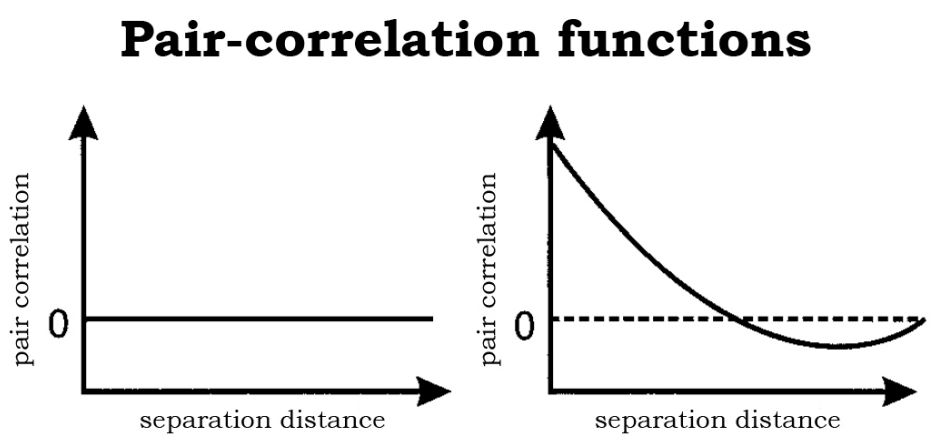

Figure 3.8: *A comparison between the pair correlation functions $\eta(l)$ with respect to the separation distance l of the two volumes dV_1 and dV_2, as this is mathematically formulated in Eq.*(3.6). *The left plot depicts the constant zero pair correlation function for the case of perfect randomness, when there is absence of spatial correlation between droplets, while the right plot shows the fluctuating non-zero pair correlation function for patchy clouds, with correlated droplets [Kostinski and Jameson, 2000].*

spatial correlations that exist between droplet positions. Particularly, $g(l) = \eta(l) + 1$ and, hence, in the absence of correlation $g(l) = 1$. In [Franklin et al., 2006], the radial distribution function reaches the value of 5 upon turbulent mixing conditions. Clustering of droplets strongly depends on the drop size distribution in the cloud volume. Droplets of different size tend to cluster in different regions of the flow because of their differing inertial responses to flow accelerations. More precisely, the amount of clustering increases with the radius ratio and turbulence intensity. The radius ratio is defined as the ratio of the smaller drop radius over the collector's drop[5] radius [Franklin et al., 2006].

Another measure of droplet clustering is the variance-to-mean ratio, the so-called clustering index CI [Baker, 1992]:

$$CI(V) = \frac{\overline{(\delta n)^2}}{\overline{n}} - 1, \tag{3.9}$$

where $\sigma_n^2 = \overline{(\delta n)^2} \equiv \overline{(n - \overline{n})^2}$ is the variance. For perfect randomness CI is zero at any given test volume V. When positive spatial correlations are dominant in V, clustering index becomes positive. Clustering index has been approved as a valuable tool for quantifying the degree of droplet clustering in clouds. However, the clustering index is thought to contain an inherent "memory" of all scales within volume V because its value at a given scale contains contributions from all smaller scales [Kostinski and Shaw, 2001]. For retrieving a scale-localizable measure of droplet clustering, the correlation-fluctuation theorem, as it is developed in [Landau et al., 1980], is used:

$$\frac{\overline{(\delta n)^2}}{\overline{n}} - 1 = \frac{\overline{n}}{V} \int_V \eta(l) dV, \tag{3.10}$$

where, $\eta(l)$ is the pair-correlation function expressed by the mathematical formula of Eq.(3.6) and the mean number of droplets in volume V is $\overline{n} = \overline{c}V$, where $\overline{c}$ is the local mean concentration.

From Eq.(3.10), it is derived that the variance of number of droplets $\overline{(\delta n)^2}$ in a given volume V is related to the pair-correlation function integrated over the same volume. In terms of physical interpretation, Eq.(3.10) states that, under the assumption of a fixed mean concentration $\overline{c}$, the variance $\overline{(\delta n)^2}$ is enhanced

[5]The collector drop is the falling drop which collide with smaller drops present in its path.

by a term $\overline{\eta}\overline{n}^2$ in the presence of correlation between droplets' positions. Thus, in case of statistical homogeneous Non-Poisson process, the variance is given as [Shaw et al., 2002]:

$$\overline{(\delta n)^2} = \overline{n} + \overline{\eta}\overline{n}^2, \tag{3.11}$$

where the volume-averaged pair correlation function $\overline{\eta}$ is defined as:

$$\overline{\eta} = \frac{1}{V}\int_V \eta(l)dV. \tag{3.12}$$

The probability density function of a Non-Poisson distribution is illustrated in Fig.3.9.

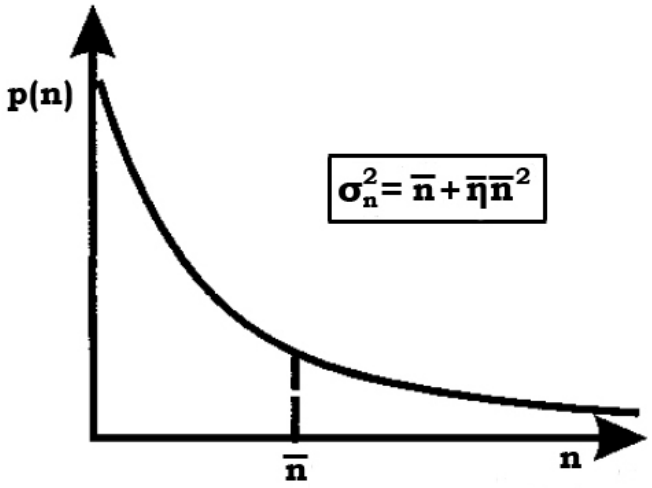

Figure 3.9: *Probability density function of a Non-Poisson distribution. The probability $p(n)$ of finding n droplets in a test cloud volume V is illustrated here in the presence of spatial correlation between droplets. The variance is enhanced by a term $\overline{\eta}\overline{n}^2$. The plot is taken and adapted from [Kostinski and Jameson, 2000].*

While the dimensions of the test cloud volume V becomes much larger in comparison with the correlation distance, most of the integration region in $\overline{\eta}$ does not contribute and, hence, the volume-averaged pair-correlation function is approximately zero. Then, the Poissonian relation $\sigma_n^2 = \overline{n}$ is recovered. Same result occurs if negative and positive correlation regions of the test volume cancel each other [Kostinski and Jameson, 2000].

Using the Random Walks approach, which is explicitly discussed in Chapter 4, the additional term $\overline{\eta}\overline{n}^2$ in Eq.(3.11) can be expressed as the coherent displacement of the walker, if n symbolizes the random number of steps [Kostinski and Jameson, 2000]. In this thesis, Random Walks theory is the statistical tool used for quantifying droplets clustering through an analysis of the coherent radar backscattering power.

4 Random Walks Theory

Random Walk is an empirical approach, which can be used as a valuable tool for extracting the statistical properties of electromagnetic waves scattered by objects containing few scattering centers. The random walk model is quite useful for providing a much physical insight into the scattering problem. In particular, Pearson's walk in plane can be used for studying the distribution of backscattered electric field and the relevant backscattered power with respect to the degree of clustering among cloud droplets.

4.1 General concept of a random walk in plane

Definition of a random walk: Let $\left\{\mathbf{Y}_j\right\}_{j=1}^{\infty}$ be a sequence of independent, identically distributed discrete random variables. For each positive integer n, we let $\mathbf{S}_n$ denote the sum $\mathbf{Y}_1 + \mathbf{Y}_2 + ... + \mathbf{Y}_n$. The sequence $\{\mathbf{S}_n\}_{n=1}^{\infty}$ is called a random walk.

Suppose that the j$^{\text{th}}$ random complex number $\mathbf{Y}_\text{j}$ has an amplitude A_j and a phase ϕ_j. The amplitude A_j denotes the j$^{\text{th}}$ step of the random walk and the phase ϕ_j denotes the j$^{\text{th}}$ step direction of the walk. All step directions are equally probable. Each random complex number is represented by a vector in the complex plane. In Fig.4.1, a random walk in the complex plane is illustrated.

In general, the sequence of $\mathbf{Y}_\text{j}$'s are considered as the outcomes of independent experiments. A random walk can be seen as a concept to study the sum of n random complex numbers and then describe the distribution and density functions of this sum [Grinstead and Snell, 1997]. In other words, by joining the origin (0,0) of the complex plane with the end point of the random walk, the resulting vector denotes the sum of n random vectors.

4.1.1 Statistical Properties of a random walk

The model describes a way to derive information about the mean value and the variance of a walker's location, provided that the individual displacements have finite mean or finite variance [Hughes, 1995]. Suppose that the walker has traveled n steps. If the random vector $\mathbf{Y}_\text{j} = A_j e^{i\phi_j}$ indicates the displacement

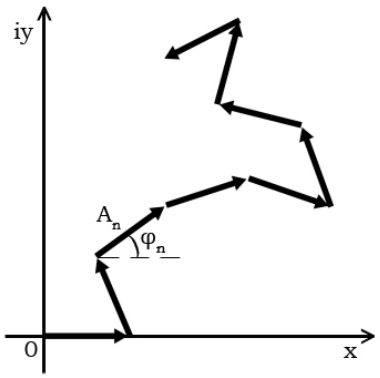

Figure 4.1: *Representation of a random walk. Each vector in the complex plane represents a random number. The j^{th} random complex number $\mathbf{Y}_j$ has an amplitude A_j and a phase ϕ_j. The amplitude A_j is the j^{th} step of the random walk and the phase ϕ_j is the j^{th} step direction of the walk. All step directions are considered equally probable. The resultant field is given as the vector sum in the complex plane.*

on the j^{th} step, the position of the walker after n steps is denoted as $\mathbf{R}_n = \sum_{j=1}^{n} \mathbf{Y}_j$. Thus, the probability density function for the position $\mathbf{R}_n$ is symbolized as $P_n(\mathbf{r})$. Assuming, without loss of generality, that the walker starts from $\mathbf{r} = \mathbf{0}$ and given the fact that the total number of steps N is finite but very large, the probability density function of the position $\mathbf{R}_N$ is approximated by the expression [Hughes, 1995]:

$$P_N(\mathbf{r}) \approx \frac{1}{\pi N \alpha^2} \exp\left(- \frac{|\mathbf{r}|^2}{N\alpha^2} \right), where \tag{4.1.1}$$

1. for a walk with constant step length $\alpha_\ell = \alpha_{\ell+1}$, $\forall \ell = 1, 2, ..., N-1$:

$$\alpha^2 = \alpha_\ell^2 \tag{4.1.1a}$$

2. for a walk with variable but deterministic step length: $\alpha_\ell \neq \alpha_{\ell+1}$, $\forall \ell = 1, 2, ..., N-1$:

$$\alpha^2 = \frac{1}{N} \sum_{\ell=1}^{N} \alpha_\ell^2 \tag{4.1.1b}$$

3. for a walk with variable step length ℓ with a known p.d.f. $w(\ell)$:

$$\alpha^2 = \int_0^\infty \ell^2 w(\ell) d\ell < \infty. \tag{4.1.1c}$$

4.1.2 Coherent scattering problem approached by random walk theory

Suppose that the k^{th} component of the electric field backscattered by the individual m^{th} cloud droplet is represented as the complex number $A_m e^{i\phi_m}$, if the time factor $exp(i\omega t)$ is not considered for simplification. Each k^{th} component backscattered electric field is represented by a vector in the complex plane. Thus, the resultant field given as a vector sum in the complex plane represents the k^{th} component of the total backscattered electric field derived in Chapter 2. In Fig. 4.1, the vectors in the complex plane representing n backscattered electric fields corresponding to n droplets present in the cloud volume constitute a *random walk*. Since cloud is a random medium, this vector sum is also random. The probability distribution of the total backscattered electric field and the relevant power can be derived through the random walks theory. The statistical properties of a walker's location after n steps can be linked to the statistical properties of the

k^{th} component of the total backscattered electric field and the relevant power [Beckmann and Spizzichino, 1987].

In section 2.2.4, the k^{th} component of the total scattered field is mathematically expressed by equation 2.31. The number of particles inside the illuminated cloud volume n corresponds to the the total number of steps that the walker has traveled. The scattering amplitude contribution A_m of the m^{th} droplet of the total backscattered field measured at the receiver corresponds to the walker's step length. After N individual backscattered fields have been coherently summed, the k^{th} component of the total backscattered field measured at the receiver's position is expressed as the complex vector:

$$\mathbf{E}_k^{\mathrm{sc}}(\mathbf{x}_\mathrm{R}) = \sum_{n=1}^{N} \left(\left| \mathbf{E}_k^{\mathrm{sc}}(\mathbf{x}_\mathrm{R}, \mathbf{x}_\mathrm{n}) \right| \cdot \exp(i\theta_\mathrm{n}) \right) \tag{4.1.2}$$

Each m^{th} scatterer contributes to the amplitude of the total field with a component $A_m = \left| \mathbf{E}_k^{\mathrm{sc}}(\mathbf{x}_\mathrm{R}, \mathbf{x}_\mathrm{m}) \right| = \frac{3k_b^2}{(4\pi)^2} \frac{1}{|\mathbf{x}_\mathrm{R} - \mathbf{x}_\mathrm{m}|^2} V_\mathrm{m} \left| \frac{\epsilon_m - 1}{\epsilon_m + 2} \right| \mathbf{D}_{km}$, which corresponds to the length of walker's m^{th} step. As it was developed in section 4.1.1, the walker's step length can be either constant, variable but deterministic or variable but weighted with a factor $w(\ell)$. These three cases will be physically interpreted for the different scattering radiation patterns [Jakeman and Tough, 1988].

1. When the particles are spherical or so small that their individual radiation patterns are spherically symmetric, for each m^{th} particle, $\left| \mathbf{E}_k^{\mathrm{sc}}(\mathbf{x}_\mathrm{R}, \mathbf{x}_\mathrm{m}) \right| = constant$ and the case is treated as a random walk with constant step length.

2. When the particles are not spherical but they are assumed to be statistically identical, the amplitude contribution $\left| \mathbf{E}_k^{\mathrm{sc}}(\mathbf{x}_\mathrm{R}, \mathbf{x}_\mathrm{m}) \right|$ by each m^{th} particle varies and the case is treated as a random walk with variable but deterministic step length.

3. Finally, if the particles are neither spherical nor statistically identical, the statistical properties of the amplitude contributions $\left| \mathbf{E}_k^{\mathrm{sc}}(\mathbf{x}_\mathrm{R}, \mathbf{x}_\mathrm{m}) \right|$ and $\left| \mathbf{E}_k^{\mathrm{sc}}(\mathbf{x}_\mathrm{R}, \mathbf{x}_\mathrm{n}) \right|$ due to the m^{th} and n^{th} scatterer, respectively, vary and the case is treated as a random walk with variable step length with a known p.d.f.

The mean-square displacement α^2 in formula 4.1.1 is easily computed for the first two cases. However, the computation of α^2 at the third case is more complicated since the scattering amplitude contribution due to the m^{th} particle, A_m, is expressed as a function of the random variables $\frac{1}{|\mathbf{x}_\mathrm{R} - \mathbf{x}_\mathrm{m}|^2}$, V_m, $\left| \frac{\epsilon_m - 1}{\epsilon_m + 2} \right|$, $\mathbf{D}_{km}$. By assuming that these random variables are independent, the probability density function of A_m, $f(A_m)$, can be estimated as the product of these four variables' probability density functions [Papoulis, 1965].

Hence,

$$f(A_m) = f\left(\frac{1}{|\mathbf{x}_\mathrm{R} - \mathbf{x}_\mathrm{m}|^2} \right) \cdot f(V_\mathrm{m}) \cdot f\left(\left| \frac{\epsilon_m - 1}{\epsilon_m + 2} \right| \right) \cdot f(\mathbf{D}_{km}) \tag{4.1.3}$$

For the sake of simplicity, the dependence of scattering amplitude contribution A_m on the ratio $\left| \frac{\epsilon_m - 1}{\epsilon_m + 2} \right|$ can be eliminated since only water droplets are considered inside the cloud volume. Moreover, the dependence on $\mathbf{D}_{km}$ is also negligible because the backscattering angle β_m can be considered almost constant for each illuminated m^{th} cloud droplets. Finally, due to the fact that radar backscatter is measured at far field, the contribution of the ratio $\frac{1}{|\mathbf{x}_\mathrm{R} - \mathbf{x}_\mathrm{m}|^2}$ is negligible too. Therefore, the amplitude A_m is certainly dependent on the particle volume V_m, thus on the drop size. In the presence of correlation among particles, the amplitude A_m is also dependent on particle's position random variable and, thus, on the r.v. $\frac{1}{|\mathbf{x}_\mathrm{R} - \mathbf{x}_\mathrm{m}|^2}$ too.

The case of water clouds, where the droplets are spherical and small compared to the radar wavelength is treated as the Case 1 of a random walk in plane with constant step length. The drop size can be considered either constant or in a distribution, where some droplets are larger than other ones.

4.2 Statistical properties of Pearson's walk in plane

The probability density function $P_n(\mathbf{r})$ approximated by Eq.(4.1.1) is mainly a form of the classical Central Limit Theorem, which asserts that the sum of a large number of independent, identically distributed random variables with finite variances is well approximated by a random variable with a Gaussian or normal distribution.

For a two-dimensional isotropic walk, the so-called Pearson's walk in the plane, in which the j^{th} step has length α_j, the transition probabilities are

$$p_j(\mathbf{r}) = \frac{1}{2\pi|\mathbf{r}|}\delta(|\mathbf{r}| - \alpha_j). \tag{4.2.1}$$

Let's consider the probability density function $P_n(\mathbf{r}) = \psi_n(|\mathbf{r}|)$ for the position of the walker and the probability $W_n(\mathbf{r})$ of being within a distance r of the starting position for an n-step isotropic walk in the plane. Closed form expressions for $P_n(\mathbf{r}) = \psi_n(|\mathbf{r}|)$ and $W_n(\mathbf{r})$ are not available for general values of n. To date, ψ_n and W_n have been evaluated in terms of known functions only for n=1,2 and 3 corresponding to an 1-, 2- and 3-step isotropic walk in the plane respectively. This section is only limited in deriving expressions for the probability density function $P_n(\mathbf{r}) = \psi_n(|\mathbf{r}|)$ of Pearson's walk with constant step length α [Hughes, 1995].

The case of 1-step isotropic walk in plane is trivial with

$$\psi_1(r) = \frac{1}{2\pi r}\delta(r - \alpha). \tag{4.2.2}$$

The probability density function $P_1(\mathbf{r}) = \psi_1(|\mathbf{r}|)$ for an 1-step Pearson's walk is a Dirac delta function. Thus, $\psi_1(|\mathbf{r}|)$ has a non-zero value and equal to $\frac{1}{2\pi\alpha}$ only when $r = \alpha$.

For a 2-step isotropic walk in plane, with equal steps of length α

$$\psi_2(r) = \begin{cases} \frac{1}{\pi^2 r}[4\alpha^2 - r^2]^{-1/2}, & r < 2\alpha \\ 0, & r > 2\alpha \end{cases}. \tag{4.2.3}$$

The probability density function $P_2(\mathbf{r}) = \psi_2(|\mathbf{r}|)$ for a 2-step Pearson's walk with constant step length $\alpha = 1$ is illustrated in Fig. 4.2.

For a 3-step isotropic walk in plane, with equal steps of length α

$$\psi_3(r) = \begin{cases} \frac{kK(k)}{2\pi^3\alpha^2(r/\alpha)^{1/2}}, & 0 < r < \alpha \\ \frac{K(1/k)}{2\pi^3\alpha^2(r/\alpha)^{1/2}}, & \alpha < r < 3\alpha \\ 0, & r > 3\alpha \end{cases}, \tag{4.2.4}$$

where function K is a complete elliptic integral given by the formula

$$K(k) = \int_0^1 dt(1 - t^2)^{-1/2}(1 - k^2t^2)^{-1/2}, \tag{4.2.5}$$

and the quantity k is

$$k^2 = \frac{16\alpha^3 r}{(r + \alpha)^3(3\alpha - r)}. \tag{4.2.6}$$

The probability density function $P_3(\mathbf{r}) = \psi_3(|\mathbf{r}|)$ for a 3-step Pearson's walk with constant step length $\alpha = 1$ is illustrated in Fig. 4.3.

As the number of steps n increases, for a walk with constant step length α, probability density function becomes

$$P_n(\mathbf{r}) = \psi_n(r) \sim \frac{1}{\pi n\alpha^2} exp - \frac{r^2}{n\alpha^2}, \tag{4.2.7}$$

with $r = |\mathbf{r}|$.

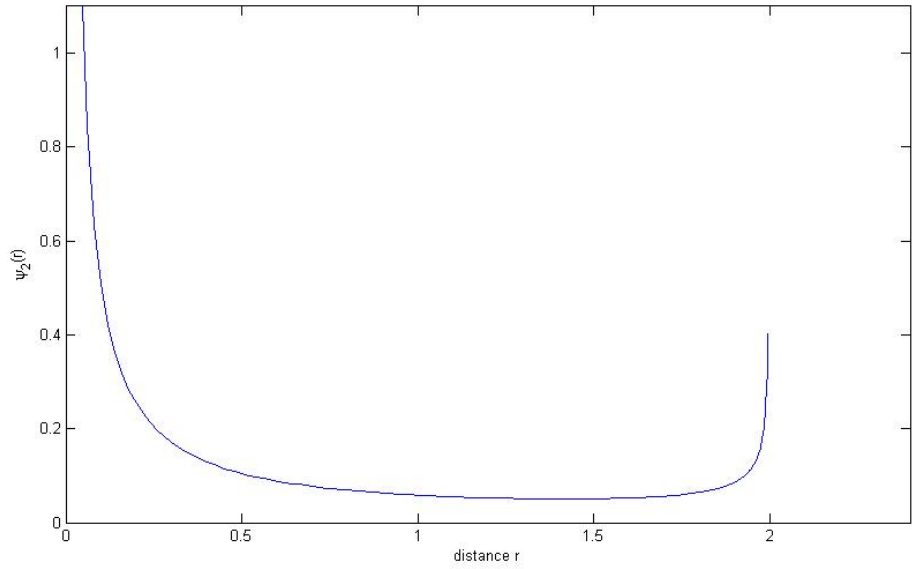

Figure 4.2: *The radially symmetric probability density function $P_2(\mathbf{r}) = \psi_2(|\mathbf{r}|)$ for a 2-step isotropic walk in the plane. Step α is constant and equal to 1. ψ_2 has two vertical asymptotes at $r = 0$ and $r = 2\alpha$.*

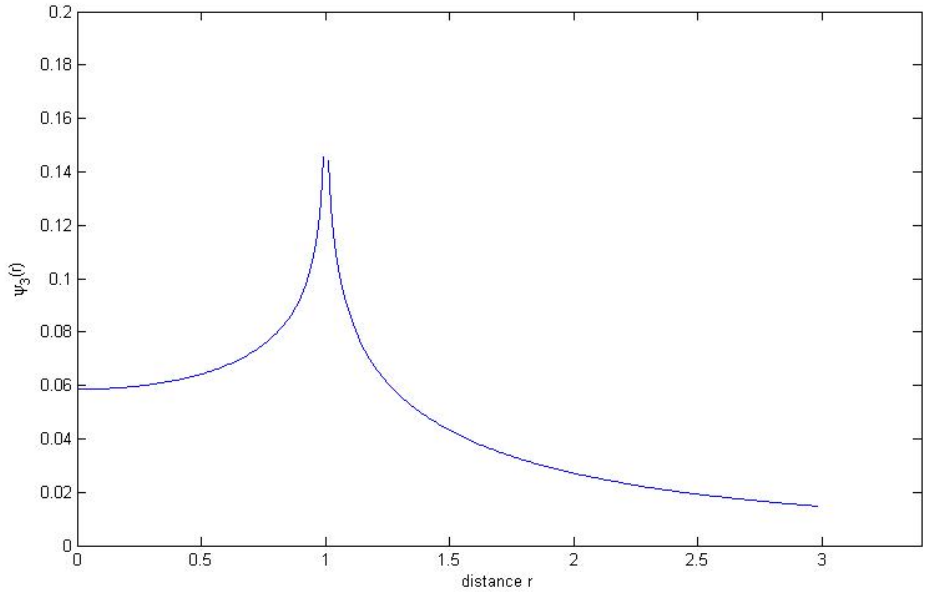

Figure 4.3: *The radially symmetric probability density function $P_3(\mathbf{r}) = \psi_3(|\mathbf{r}|)$ for a 3-step isotropic walk in the plane. Step α is constant equal to 1. ψ_3 has a vertical asymptote at $r = \alpha$.*

4.3 Pearson's walk in plane: A tool for quantifying clustering

From the section 4.2, it is evident that the probability density function of walker's position strongly depends on the number of steps that the walker has traveled. In section 4.1.2, the total backscattered electric field is related to the walker's position. Indeed, this analysis has been developed under the convention $|\mathbf{r}| = |\mathbf{E}_1^{sc}(\mathbf{x}_R)|$. However, Pearson also worked with the related function $\phi_n(|\mathbf{r}|^2) = \psi_n(|\mathbf{r}|)$ [Hughes, 1995], where it could be assumed that $|\mathbf{r}|^2 = |\mathbf{E}_k^{sc}(\mathbf{x}_R)|^2$. Therefore, since the backscattered power is approximated by the square magnitude of total backscattered electric field, the probability density function of the

backscattered power when droplets in the cloud volume form 1, 2 and 3 clusters is linked to the probability density function $P_n(\mathbf{r}) = \psi_n(|\mathbf{r}|)$ for n=1, 2, 3 respectively. These cases can be considered as 3 different degrees of spatial correlation among cloud droplets.

In the absence of clustering where all N droplets inside the cloud volume are completely independent (i.e., pair-correlation function is zero), the magnitude of each component of the total backscattered electric field follows a Gaussian (normal) distribution given by Eq. (4.2.7). Therefore, the magnitude of the total backscattered electric field follows a Rayleigh distribution [Beckmann and Spizzichino, 1987]. Then, the backscattered power is expected to be exponentially distributed. In the presence of clustering, patterns of backscattered electric field and the relevant power are approximated by the analytical formulas of n-step isotropic random walk in plane when n=1, 2, 3. Lower degrees of spatial correlation (i.e., droplets into 4 and more clusters) are expected to converge to the case of perfect randomness.

5 Research approach

5.1 Description of the computational model

Suppose that the radar, while looking at the sky, illuminates a cloud volume filled with N liquid water droplets, which are considered as perfect spheres. For the computational tests, the cloud volume is simulated as a box with dimensions $0.05m \times 0.05m \times 0.05m$ and the concentration of particles inside the box equals 500 particles/cm^3. The source/receiver, which represents the cloud radar, is located at a large distance of $10m$ so as the cloud volume is considered in the far field of the radar. The exact coordinates of the receiver for a cloud volume with the aforementioned dimensions are (0.025, 0.025, -10). In Fig. 5.1, the *radar-cloud volume* system of the computational model is illustrated.

The source operates at $3mm$ wavelength and, thus, electric permittivity of water at $3mm$ and 3^oC temperature is estimated as 6.4078 + i*8.43 [Liebe et al., 1991]. During the illumination time, which is 1s, the radar transmits pulses with a time interval of 1ms between successive pulses. Hence, every 1ms one snapshot of the cloud volume is collected. At each snapshot, the field scattered by every individual droplet is calculated by Eq. (2.30). By studying the successive snapshots taken during the total measurement time, one can extract information about the spatial structure of cloud. Since turbulence mixes the atmosphere, droplets cannot be static inside the cloud, but instead they distribute horizontally or/and vertically. Therefore, the spatial distribution of droplets changes from snapshot to snapshot due to the presence of eddies inside the cloud volume which make droplets move in many ways. The type of turbulence (together with relevant parameters such as wind velocity and wind direction) indicates the motion that particles undergo in the cloud. Four different types of motion are simulated from the developed model. The patterns of scattered electric field and relevant scattered power are investigated with respect of the various types of motion. Moreover, in order to investigate the clustering of droplets to be investigated, the resulting patterns of scattered field and power distributions are compared for different degrees of spatial correlation among droplets. The explicit description of the possible generated motions and how clustering may affect the scattered field and power will be elaborated in the next sections.

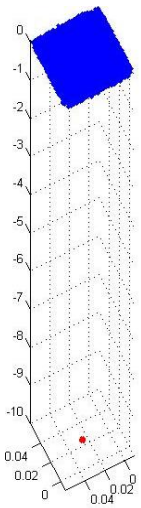

Figure 5.1: *Simulation of the radar-cloud volume system. The cloud volume is simulated by a box with dimensions 0.05m x 0.05m x 0.05m and the concentration of particles inside the box equals 500 particles/cm^3. The cloud volume is considered in the far field of the radar which is located in point (0.025, 0.025, -10). The cloud droplets are indicated by blue spheres while radar location is shown by a red cross.*

5.2 Investigated cases

Provided that randomness of droplets is a cloud feature characterized by the spatial distribution of particles, it is mandatory to classify the possible study cases related to particles' spatial correlation. Hence,

1. all N particles are completely uncorrelated. The particles do not compose any cluster and they can move independently in all three directions.

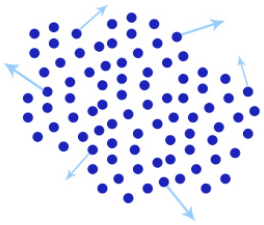

Figure 5.2: *All cloud droplets completely uncorrelated. This is the case where particles do not form any cluster. The absence of clustering implies that droplets are perfectly random distributed inside the cloud volume. In such a case, droplets can move independently in all three directions.*

2. all N particles inside the cloud volume are totally correlated. The cloud droplets form just one cluster which can be moved with four types of motion, which are all described in section 5.2.2.

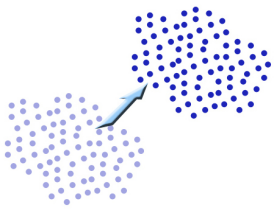

Figure 5.3: *All cloud droplets totally correlated. This is the case where particles form a single cluster. The cluster can undergo four types of motion.*

3. the particles are partially correlated. The N particles are arranged in 2 to (N-1) clusters and each cluster can move independently from any other cluster. Thus, in the simple case where N particles are distributed into two clusters of N/2 droplets, let's say cluster A and cluster B, particles belonging to cluster A are totally correlated with the particles of same cluster and completely uncorrelated with the particles of cluster B and vice versa. Similarly, in case N particles distributed into three clusters of N/3 droplets (illustrated in Fig. 5.4b, let's say cluster A, B and C, particles belonging to cluster A are totally correlated with the particles of same cluster and completely uncorrelated with the particles of clusters B and C. In particular, the cases where the total number of droplets N are distributed into 2 and 3 clusters are mostly elaborated in this study. Moreover, lower degrees of spatial correlation among droplets (i.e., when droplets form more than 3 clusters) will be investigated until the point of convergence to the case of completely uncorrelated droplets (Case 1).

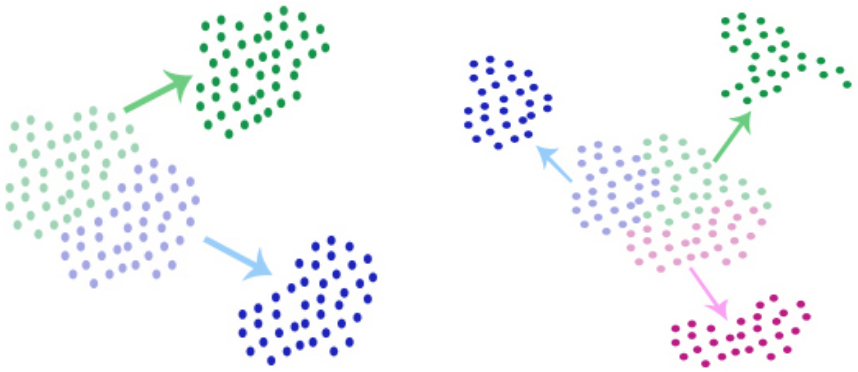

(a) *N droplets distributed into 2 clusters* **(b)** *N droplets distributed into 3 clusters*

Figure 5.4: *Cloud droplets partially correlated. N particles are arranged in 2 to (N-1) clusters and each cluster can move independently from any other cluster. In the simple case where N particles are distributed into two clusters of N/2 droplets (a), let's say cluster A and cluster B, particles belonging to cluster A are totally correlated with the particles of same cluster and completely uncorrelated with the particles of cluster B and vice versa. Similarly, in case N particles distributed into three clusters of N/3 droplets (b), let's say clusters A, B and C, particles belonging to cluster A are totally correlated with the particles of same cluster and completely uncorrelated with the particles of clusters B and C.*

5.2.1 No cluster: Independent movement of droplets

When the droplets are distributed in a perfectly random way inside the cloud volume, there is no chance of clustering among droplets. This is simulated by a cloud volume which consists of N droplets that can move independently to any direction in space. Therefore, the individual droplets are free to move to a random direction and with a random step. The displacement from one snapshot to the next one is related to the velocity and/or acceleration. Suppose that the current location of a droplet is $\mathbf{x}(t)$ at any given time t and the time difference between two successive snapshots is Δt. In the presence of a turbulent eddy which makes the droplets move with a velocity $\mathbf{v}(\mathbf{x},t) = \frac{d\mathbf{x}(t)}{dt}$ and an acceleration $\alpha(\mathbf{x},t) = \frac{d^2\mathbf{x}}{dt^2}$, the next location of each droplet after Δt is expressed by the following equation:

$$\mathbf{x}(t+\Delta t) = \mathbf{x}(t) + \frac{d\mathbf{x}}{dt}\Delta t + \frac{d^2\mathbf{x}}{2dt^2}\Delta t^2, \tag{5.2.1}$$

The computational experiments will be used as validation for the basic radar theory which assumes Poissonian clouds (i.e., with perfect randomness). Hence, the total scattered field measured at the receiver location is expected to follow a Gaussian distribution and the corresponding total backscattered power will be exponential distributed. This power is the so-called coherent power and it should be studied in comparison with the relevant incoherent power. In the classical radar theory, the incoherent power is expected to be equal to the mean value of the distribution of coherent power. The validity of this statement will be tested through simulations for the case of completely uncorrelated droplets.

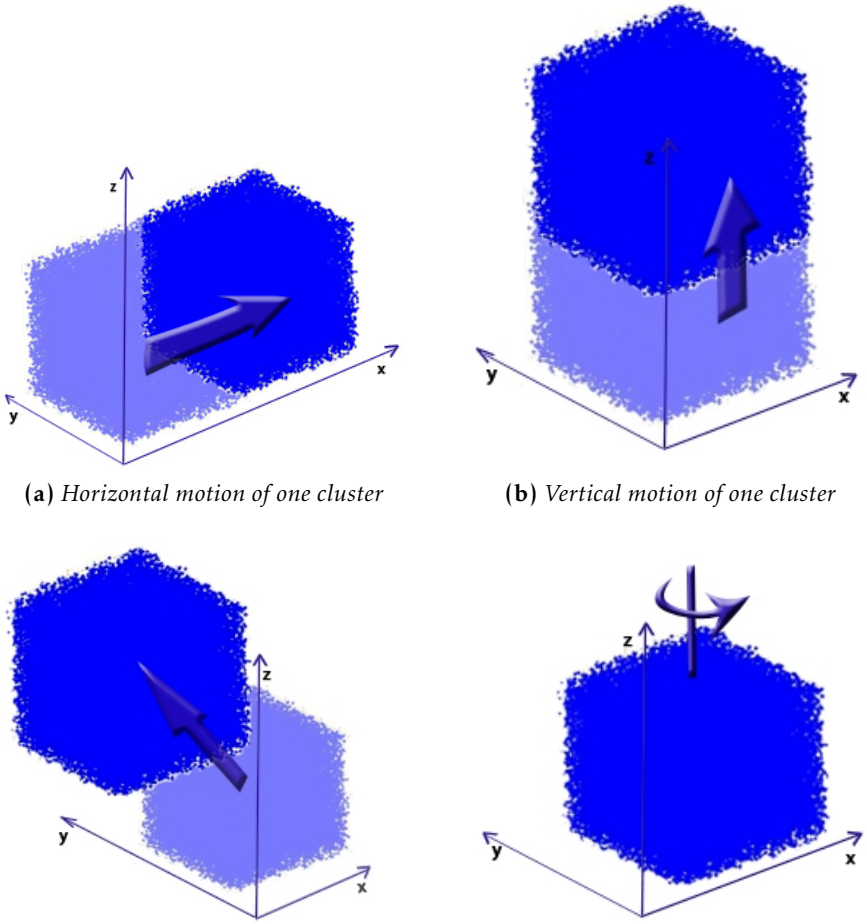

(a) *Horizontal motion of one cluster*

(b) *Vertical motion of one cluster*

(c) *Motion of one cluster in 3-dimensional space*

(d) *Rotation of a cluster about a vertical axis*

Figure 5.5: *Types of motion for one cluster. (a) Horizontal motion of one cluster. The direction of this motion is fixed parallel to x-axis while the displacement is random but bounded in the range* $(-v\Delta t - \frac{1}{2}\alpha\Delta t^2, +v\Delta t + \frac{1}{2}\alpha\Delta t^2)$*. (b) Vertical motion of one cluster. The direction of this motion is fixed parallel to z-axis while the displacement is random but bounded in the range* $(-v\Delta t - \frac{1}{2}\alpha\Delta t^2, +v\Delta t + \frac{1}{2}\alpha\Delta t^2)$*. (c) Motion of one cluster in 3 dimensional space. The cluster can move at any direction in space. The direction of this motion can either remain fixed and the displacement takes random non-negative values from the range* $(0, +2v\Delta t + \alpha\Delta t^2)$ *or changes between snapshots and the step takes random values from the range* $(-v\Delta t - \frac{1}{2}\alpha\Delta t^2, +v\Delta t + \frac{1}{2}\alpha\Delta t^2)$*. (d) Rotation of a cluster about a vertical axis. The cluster can rotate about an axis which is located in the center of the cluster parallel to the z-axis. The rotation axis has been defined perpendicular to x,y-plane and transverse to the center of the cluster at its initial position. Alternatively, the axis of rotation is selected so as to cross the center of cluster in x,y-plane at each realisation. The rotation step is indicated by the angle of rotation.*

5.2.2 One cluster: Possible motions of the cluster

The extreme case of totally correlated droplets is simulated as all droplets in the cloud volume forming just a single cluster. Therefore, the droplets are all moving with the same way (i.e., same direction, same velocity and acceleration). Suppose a 3-dimensional coordinate system (x, y, z). The generated motions that the cluster may undergo are

1. Horizontal motion: the cluster can only move parallel to x-axis. Thus, the direction of this motion is fixed while the displacement is random but bounded in a range which depends on the given velocity and acceleration. In detail, the upper and lower bounds of cluster's displacement are defined as $-(v\Delta t + \frac{1}{2}\alpha\Delta t^2)$ and $+(v\Delta t + \frac{1}{2}\alpha\Delta t^2)$ respectively. In practice, the maximum displacement matters for the computation tests, since various combinations of values for the velocity and acceleration result in

the same maximum displacement estimated by Eq. (5.2.1). The illustration of the horizontal motion is presented in Fig. 5.5a.

2. Vertical motion: the cluster can move only parallel to z-axis. The direction of this motion is fixed and the displacement can take any value again from the range $(-v\Delta t - \frac{1}{2}\alpha\Delta t^2, +v\Delta t + \frac{1}{2}\alpha\Delta t^2)$. For the computational tests, only different values for the maximum displacement are considered and not individual values for the velocity and acceleration. A representation of this motion is shown in Fig. 5.5b.

3. 3-dimensional motion: the cluster can move at any direction in space. The direction of this motion can either remain fixed or change between snapshots. In particular, for the simulation of a 3D-motion with fixed direction, the direction is defined at the first realisation. Two out of the three Cartesian coordinates, which define the position of cluster in the reference coordinate system, remain constant for all the 1000 realisations, since the direction stays unchanged, and only the third coordinate changes with respect to the maximum displacement that velocity and acceleration permit. The displacement takes random non-negative values from the range $(0, +2v\Delta t + \alpha\Delta t^2)$. When a random direction 3D motion is simulated, the direction changes for all the realisation and, thus, all Cartesian coordinates of cluster's position change between realisations. In this case, the displacement takes random values from the range $(-v\Delta t - \frac{1}{2}\alpha\Delta t^2, +v\Delta t + \frac{1}{2}\alpha\Delta t^2)$. For the computational tests, only different values for the maximum displacement are considered and not individual values for the velocity and acceleration. The motion is depicted in Fig. 5.5c.

4. Rotation: the cluster can rotate about an axis which is located in the center of the cluster parallel to the z-axis. Suppose the initial position of each n^{th} droplet inside the cloud volume is defined by the Cartesian coordinates $\{x_n^0, y_n^0, z_n^0\}$. After the completion of each i^{th} rotation, the Cartesian coordinates $\{x_n^i, y_n^i, z_n^i\}$ define the new position of the n^{th} droplet inside the cloud volume, for i=1,2,3...,1000. Since the rotation is around a vertical axis parallel to z-axis, it is obvious that z-coordinate stays unchanged and, thus, $z_n^i = z_n^0 \; \forall \; i$. The model provides two types of rotation; one with a fixed rotation axis transverse to the center of cluster and another one with leaving freedom to the axis to slightly move. The first rotation can be characterized as deterministic since the axis of rotation do not change between two successive snapshots, while the second rotation can be considered as random because the rotation axis changes from the $(i-1)^{th}$ snapshot to the i^{th} snapshot. Actually, the difference between the two motions has been indicated by the selection of the rotation axis. At the first case, the rotation axis has been defined perpendicular to x,y-plane and transverse to the center of the cluster at its initial position. Thus, to determine the rotation axis $\{x_c^0 = |max(x_n^0)| - |min(x_n^0)|, y_c^0 = |max(y_n^0)| - |min(y_n^0)|\}$, only the initial positions $\{x_n^0, y_n^0, z_n^0\}$ are required and, hence, $\{x_c^i = x_c^0, y_c^i = y_c^0\}$ $\forall$ i=1,2,...,1000. At the second case, the axis of the i^{th} rotation is selected so as to cross the center of cluster in x,y-plane at the $(i-1)^{th}$ realisation. Therefore, the rotation axis for the i^{th} rotation is estimated as $\{x_c^i = |max(x_n^{i-1})| - |min(x_n^{i-1})|, y_c = |max(y_n^{i-1})| - |min(y_n^{i-1})|\}$. How fast the cluster rotates is defined by the induced angular velocity which is, for simplicity, indicated by the angle of rotation, θ. For a counter clockwise rotation, the rotation matrix is mathematically expressed as

$$R = \begin{bmatrix} cos(\theta) & -sin(\theta) \\ sin(\theta) & cos(\theta) \end{bmatrix},$$

whilst for a clockwise rotation, the rotation matrix is

$$R = \begin{bmatrix} cos(\theta) & sin(\theta) \\ -sin(\theta) & cos(\theta) \end{bmatrix}.$$

Therefore, for an i^{th} θ-angle rotation about the central vertical axis, the matrix form can be written:

$$\begin{bmatrix} x_n^i \\ y_n^i \end{bmatrix} = R \cdot \left(\begin{bmatrix} x_n^{i-1} \\ y_n^{i-1} \end{bmatrix} - \begin{bmatrix} x_c^i \\ y_c^i \end{bmatrix} \right) + \begin{bmatrix} x_c^i \\ y_c^i \end{bmatrix},$$

The motion is shown in Fig. 5.5d.

5.2.2.1 Physical reason for the choice of these motions

The above motions have been selected to simulate the dynamics of a cluster because they refer to different scales of turbulence. The first three motions take place in the presence of a large-scale eddy. Indeed, the horizontal, vertical and 3D motion may occur when the cloud volume is small compared to the length-scale of the eddy, as it is shown in Fig. 5.6a. In practice, 3-dimensional motion describes the turbulence in large-scale eddy conditions and the horizontal and vertical motion are subcategories of the 3D motion. However, the discrimination among horizontal, vertical and 3-dimensional was important to describe the physical location of the cloud volume inside the eddy. The rotation corresponds to a small-scale eddy, which is of comparable length with the cloud volume. A small eddy is illustrated in Fig. 5.6b. Hence, rotation can only be used when a small eddy is simulated. Consequently, the simulated motions cover different length scales of eddies and particularly for the case of large eddy, the direction of motion (horizontal, vertical or any direction in space) is defined depending on the physical location of cloud volume in the eddy.

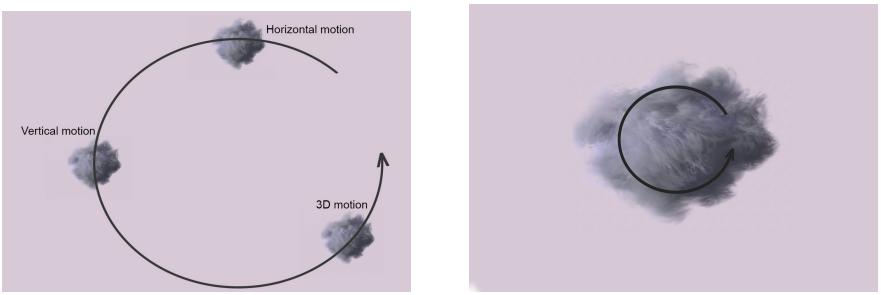

(a) *Large-scale eddy* **(b)** *Small-scale eddy*

Figure 5.6: *A large-scale and a small-scale eddy. In the presence of large-scale eddy (a), the cluster can undergo horizontal, vertical or 3D-motion. Depending on the physical location of cluster inside the eddy, the direction of motion is defined. In the presence of a small-scale eddy (b), the only possible motion that describes the dynamics of a cluster is the rotation.*

5.2.3 More clusters: Possible arrangements of clusters inside the cloud volume

From the extreme case of totally correlated particles, there are intermediate cases of lower correlation among particles positions. In the model, the correlation degree is pertinent to the number of clusters that the cloud droplets are distributed in. Hence, by increasing the number of clustering present in the cloud volume, lower degrees of spatial correlation are introduced to the model. Since correlation is referred to the spatial distribution of particles, apart from the total number of clusters, the clustering type is also linked to the way they are located in the given space. The model accepts four types of arrangement for the droplets positions. For reasons of simplicity, all types of arrangement will be described for the case of two clusters present in the box of dimensions $0.05m \times 0.05m \times 0.05m$. With the given concentration of $500 particles/cm^3$, it is expected that the cloud volume contain 62500 droplets in total. Therefore, these particles can be split into two clusters of 31250 each. By convention, the number of droplets present in a cluster is estimated as the ratio of the total number of particles in the box over the number of clusters.

In order to give an indication of the different arrangements of droplets' clustering, the simple case of two clusters is illustrated below. Thus, possible arrangements are:

1. random arrangement: correlated particles (i.e. belonging to the same cluster) are not necessarily adjacent. In this case, the only requirement for the clustering process is that each cluster contains N/2 particles independently to particles' physical location inside the cloud volume. This clustering type is shown in Fig. 5.7a.

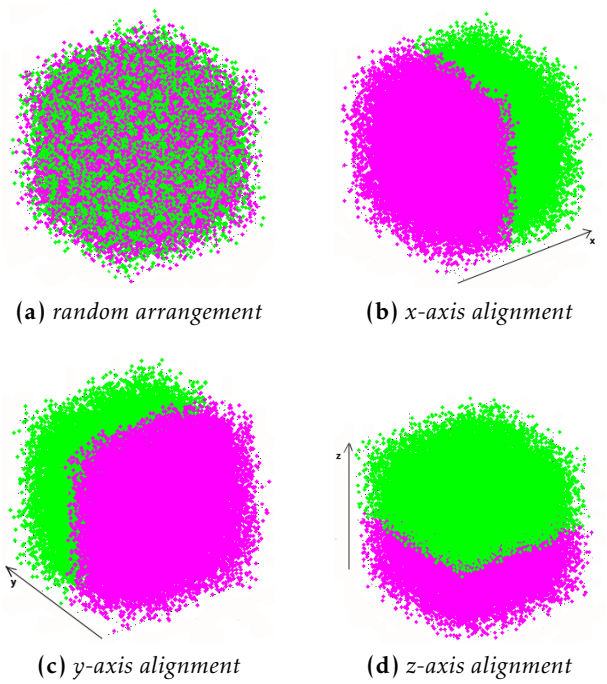

(a) *random arrangement* **(b)** *x-axis alignment*

(c) *y-axis alignment* **(d)** *z-axis alignment*

Figure 5.7: *Two clusters: types of clustering. (a) Random arrangement: correlated particles (i.e. belonging to the same cluster) are not necessarily adjacent. (b) X-axis alignment: the total cloud volume is separated into two clusters with a boundary plane transverse to the middle point of box's x-dimension. (c) Y-axis alignment: the total cloud volume is separated into two clusters with a boundary plane transverse to the middle point of box's y-dimension. (d) Z-axis alignment: the total cloud volume is separated into two clusters with a boundary plane transverse to the middle point of box's z-dimension.*

2. x-axis alignment: adjacent particles form clusters as illustrated in Fig. 5.7b. The total cloud volume has been broken into two clusters so as the boundary plane is transverse to the middle point of box's x-dimension.

3. y-axis alignment: adjacent particles form clusters as illustrated in Fig. 5.7c. The total cloud volume has been broken into two clusters so as the boundary plane is transverse to the middle point of box's y-dimension.

4. z-axis alignment: adjacent particles form clusters as illustrated in Fig. 5.7d. The total cloud volume has been broken into two clusters so as the boundary plane is transverse to the middle point of box's z-dimension.

The aforementioned arrangements have been tried to investigate whether the relative distance between each cluster and the receiver has an impact on the measured radar backscattered electric field and the relevant power. Several simulations have been performed to explore if such a classification for clustering types is necessary or has no influence on the total measured radar reflectivity. The latter implies that no different spatial arrangement for the same degree of clustering is required.

The possible types of motion for the case of two clusters is similar to the one cluster case. The main two possibilities are that all clusters undergo same type of motion or each cluster moves in a different way. The former case has been considered the most crucial to be studied since, in the latter case, the clustering effect on backscattered power is difficult to be interpreted. The major objective is to keep the introduced turbulence complexity at such a level so that the results can be easily comparable with random walks theory. Therefore, complex combinations of different types of motions are not considered in this research.

5.3 Description of the simulations

The computer simulations executed in Matlab software consist of an alternative way of experimenting. Most of the configuration parameters are mentioned in the next chapters where the computational results are presented. The drop radius in the tests has been considered constant and equal to $6\mu m$.

The primarily simulations aim to explore the patterns of electric field for the case of totally correlated particles. The patterns will be used to explore the effect of turbulence on the total scattered field. At every snapshot, one measurement for the total electric field has been obtained. Each component of the scattered

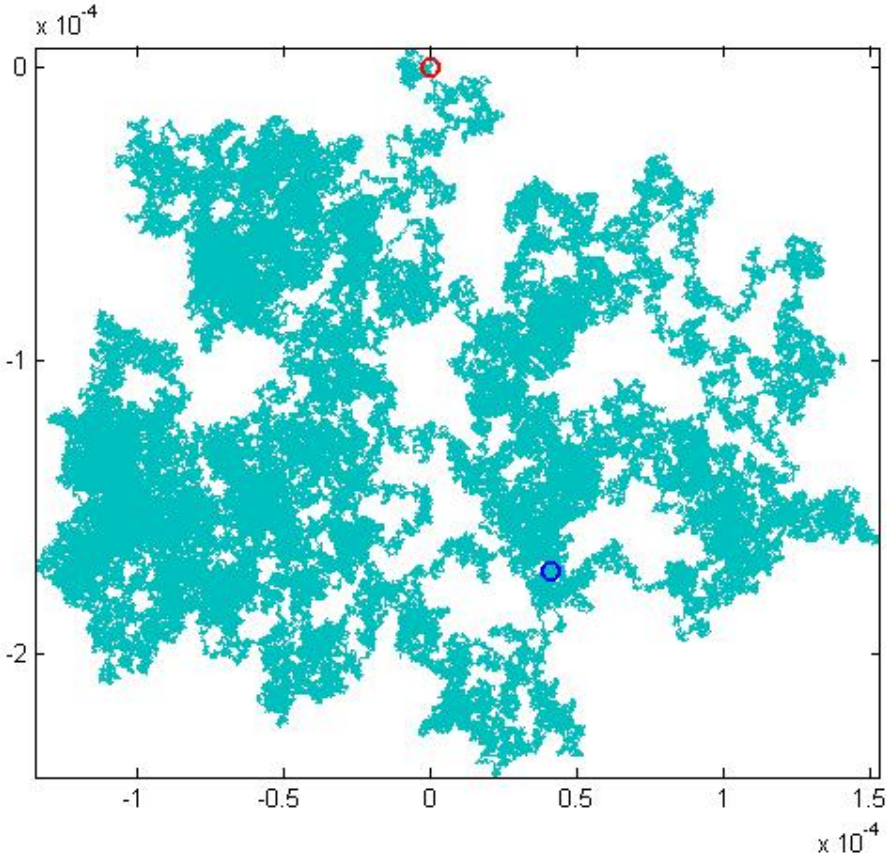

Figure 5.8: *A single realisation is a random walk in the complex plane. Each vector represents the first component of the scattered electric field by a single droplet. The total number of complex vectors is equal to number of droplets present in the cloud volume. The field scattered by the* 1^{th} *and the* 62500^{th} *droplet is represented by the red and blue circle respectively. The blue point, as being the end point of the random walk, expresses the first component of the total scattered electric field resulting by the coherent summation of 62500 scattered electric fields, measured at the receiver location. This figure shows one realisation of the motion of a single cluster in 3D space with a maximum displacement of* $500\mu m$.

electric field is depicted in the complex plane as a random walk. Fig. 5.8 illustrates a single realisation which is indeed a random walk in the complex plane. Each vector represents the first component of the scattered electric field by a single droplet. The complex vectors shown in the figure are equal to number of droplets present in the cloud volume. Thus, for the specified volume dimensions, 62500 vectors are coherently summed. In Fig. 5.8, the field scattered by the 1^{th} and the 62500^{th} droplet is represented by the red and blue circle respectively. Hence, the blue point, as being the end point of the random walk, expresses the first component of the total scattered electric field resulting by the coherent summation of 62500 scattered electric fields, measured at the receiver location.The patterns for the electric field have been studied through the distribution of these end points (i.e., the end point of each random walk denotes the first component of the total measured scattered field when contributions from all droplets have been

coherently summed). Hence, in the presentation of the results, figures in the complex plane depict the end points for the total number of realisations (i.e., 1000 realisations for 1sec measurement time).

Firstly, the case of completely correlated droplets has been investigated. The patterns of total electric field are explored for the specified types of motion described in section 5.2.2. Sensitivity analysis for the input parameters (i.e., velocity and acceleration) has been conducted for each type of movement, so as to answer the question: *How fast the cluster may shift in the total measurement time (i.e., 1sec) and what is the impact of these parameters (velocity and acceleration) on the resulting pattern of electric field?* For the horizontal, vertical and 3-dimensional motion, this is investigated through the maximum displacement that the cluster can run between snapshots. In particular, the patterns of electric field for these 3 motions have been studied for different maximum displacements. Regarding the rotation, how fast the cluster rotates is indicated by the angle of rotation completed between two snapshots. The patterns of electric field for all the aforementioned types of motion are presented in Chapter 6.

Furthermore, other degrees of spatial correlation, which have been studied in this thesis, are discussed in Chapter 7. The impact of clustering on the backscattered power distribution is presented in conjunction with the theory of random walks. The results are focused on answering the question: *Whether or not, in the presence of clustering, backscattered power resulting from the coherent summation of electric fields deviates from the expected incoherent power?* The cases of droplets distributed into 1, 2 and 3 clusters are analysed. Moreover, the convergence to the case of perfect randomness is explored when the number of clusters present in the cloud volume is increased.

6 Computational Results: The scattered electric field by one cluster

For the case of totally correlated droplets, which form a single cluster, they all undergo same type of motion. Nevertheless, the way motion has been categorized in 4 different types implies that each type of motion should be studied separately. For this reason, the results are grouped for particles which move horizontally, vertically, in any direction of 3-Dimensional space and particles who rotate around an axis. At the end, each type of motion will be recognizable from the pattern of total scattered electric field for a large number of realisations.

A comparative analysis of the total electric field for different types of motion When the total scattered field has been estimated as the coherent summation of the individual scattered fields, it is useful to show the patterns for the total scattered field. In the following figures, the first component of total scattered electric field for the total number of realisations is illustrated. The patterns for the second and third component of the total scattered electric field are similar to the pattern of the first component of total scattered electric field (see Appendix II). Nevertheless, the magnitude of the second and third component of backscattered electric field is much lower than the magnitude of the first component of backscattered electric field. Each point in the complex plane represents the total backscatter electric field measured at one realisation. The goal of the simulations was to identify the effect of different types of motion on the measured scattered field and recognise how the relevant parameters of each motion (i.e., velocity and acceleration) influence the pattern of electric field after few realisations. The number of realisations indicates the temporal scale, which has been kept fixed at 1000 realizations, since this gives a realistic number of samples in 1 sec measurement time.

For the following results, the initial conditions are not considered constant in the computational tests, but the initial positions of droplets inside the cloud volume are randomly generated in each test. However, for the same type of motion and same input parameters (i.e., maximum displacement), different initial conditions will result into similar patterns but they will only change the scaling of the pattern (see Appendix II).

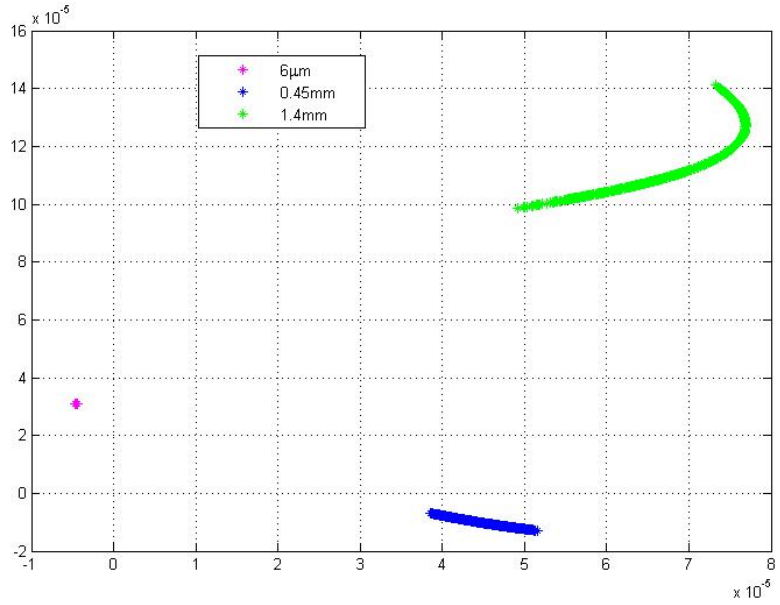

Figure 6.1: *One cluster undergoes horizontal motion. The cluster shifts to the left or to the right within a specified maximum displacement. The influence of maximum displacement on the total measured backscattered electric field is shown here. The total measured electric field for 1000 snapshots seems unchanged for a maximum displacement of* $6\mu m$*. For larger displacements, the electric field fluctuates more. For a maximum displacement of* $0.45mm$*, the scattered electric fields in the complex plane form a line while for an even larger maximum displacement of* $1.4mm$ *the total scattered electric fields form an arc.*

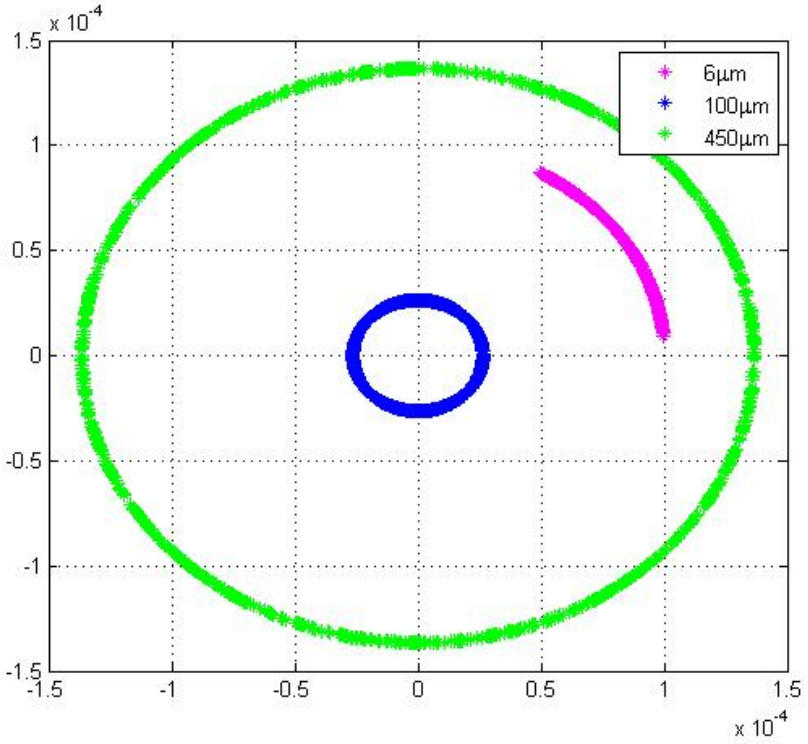

Figure 6.2: *One cluster undergoes vertical motion. The cluster can shift upwards or downwards within a specified maximum displacement. The influence of maximum displacement on the total measured backscattered electric field is shown here. The total measured electric fields for 1000 snapshots form an arc for a maximum displacement of* $6\mu m$*. For larger maximum displacements of* $100\mu m$ *and* $450\mu m$*, the scattered fields in the complex plane form rings about the origin.*

6.1 Horizontal motion

It was observed that the horizontal motion has the least influence on variation of the backscattered electric field. This is obvious from Fig. 6.1 since the scattered electric field measured at the receiver does not fluctuate for small displacements in the horizontal direction. In particular, the scattered electric field for 1000 snapshots seems unchanged when the cluster is free to move horizontally to the left or to the right within a maximum displacement of $6\mu m$, which corresponds to half drop diameter. For larger displacements, the measured field fluctuates more. Thus, the electric field in the complex plane is represented by lines for $0.45mm$ maximum displacement or arcs for higher velocities which result in cluster's maximum shift of $1.4mm$.

6.2 Vertical motion

On the other hand, when cluster moves exclusively in the vertical direction, the measured electric field is illustrated by arcs when the maximum displacement is small, like half drop diameter (i.e., $6\mu m$). However, for higher induced velocities (and/or accelerations), cluster is allowed to shift upwards and downwards within larger displacements. Larger vertical shifts, such as $100\mu m \sim 9$ drop diameter and $450\mu m \sim 38$ drop diameter, result in different patterns for the scattered electric field which are illustrated in Fig. 6.2 as rings around the origin (0,0). It is obvious that the magnitude of the scattered electric field remains constant and, hence, the corresponding backscattered power is expected to be constant for all realisations.

6.3 3-Dimensional motion

When particles, as a cluster, are free to move in any random direction in space, the pattern of backscattered electric field changes with respect to the maximal displacement. However, when the four types of motions were introduced in section 5.2.2, the 3-dimensional motion has been characterized twofold. The first option considers that cluster can move to any direction, which may change between two successive realisations, and with any random step within a given range. However, the second option does not allow the cluster to move to any different direction but only to a predefined direction and with a non-negative step. Fig. 6.3 illustrates the electric field pattern for the first option while the pattern for the second possible 3-dimensional motion is shown in Fig. 6.4.

Table 6.1: *Comparative table for the pattern of scattered electric field when one cluster moves horizontally, vertically and randomly in space. The impact of step length on the resulting pattern is presented.*

	Maximum displacement [μm]	Pattern of electric field in the complex plane	Mean value of magnitude [Vm^{-1}]	Standard deviation of magnitude [Vm^{-1}]
Horizontal motion	6	*dot*	3.1227e-05	2.3787e-08
	450	*line*	4.6103e-05	3.5009e-06
	1450	*arc*	1.3864e-04	1.3256e-05
Vertical motion	6	*arc*	1.0012e-04	1.1201e-09
	100	*ring*	2.6428e-05	2.9715e-09
	450	*ring*	1.3647e-04	1.0552e-07
3-Dimensional motion	6	*arc*	1.1837e-04	5.1392e-09
	100	*ring*	1.2844e-04	4.7181e-07
	450	*wider ring*	1.4245e-04	5.2762e-06

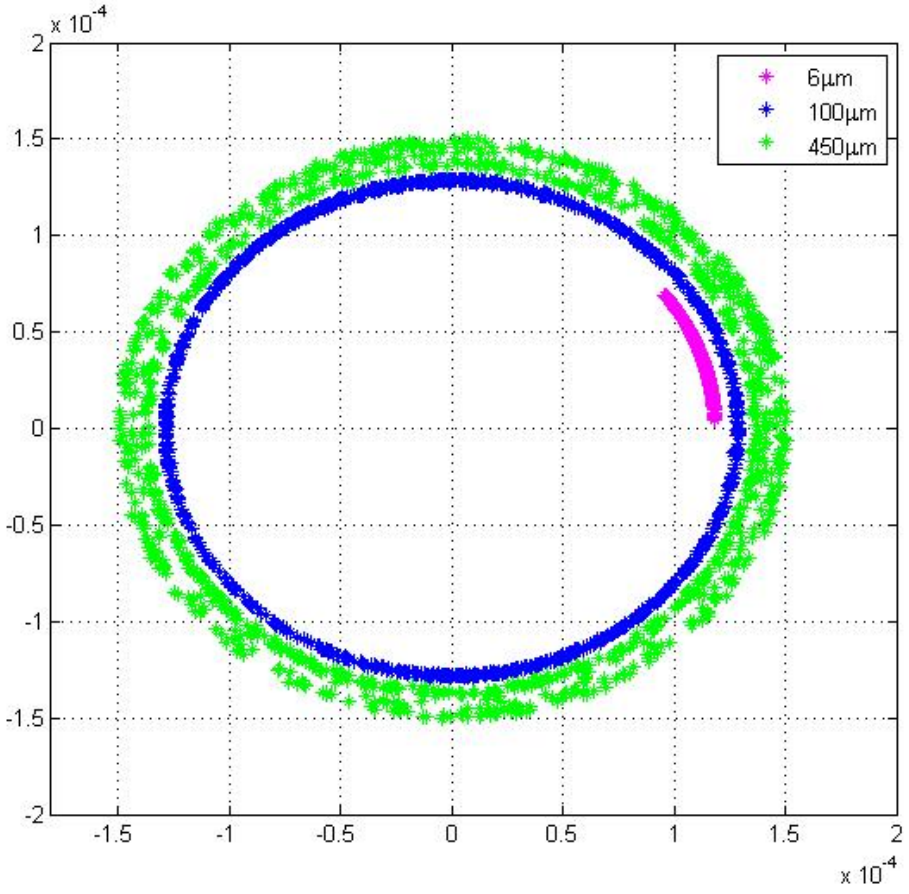

Figure 6.3: *One cluster undergoes 3-dimensional motion. The cluster moves to any arbitrary direction in space within a specified maximum displacement. For* 450μm *displacement, backscattered electric fields form an arc. When the maximum displacement increases to* 100μm*, points of backscattered electric field lie on a ring which becomes wider when velocity increases more and permits to the cluster to shift with a maximum displacement of* 450μm*.*

Table 6.2: *Comparative table for the pattern of scattered electric field when one cluster moves at any random direction in space or towards a given direction in space. The impact of step length on the resulting pattern is presented.*

	Displacement range [μm]	Pattern of electric field in the complex plane	Mean value of magnitude [Vm^{-1}]	Standard deviation of magnitude [Vm^{-1}]
3-dimension motion (random direction)	(-6,6)	*arc*	1.1837e-04	5.1392e-09
	(-100,100)	*ring*	1.2844e-04	4.7181e-07
	(-450,450)	*wider ring*	1.4245e-04	5.2762e-06
3-dimension motion (fixed direction)	(0,6)	*ring*	1.3816e-04	9.5665e-07
	(0,100)	*wider ring*	8.9197e-05	1.9947e-06
	(0,450)	*much wider ring (high concentration in the outer edge)*	9.0920e-05	1.5900e-05

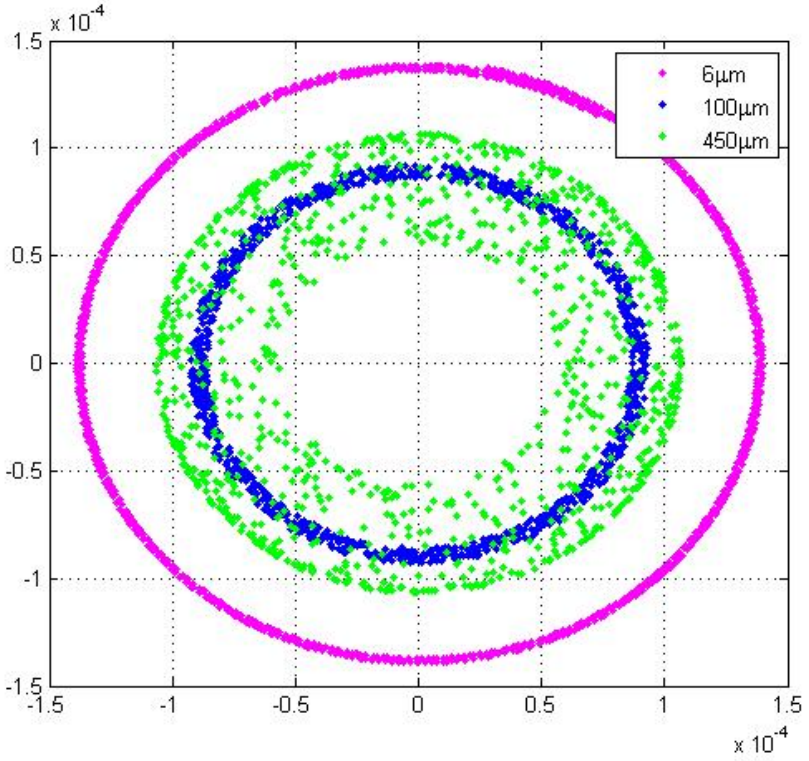

Figure 6.4: *One cluster undergoes 3-dimensional motion but towards a fixed direction. The cluster shifts towards a given direction in space within a specified maximum displacement. The total scattered electric fields for 1000 snapshots form a thin ring when the positive displacement of the cluster is any value from the range* $(0-6)\mu m$*. The ring becomes wider when the range increases to* $(0-100)\mu m$ *and when the maximum displacement increases to* $450\mu m$*, the ring becomes even wider but most of the points lie in the outer edge of the ring which means that the direction of motion leads the cluster to move closer to the radar.*

In Fig. 6.3, the impact of velocity on the measured backscatter is presented when cluster is free to move towards any direction in space. For particles moving with a small velocity which causes at most half a drop diameter displacement, radar returns form a sequence of points which is shown as the pink arc in Fig. 6.3. When the velocity of particles' motion increases at such an extent that may cause 9 drop diameters displacement between two successive snapshots, points of backscattered electric field lie on a ring (i.e. shown with blue color) which becomes wider when velocity increases more and permits to the cluster to shift even 38 drop diameters far from its current position (i.e. shown with green color).

Table 6.1 provides an overview of the three discussed motions. The patterns of scattered electric field are characteristic for each motion. Thus, by looking at these patterns, one can have an indication of the type of motion that the cluster undergoes and what is the maximum displacement that cluster moves between realisations. This can be useful for identifying the different scales of eddies present in a cloud volume. The order of standard deviation of electric field magnitude in conjunction with the order of mean magnitude are the two statistical properties which can describe the patterns. For instance, in the case of horizontal motion, a small displacement of $6\mu m$ is easily distinguished from a much higher displacement of $1450\mu m$ because a low mean magnitude in the order of $10^{-5}-10^{-4}$ with a very low standard deviation in the order of 10^{-8} would definitely correspond to the small displacement while a standard deviation of the order 10^{-5} would imply larger steps.

Not only the maximum displacement of clusters' movement is recognisable through the statistical mean and standard deviation of electric field magnitude, but for specified velocity and acceleration, the direction, which the cluster moves towards, can be identified. For example, for an eddy which induces a small maximum displacement of $6\mu m$, the order of difference between the mean magnitude and the standard

deviation can give an impression of clusters' relative position inside the eddy. In other words, if the maximum displacement is known, the pattern of backscattered electric field can provide information about the position of the cluster inside the eddy since in section 5.2.2.1 any type of motion has been related to a specific position of cluster in a large eddy. Indeed, for a maximum displacement of $450\mu m$, when cluster moves vertically the order of difference between mean magnitude and standard deviation is 10 times lower than the corresponding order of difference when cluster moves randomly in space.

Table 6.3: *Comparative table for the pattern of scattered electric field and the relevant power when one cluster moves towards a given direction in space but with different maximum step length. Deviation from incoherent power is defined as mean incoherent power minus mean coherent.*

	$450\mu m$ max displacement	$900\mu m$ max displacement
Pattern of electric field in the complex plane	*wide ring (high concentration in the outer edge)*	*wide ring (high concentration in the inner edge)*
mean value of magnitude $[Vm^{-1}]$	9.0920e-05	7.8432e-05
standard deviation of magnitude $[Vm^{-1}]$	1.5900e-05	2.3157e-05
probability density function of power	ascending curve	descending curve
mean power $[V^2m^{-2}]$	8.5199e-09	1.0403e-08
deviation from incoherent power (1.55e-08)	6.9801e-09	5.0970e-09

A more deterministic motion which does not permit any shift of direction between snapshots results to different patterns for the scattered field. That is reasonable because, in this case, there is no possibility that the cluster visits one position for a second time since the step is always non-negative. However, when the direction of motion does not change between successive realisations and the step is equally probable to be towards the positive and the negative axes, it is likely that the cluster might reach its initial position or any other intermediate position which was visited in a previous realisation.

In Fig. 6.4, the total scattered electric fields for 1000 snapshots form a thin ring when the positive displacement of the cluster is any value from the range $(0,6)\mu m$. The ring becomes wider when the step range increases to $(0,100)\mu m$ and when the maximum displacement increases to $450\mu m$, the ring becomes even wider but most of the points lie in the outer edge of the ring. This is reasonable for such type of motion when the cluster keeps on going towards a certain direction. It means that, in terms of physical location, the cluster approaches the radar. However, since the direction is fixed but initially randomly chosen and not deterministic, information about the direction can be extracted through the pattern of electric field or the behavior of power probability density function. When the displacement range is $(0,900)\mu m$, the total scattered electric field points, shown in Fig. 6.5, lie in the inner edge of the ring and, thus, the ring seems less dense in the periphery. A direct comparison upon the scattered field patterns for these two maximum displacements $450\mu m$ and $900\mu m$ can be made through Fig. 6.6. The observed difference between their patterns indicates (1) the widest ring corresponds to the largest maximum step and (2) the different directions of motions: cluster moves closer to the radar in the computational test of $450\mu m$ maximum displacement; cluster moves away from the radar in the computational test of $900\mu m$ maximum displacement.

Table 6.2 provides a direct comparison between the two types of motion in 3 dimensions (the random and the deterministic version). For the same maximum displacement, whether the direction of motion is fixed or random is obvious through the shape of the pattern. For instance, when the velocity of the wind is known and results to a maximum displacement of $100\mu m$, for a difference between mean value ($\approx 1.2844e-04$) and standard deviation of magnitude ($\approx 4.7181e-07$) in the order of 10^3, the pattern formed in the complex plane is a thin ring and thus a conclusion about cluster moving towards any random direction in space can be drawn. On the contrary, mean value ($\approx 8.9197e-05$) and standard deviation of magnitude ($\approx 1.9947e-06$) result in a difference in the order of 10^1-10^2 and the ring appears much wider. Hence, one can identify that the cluster has moved towards a fixed direction in space in this case.

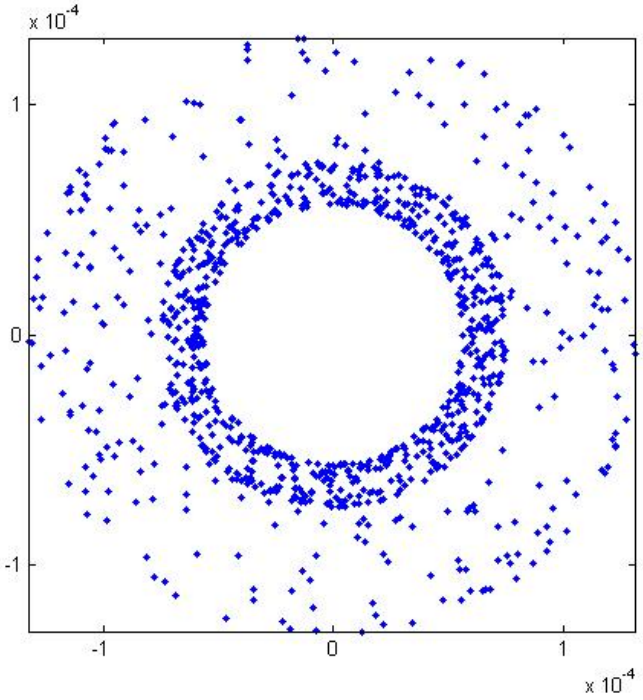

Figure 6.5: *One cluster undergoes 3-dimensional motion towards a fixed direction with a large maximum step of* 900μm. *Total scattered electric fields for large maximum displacement form still a ring but much wider. Most of the end points lie in the inner edge of the ring and, thus, the ring seems less dense in the periphery. This is interpreted as cluster moving away from the radar.*

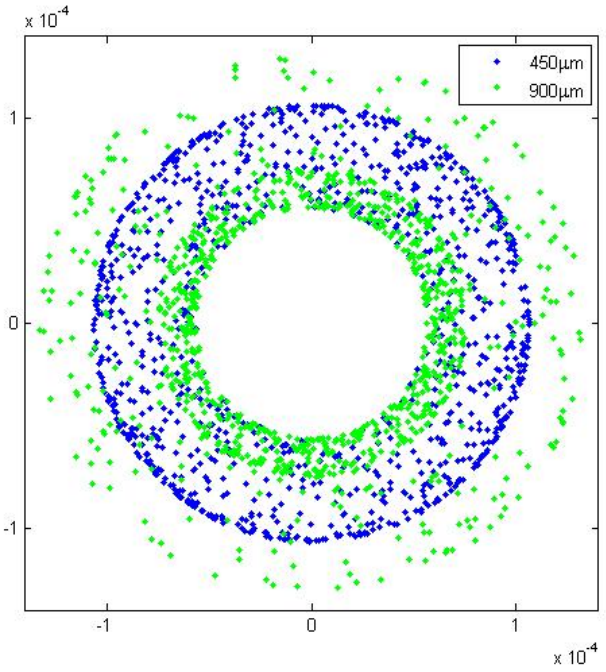

Figure 6.6: *One cluster undergoes 3-dimensional motion towards a fixed direction with large maximum steps. The green ring corresponding to the* 900μm *displacement is wider than blue ring which corresponds to the* 450μm *displacement. Moreover, the wider green ring is more dense in the inner edge area while the blue ring is more dense in the outer edge which means that in the green test cluster moves away from the radar whilst in the blue test cluster moves closer to the radar.*

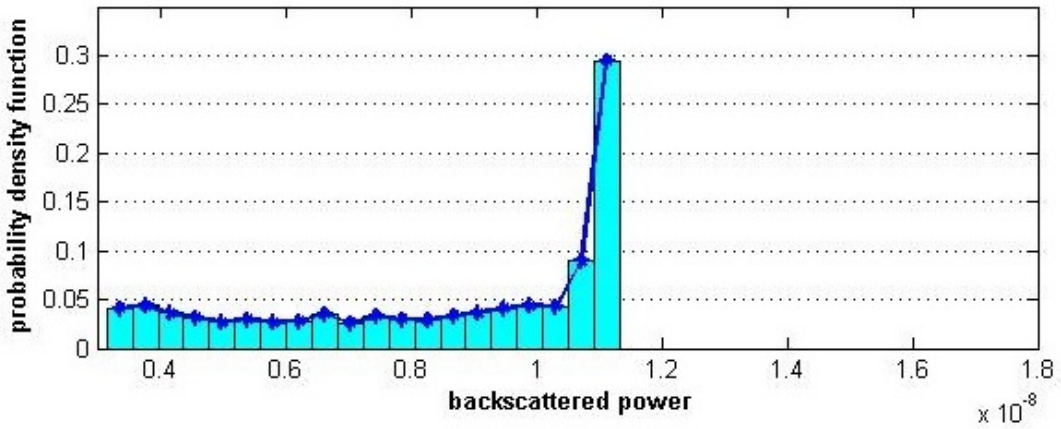

(a) 450μm *maximum displacement*

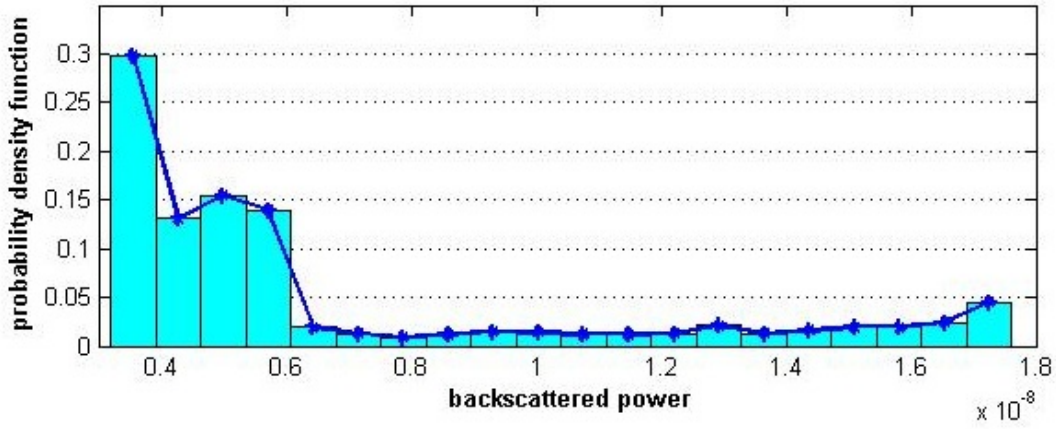

(b) 900μm *maximum displacement*

Figure 6.7: *Probability density function of total backscattered power for* 450μm *and* 900μm *maximum displacements. For a maximum displacement of* 450μm *the distribution of power is ascending because direction of motion is towards the radar while for a maximum displacement of* 900μm *the power distribution is descending because cluster moves away from radar. The range of backscattered power is shorter for the* 450μm *displacement than the* 900μm *displacement.*

The observed difference in the patterns of total scattered electric fields when the maximum displacement increases from 450μm to 900μm is meaningful for the expected distribution of backscattered power. Fig. 6.7 shows the probability density function (p.d.f.) of the total backscattered power for these different maximum displacements. Fig. 6.7a shows the p.d.f. of scattered power when the cluster can shift within a displacement of the range $(0, 450)\mu m$ and Fig. 6.7b shows the p.d.f. of the scattered power when the cluster can shift with any displacement from the range $(0, 900)\mu m$. The power in Fig. 6.7a is ascending while in Fig. 6.7b the power is descending. This is expected already from the patterns of electric field (see Fig.6.6) since for a 450μm maximum displacement, the ring is dense in the outer edge whereas, for a maximum displacement of 900μm, the ring is more dense in the inner edge area. The ascending trend of p.d.f. in Fig. 6.7a implies that the cluster approaches the radar whilst the descending trend of p.d.f. in Fig 6.7b implies that cluster moves away from radar. The range[1] of backscattered power is shorter for the 450μm displacement than the 900μm displacement. Indeed, from Fig. 6.6 this result was expected since the ring representing the 900μm displacement is wider than the one resulting from 450μm displacement. The ring

[1] Here, the term range denotes the spectrum of values, which is given as the difference between the maximum and minimum observed value.

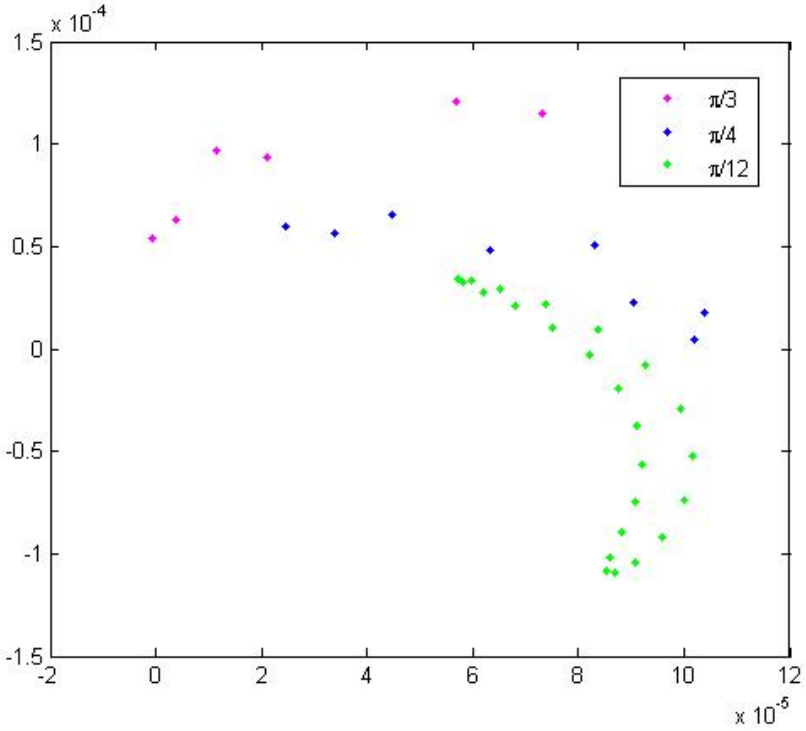

Figure 6.8: *One cluster undergoes deterministic rotation. The cluster rotates about its central axis with a known angular displacement. For a large angular displacement of $\pi/3$, the total scattered field is represented by 6 points in the complex plane. For $\pi/4$ and $\pi/12$, the total scattered field is represented by 8 and 24 points in the complex plane respectively.*

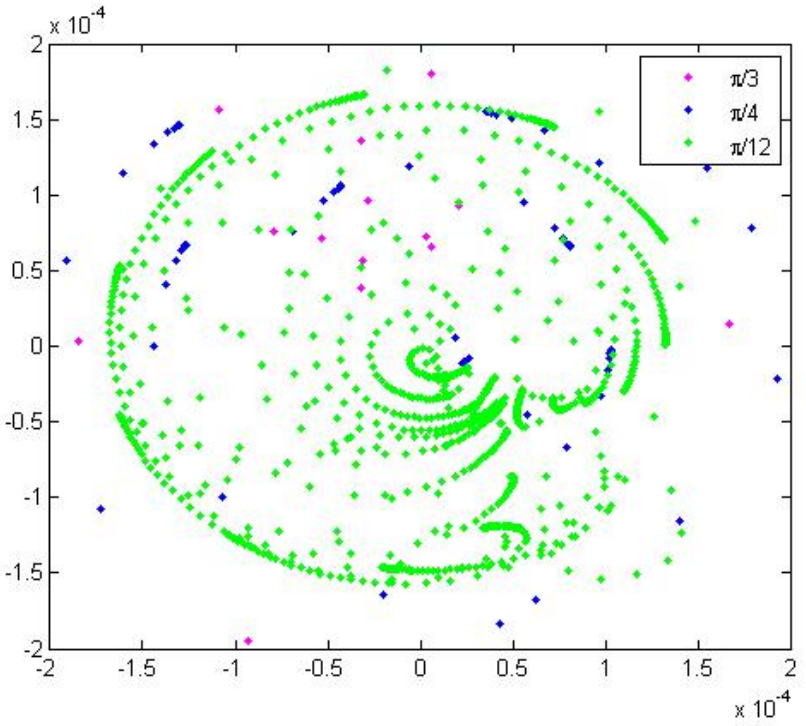

Figure 6.9: *One cluster undergoes a random rotation. The cluster rotates about an axis which is allowed to swift between snapshots with a known angular displacement. For a large angular displacement of $\pi/3$, the total scattered field is represented by few points in the complex plane. For smaller angles of $\pi/4$ and $\pi/12$, the total scattered field is represented by more points in the complex plane. In detail, for the $\pi/12$ angle, the rotation itself is evident by the scattered field pattern.*

gets wider while the maximum displacement increases.

Table 6.3 summarizes the differences in the scattered electric field and the corresponding backscattered power when one cluster moves towards a given direction in 3D space with different velocities. Through the statistical properties mentioned in the table, nothing with high certainty can be concluded about the maximum displacement of cluster, since mean magnitude and standard deviation have similar values for both displacements. However, the pattern of electric field can help in answering whether the cluster moves closer to the radar or not. The direction of motion is recognisable from the shape of the probability density function of backscattered power. As it was previously mentioned, when cluster moves closer to the radar, the p.d.f is an ascending curve whereas the power p.d.f. has a descending trend when cluster moves away.

6.4 Rotation

When the cluster makes a clear rotation around a fixed axis which is defined at the center of cluster's initial position, the pattern of scattered field is predictable because this type of rotation is of absolutely deterministic nature. Hence, if the cluster rotates about its central axis with a known angular velocity which leads to a specified angular displacement (i.e., the so-called rotation angle), the number of points in the complex plane is given as the ratio 2π/(angle of rotation). Indeed, for an induced angular velocity which results in a $\pi/4$ angular displacement between realisations, the cluster would have completed a total 2π rotation after 8 realisations. This deterministic rotation for three angular displacements is illustrated in Fig. 6.8. Indeed, from Fig. 6.8, the total backscattered electric fields after 1000 realisations for $\pi/3$, $\pi/4$ and $\pi/12$ angular displacements are represented by 6, 8 and 24 single points in the complex plane.

When the cluster rotates about a central axis (i.e., which always crosses cluster's middle point), the pattern of total scattered field is of a more random nature since the rotation axis changes between realisations. The end points forming the pattern of electric field are more in number than in the case of deterministic rotation. Indeed in Fig. 6.9, for angular displacements of $\pi/3$, $\pi/4$ and $\pi/12$, the scattered field consists of more than 6, 8 and 24 points respectively. The exact number of end points is not predictable though. A comparison of backscattered power between deterministic and random rotation when angular displacement is $\pi/12$ is given in Fig. 6.10. In Fig. 6.10a, the deterministic nature of this rotation type is shown through the periodic distribution of measured backscattered power (i.e., with a known period). In Fig. 6.10b, the power is still a periodic function since there is a hidden deterministic nature because the rotation axis always crosses the middle point of cluster. However, the periodicity of this function is not predictable for all the 1000 realisations in consistency with the non-predictable number of scattered points. For instance, in Fig. 6.11, the total backscattered power for 200 realisations is shown. There, it is presented that for the case of random rotation, the power is a descending periodic function for the first 200 realisations (0-200) (see Fig. 6.11b) while for the next 200 realisations (200-400) power would be an ascending periodic function (see Fig. 6.11c. For deterministic rotation, the power is neither decreasing nor increasing for the total number of 1000 realisations.

Furthermore, the computational tests showed that cluster's rotation is recognisable by the pattern of electric field when the rotation angle is sufficiently small. For instance, for an $\pi/3$ angular displacement, it is not possible to say that cluster undergoes a random rotation. However, when the angular displacement decreases to $\pi/12$, it is evident to identify the rotation just by the scattered electric field pattern.

The establishment of rotation can be useful for simulating small-scale eddies (see, Fig. 5.6b). The more realistic type of rotation is the less deterministic one. The exact trajectory of cluster's rotation can be seen through the backscattered points of electric field in the complex plane when the angular displacement is small. In Fig. 6.12, the total scattered field at the first and the last snapshot is indicated by the blue and pink circle respectively. All the intermediate realisations result in the rest intermediate points of the pattern. From the pattern of end points for small angular displacement, the stochastic nature of this type of rotation can be identified. In other words, the variations of the electric field which is scattered back to the radar implies that cluster does not only rotate about a central vertical axis but also shifts to one random direction in 3D space. However, the exact displacement of the cluster cannot be extracted.

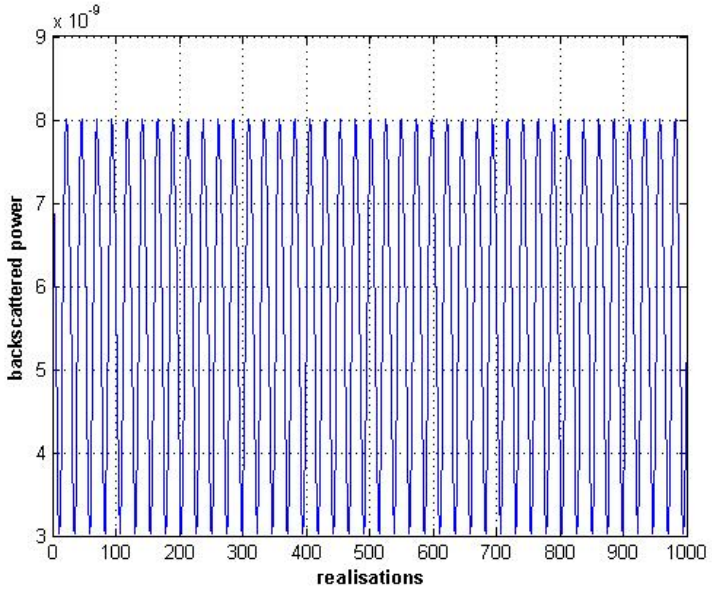

(a) *deterministic rotation*

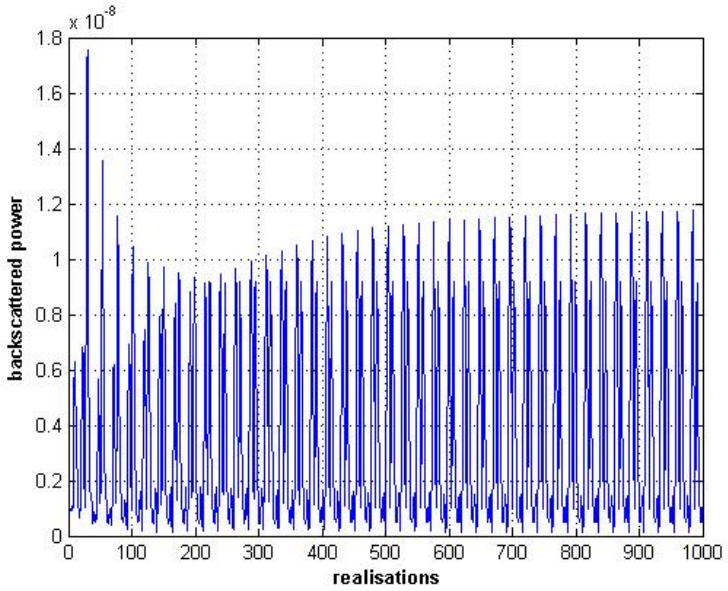

(b) *random rotation*

Figure 6.10: *Backscattered power in $\pi/12$ angle rotation. In Fig. 6.10a, the deterministic nature of this rotation can be seen through the periodic backscattered power versus the total number of realisations. In Fig. 6.10b, the power shows a hidden deterministic nature since the rotation axis always crosses the middle point of cluster. The deterministic nature of this rotation is evident through the backscattered power in Fig. 6.10b which is a periodic function. The main difference in these two power functions is that in the first case, only 24 values for backscattered power appear whereas, in the second case power may take more values but not predictable in number.*

The only conclusion that can be drawn is that the displacement is relatively small since it results to electric fields with comparable values of the ones resulting in the previous tests of random motion in 3 dimensions. For instance, the scale of the electric field in Fig. 6.12 is very much the same with the scale of the electric field in Fig. 6.3. It would be possible to combine a random 3D motion with the deterministic rotation, so as to have similar results with the stochastic rotation. Nevertheless, this is out of the scope of this thesis.

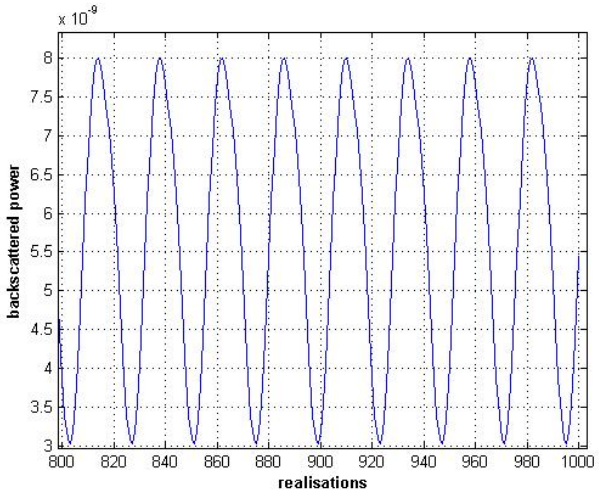

(a) *deterministic rotation 800-1000 realisations*

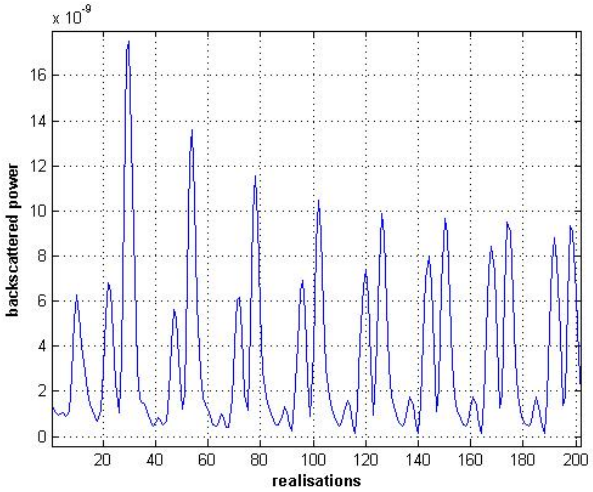

(b) *random rotation 0-200 realisations*

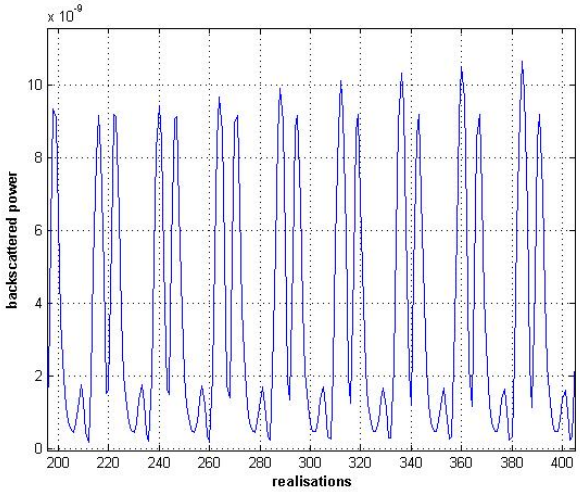

(c) *random rotation 200-400 realisations*

Figure 6.11: *Backscattered power in $\pi/12$ angle rotation for 200 realisations. This is a zooming-in of Fig. 6.10. For the deterministic rotation, any zooming-in for 200 realisations would result in (a). However, for the random rotation, zooming-in between 0-200 realisations (b) shows a descending trend, while a zooming-in between 200-400 realisations (c) shows an ascending trend.*

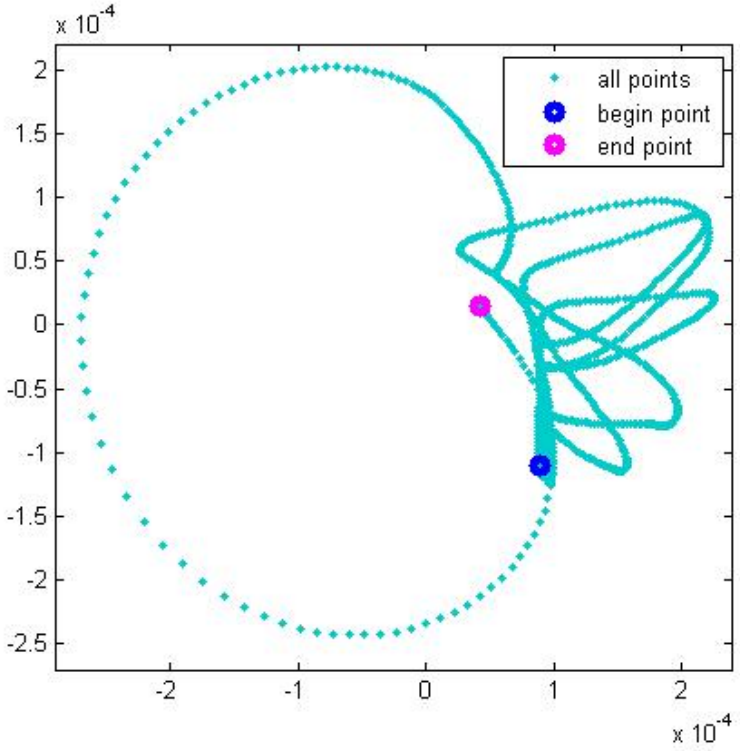

Figure 6.12: *One cluster undergoes random rotation with small angular displacement. The cluster rotates about a central mobile axis with an $\pi/100$ angular displacement. The scattered field pattern is characteristic for such a small angle and the exact trajectory of cluster's rotation can be seen through the backscattered electric field in the complex plane. The total scattered electric field at the first and the last snapshot is indicated by the blue and pink circle respectively. All the intermediate realisations result in the rest intermediate points of the pattern.*

7 Computational Results: Exploring different degrees of clustering

The order of discrepancy between the mean value of backscattered power and the one resulting from incoherent Rayleigh scattering theory will be analysed here. First, the absence of correlation is presented. The clustering effect is investigated by considering different numbers of clusters. The extreme case of having a single cluster present in the cloud volume is followed by the two and three clusters case. Finally, higher number of clusters are considered. The different degrees of clustering have been studied by considering same initial conditions for the computational tests. The influence of the initial conditions on the results is presented for the case of 2 clusters (see Appendix II).

7.1 Case I: All particles completely uncorrelated

According to the standard radar theory, droplets are completely uncorrelated inside the cloud volume. This property makes clouds to be considered as perfect random media. Perfect randomness results in

- **normal distribution** for the magnitude of each component of total backscattered electric field,
- **exponential distribution** for the backscattered power resulting as the coherent summation of individual scattered fields.

The computational tests aim to validate the aforementioned statements. The results of this case, where there is absence of clustering in the cloud volume, will be used for comparison with the different degrees of clustering. Thus, in a later section, the statistical properties of power distribution for partially correlated droplets (i.e., especially for droplets split into more than 3 clusters) will be compared to the 'no cluster' case.

For the case of all particles completely uncorrelated, where each droplet is free to move towards any direction in space within a maximum displacement of $150\mu m$, the pattern of first component of scattered electric fields in the phase space is illustrated in Fig. 7.1. Hence, the scattered points are Gaussian distributed around the origin. The p.d.f of their magnitude, shown in Fig. 7.2, is indeed a normal distribution. The distribution of scattered power resulting by the coherent summation of electric fields is shown in Fig. 7.3. There, it is shown that p.d.f. of backscattered power follows an exponential distribution. The mean value of this distribution is expected to be equal to the incoherent power, illustrated by the pink line in

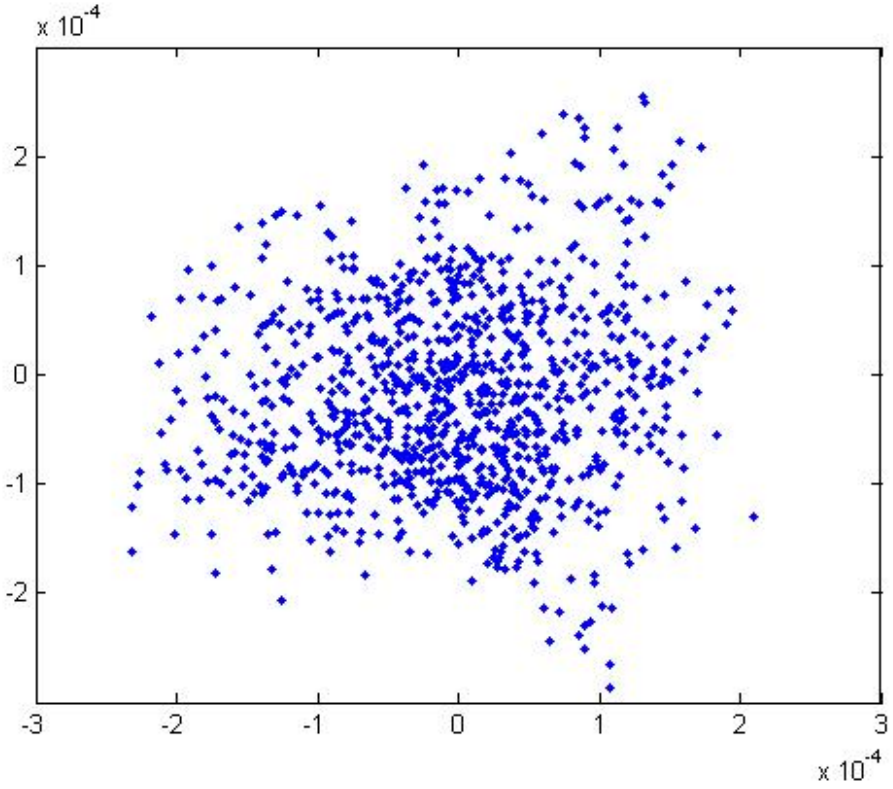

Figure 7.1: *Independent droplets move towards any random direction with a maximum displacement of 150μm. This is how the pattern of the first component of total scattered electric field looks like after 1000 realisations.*

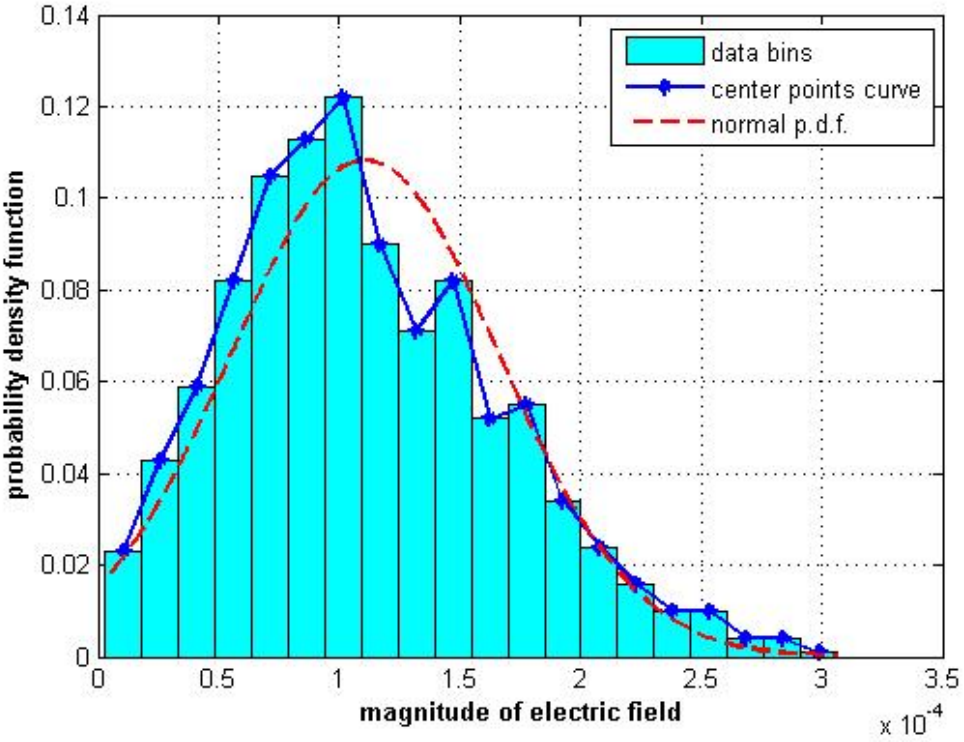

Figure 7.2: *P.d.f. for the magnitude of the first component of scattered field. The magnitude calculations refer to the scattered points of Fig. 7.1. Magnitude of the first component of scattered electric field follows a normal distribution.*

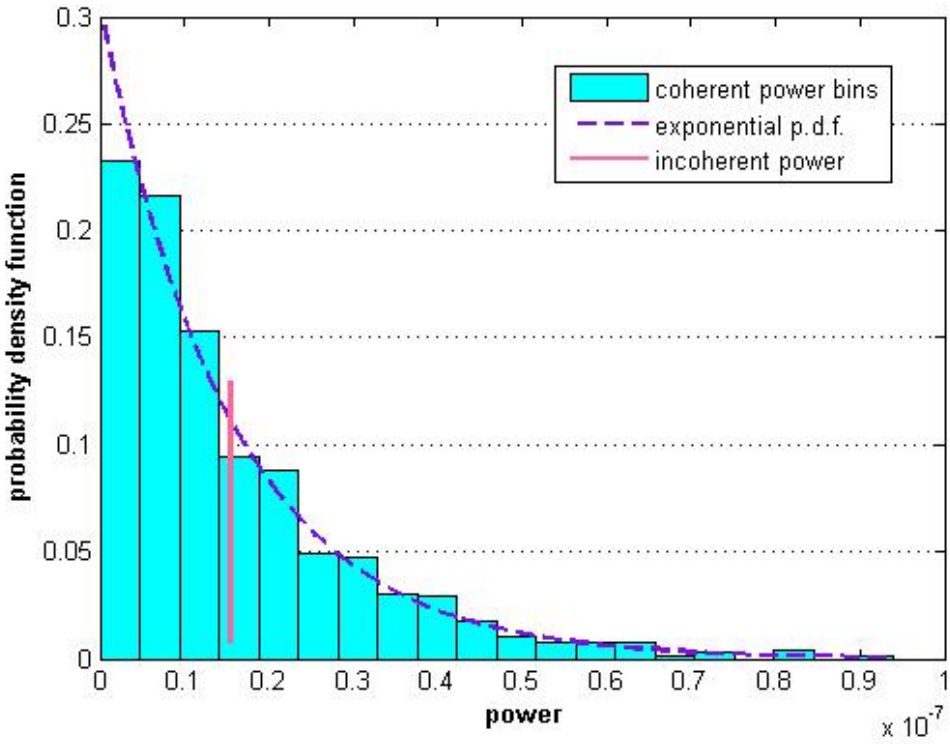

Figure 7.3: *P.d.f of the backscattered power Vs. the incoherent power. The power calculations refer to the scattered points of Fig. 7.1, when the cloud droplets are free to move towards any direction within a maximum displacement of 150μm. The coherent backscattered power is exponentially distributed. The mean value of the exponential distribution is almost equal to the incoherent power, illustrated by the pink line in the figure.*

Fig. 7.3. Indeed, for this computational experiment, the mean value of backscattered power is 1.5369e-08 while the mean incoherent power equals 1.55e-08 and, thus, the difference between them is in the order of 10^{-10} (in detail deviation between mean coherent power and mean incoherent power is 1.3294e-10). Such a low deviation is considered negligible for the sensitivity of radar to measure backscattered power.

7.2 Case II: All particles totally correlated

For the case of totally correlated droplets, which form one single cluster able to more towards any direction in space, the scattered electric field points after 1000 snapshots lie on rings which their width depends on cluster's maximum displacement (i.e., the maximum displacement parameter is estimated by the input velocity and acceleration). The backscattered field of totally correlated droplets was discussed in Chapter 6. The backscattered power by a single cluster, when this results from the coherent summation of individual electric fields, is presented here.

7.2.1 Consistency with single-step Pearson's two-dimensional walk.

For the purpose of this section, the cluster was freely moving towards any direction in space within a maximum specified displacement of $150\mu m$. The backscattered power measured at the receiver location does not fluctuate for a total number of 1000 realisations. The p.d.f. of backscattered power is a delta dirac function. Hence, there is consistency with the p.d.f. of distance from the origin in a single-step Pearson's two-dimensional walk $\psi_1(r)$. The single-step random walk was discussed in section 4.2. The non-fluctuating behavior of coherent power does not ensure that coherent and incoherent summation give equal values. For instance, in Fig. 7.4, the backscattered power, when coherent summation of the individual

electric fields is considered, is around the value of 0.32e-08V^2m^{-2} whilst power resulting from incoherent summation is 1.55e-08V^2m^{-2}. Therefore, the latter is five times higher than the backscattered power when electric fields are coherently summed. This discrepancy appears due to the spatial correlation among droplets.

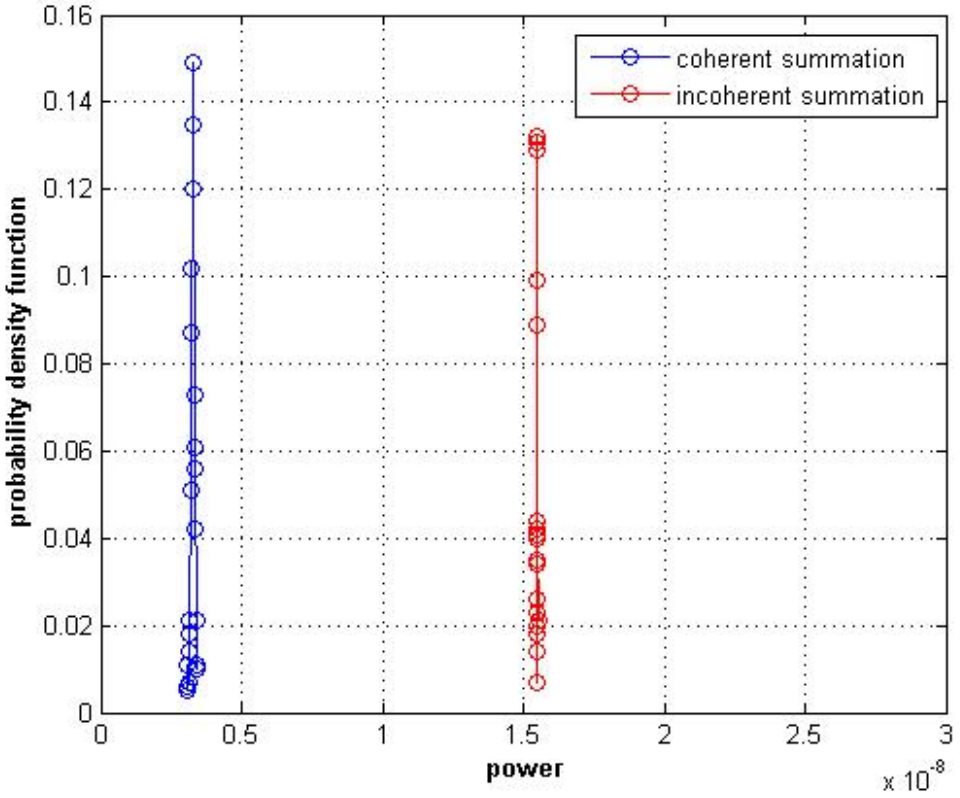

Figure 7.4: *Coherent Vs. Incoherent power. This test considers a cluster which moves to any direction in space with a maximum displacement of* 150μm. *The backscattered power is a delta dirac function, which simply means that it doesn't vary between snapshots. However, power from incoherent summation is five times higher than power measured from coherent summation.*

7.3 Case III: Particles of the cloud volume distributed into clusters

For the investigation of lower degrees of correlation among droplets' positions, droplets are split into larger number of clusters. The case of n=2 clusters and n=3 clusters is explicitly discussed in section 7.3.1 and 7.3.2 respectively. For an increased number of clusters, the backscattered power distribution is presented in section 7.3.3. For a large number of clusters, which implies low spatial correlation for cloud droplets, backscattered power, when electric fields are coherently summed, is an exponential distribution, which is very similar to the exponential distribution of power in the absence of clustering case (i.e., perfect randomness).

7.3.1 Particles distributed into two clusters

When particles are distributed into two clusters, four different arrangements (i.e., random arrangement, X-axis alignment, Y-axis alignment and Z-axis alignment) have been introduced in section 5.2.3. The pattern of each component of the total scattered electric field is similar for any type of arrangement. Such a pattern is illustrated in Fig. 7.5a. This is still a ring as in a single cluster case. However, the width of

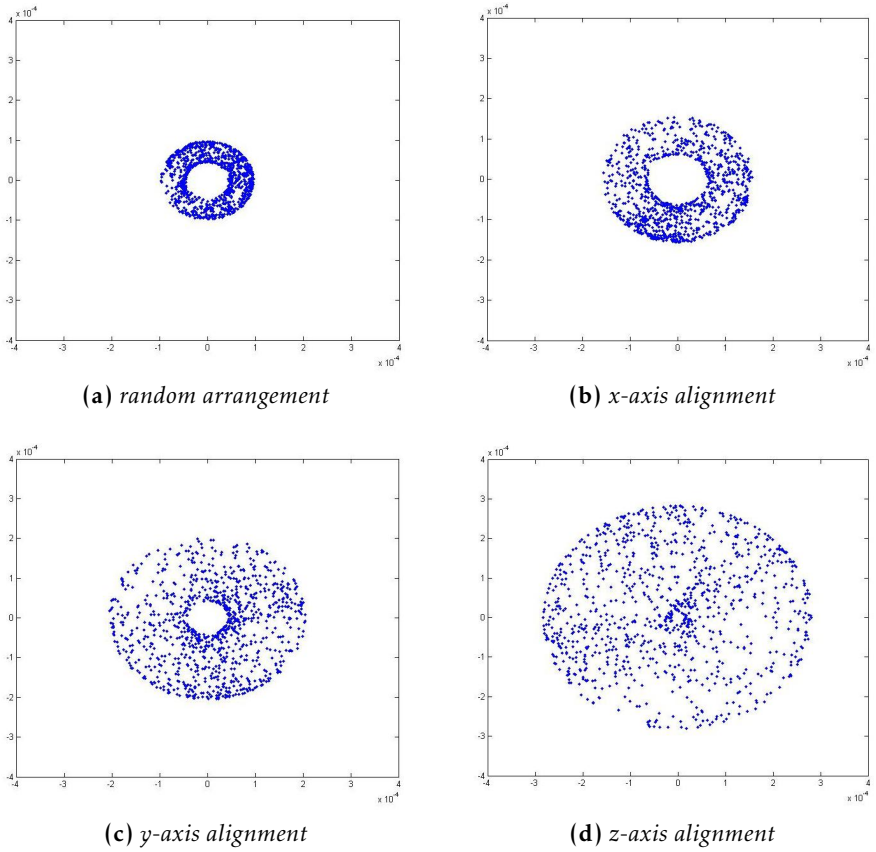

(a) *random arrangement* **(b)** *x-axis alignment*

(c) *y-axis alignment* **(d)** *z-axis alignment*

Figure 7.5: *Scattered electric field by two clusters. The patterns of electric field are similar for different type of arrangements. End points form a ring in the complex plane. However, the width of the ring is dependent on clusters' arrangement. Both clusters have moved with the same velocity and acceleration, which result to the same maximum displacement of* $150\mu m$*. (a) Random arrangement: ring with small width (b), (c) X-, Y-axis alignment: wider rings. (d) Z-axis alignment: ring with the largest width.*

the ring varies with respect to the type of clusters' arrangement inside the cloud volume. The impact of the different arrangements on the pattern of scattered electric field and the corresponding backscattered power is investigated here. For this reason, the initial positions of droplets were considered the same in all experiments below. In other words, the initial conditions before separating the droplets into 2 clusters were identical. That was necessary for taking comparable figures for the scattered electric field and the power distribution presented in Fig. 7.5 and 7.6 respectively. The droplets are split into 2 clusters but differently arranged inside the cloud volume (random arrangement, aligned with X-, Y- or Z-axis). They start moving in space towards any random direction but within the same maximum displacement of $150\mu m$. From Fig. 7.5, the pattern of scattered electric field points in the complex plane is a ring (similar to one cluster case), but the width of the ring depends on clusters' arrangement in volume. The variance around the mean value of electric field magnitude denotes the width of each ring. The widest ring appears for the Z-axis arrangement and it is illustrated in Fig. 7.5d. Indeed, the highest value for the standard deviation of electric field's magnitude shown in Table 7.1 is for the Z-axis alignment case.

The distribution of backscattered power for all types of arrangement is presented in Fig. 7.6. The several arrangements influence the mean value and the standard deviation of backscattered power and, thus, its discrepancy from incoherent power. Table 7.1 provides some statistical properties (i.e., mean, standard deviation) for the backscattered coherent power and its deviation from incoherent power. The deviation is estimated as the difference of mean value of coherent power from incoherent power. Among the introduced clusters' arrangements, the random arrangement depicted in Fig. 7.6a seems to give large deviation from incoherent power (see Table 7.1). The backscattered power for such random arrangement

appeared lower than the incoherent power, in all 1000 realisations. That was not the case for the other types of arrangements. From the p.d.f. of power in case of X-axis alignment shown in Fig. 7.6b, it is likely that coherent power is lower than incoherent power since the mean value of coherent power is approximately 11% lower than incoherent power. On the contrary, for the case of Y-axis alignment, the coherent power may have lower value than incoherent power, but most probably, coherent power is higher than incoherent power since the mean value of coherent power is 25% higher than incoherent power. The mean value of coherent power appears 165% larger than incoherent power for the case of Z-alignment. The order of discrepancy between incoherent power and mean coherent power is strongly augmented for Z-axis alignment case. That means that it is very likely that the backscattered coherent power, when clusters are aligned to Z-axis, has higher value than incoherent power. Therefore, for the introduced arrangements, the lowest discrepancy between the mean value of coherent power and incoherent power has been observed for the X-axis alignment case. Nevertheless, it can be noticed that the p.d.f. of power has the same shape regardless how clusters are arranged in space. This observation is important and will be further discussed in section 7.3.1.1.

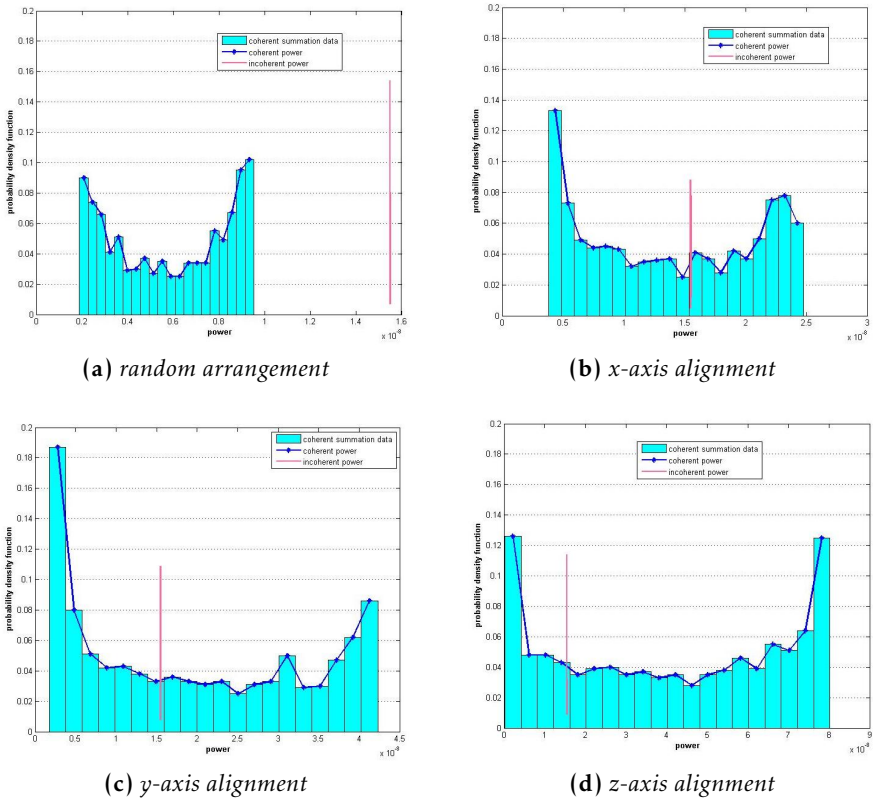

(a) *random arrangement* **(b)** *x-axis alignment*

(c) *y-axis alignment* **(d)** *z-axis alignment*

Figure 7.6: *P.d.f. of the power backscattered by two clusters. The shape of power distribution resulting from coherent summation is similar for each arrangement. However, the mean value and standard deviation of power differs for the several arrangements. Therefore, the discrepancy between mean coherent power and incoherent power depends on the arrangement. (a) Random arrangement: coherent power appears lower than incoherent power; incoherent power is* 165% *higher than the mean coherent power. (b) X-axis alignment: mean coherent power has lower value than incoherent power; their discrepancy is the lowest among all arrangements. (c) Y-axis alignment: mean coherent power has higher value than incoherent power; their discrepancy is still low. (d) Z-axis alignment: mean coherent power is much higher than incoherent power; their discrepancy is the highest among all arrangements.*

In the previous tests, each cluster was able to move in space within the same maximum displacement of $150\mu m$. However, in more realistic turbulence conditions, the clusters do not necessarily move with the same velocity and acceleration. The impact of velocity and acceleration of clusters' motion on backscattered power distribution can be studied by considering different maximum displacements for each cluster.

Table 7.1: *Comparative table for the different types of arrangement in 2 clusters case. The table provides the statistical properties for the magnitude of scattered electric field and the corresponding power. Clusters are able to move in 3-Dimensional space within the same maximum displacement of* $150\mu m$*. Power, when incoherent summation is considered, is equal to* $1.55e\text{-}08 V^2 m^{-2}$.

	Mean magnitude $[Vm^{-1}]$	Std of magnitude $[Vm^{-1}]$	Mean power $[V^2m^{-2}]$	Std of power $[V^2m^{-2}]$	Discrepancy $[V^2m^{-2}]$
Random arrangement	7.4436e-05	1.7972e-05	5.8634e-09	2.6012e-09	9.6412e-09
X-axis alignment	1.1315e-04	3.1716e-05	1.3807e-08	7.0273e-09	1.6942e-09
Y-axis alignment	1.2803e-04	5.5293e-05	1.9445e-08	1.3995e-08	-3.9488e-09
Z-axis alignment	1.8543e-04	8.2901e-05	4.1249e-08	2.7375e-08	-2.5747e-08

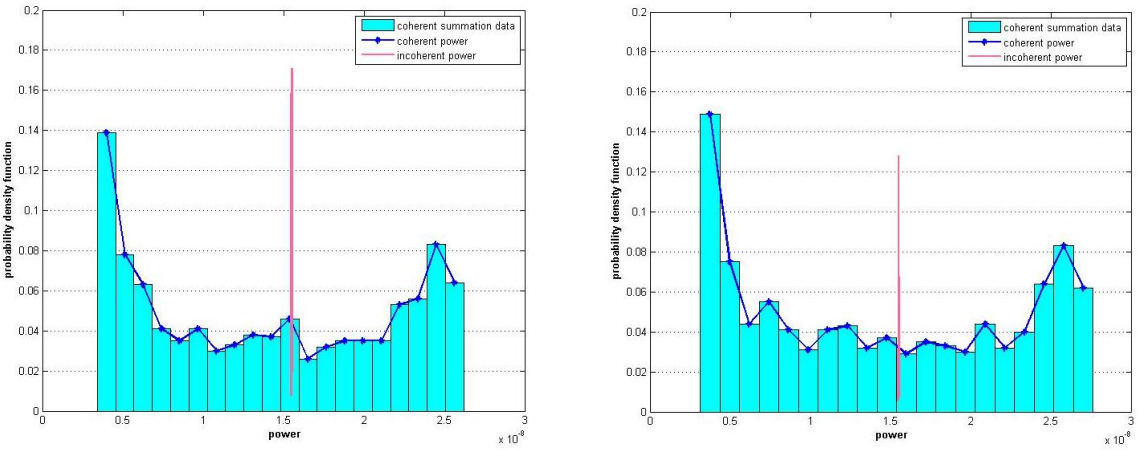

(a) $300\mu m$ *maximum displacement* **(b)** $450\mu m$ *maximum displacement*

Figure 7.7: *P.d.f. of the power backscattered by two clusters moving with different velocities and/or accelerations. Clusters are aligned parallel to X-axis. The power distribution has similar shape as in Fig. 7.6b and only the statistical properties slightly differ. (a) Second cluster moves with a maximum displacement of* $300\mu m$*: the mean value of coherent power increases; discrepancy from the incoherent power decreases by* 1% *compared to the main case {Both clusters-*$150\mu m$*}. (b) Second cluster moves with a maximum displacement of* $450\mu m$*: mean value of coherent power increases more; discrepancy from the incoherent power decreases* 3% *more, thus it appears* 4% *decreased from the main case {Both clusters-*$150\mu m$*}.*

Table 7.2: *Comparative table for different maximum displacements in 2 clusters case. The table provides the statistical properties for the magnitude of scattered electric field and the corresponding power. Clusters are aligned to X-axis and move in any random direction in 3-Dimensional space. Power, when incoherent summation is considered, is equal to 1.55e-*$08 V^2 m^{-2}$.

Cluster(s)-Displacement $[\mu m]$	Mean magnitude $[Vm^{-1}]$	Std of magnitude $[Vm^{-1}]$	Mean power $[V^2m^{-2}]$	Std of power $[V^2m^{-2}]$	Discrepancy $[V^2m^{-2}]$
Two-150	1.1315e-04	3.1716e-05	1.3807e-08	7.0273e-09	1.6942e-09
1^{st}-150, 2^{nd}-300	1.1341e-04	3.4388e-05	1.4044e-08	7.6696e-09	1.4505e-09
1^{st}-150, 2^{nd}-450	1.1435e-04	3.6698e-05	1.4421e-08	8.2618e-09	1.0911e-09

For this purpose, the droplets form two clusters in alignment with X-axis. In addition, the initial positions of droplets inside the cloud volume have been considered the same with the case of $150\mu m$ maximum displacement, so as the resulting figures can be compared with Fig. 7.6b. In particular two cases are analyzed here:

1. One cluster moves with a maximum displacement of $150\mu m$ and the other cluster moves with a double maximum displacement of $300\mu m$.

2. One cluster moves with a maximum displacement of $150\mu m$ and the other cluster moves with a triple maximum displacement of $450\mu m$.

In Fig. 7.7 , the p.d.f. of backscattered power for these two cases are illustrated. The p.d.f. in Fig. 7.7a and Fig. 7.7b, corresponding to the first and second case respectively, are similar to the p.d.f. shown in Fig. 7.6b, when both clusters can move within the same displacement of $150\mu m$. However, some slight differences in the mean value and standard deviation of power distribution have been noticed. In Table 7.2, the statistical properties for magnitude of scattered electric field and the relevant power are presented for these 2 cases. Mean value and standard deviation of magnitude of electric field increases as the maximum displacement of the second cluster increases. The same relationship applies for the mean and standard deviation of backscattered power. At the initial experiment of same maximum displacement for both clusters, the mean value of coherent power was 11% lower than incoherent power. Discrepancy between mean coherent power and incoherent power has been slightly decreased while the maximum displacement of the second cluster increased. In particular, at the experiment $\{1^{st} - 150\mu m, 2^{nd} - 450\mu m\}$ mean value of coherent power appears 7% lower than incoherent power. Hence, discrepancy has been only decreased by $11 - 7 = 4\%$. Therefore, an increase in the maximum displacement of the second cluster has negligible impact on the statistical properties and shape of coherent power distribution.

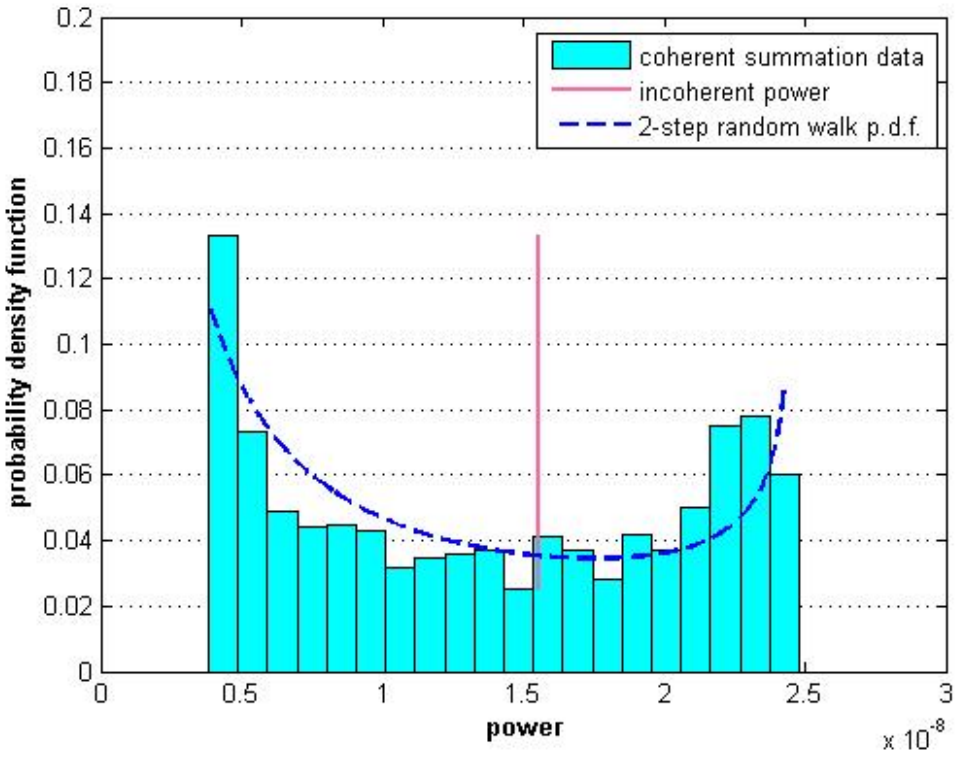

Figure 7.8: *P.d.f. of power for 2 clusters Vs. p.d.f. of distance from the origin in two-step random walk with step length* $\alpha = 1.4$. *The vertical asymptotes are the* $P = 0.4 \times 10^{-8}$ *and* $P = 2.45 \times 10^{-8}$.

7.3.1.1 Consistency with the isotropic 2-step random walk

The shape of p.d.f. of backscattered power remains the same for the two clusters case. The computational outcomes confirm that the p.d.f. of the power resulting from the coherent summation of backscattered electric fields is consistent with the probability density function of the distance from the origin $\psi_2(r)$ in an two-step isotropic Pearson's random walk over the two-dimensional phase space. The two-step random walk was previously discussed in section 4.2. However, the features of the p.d.f. of backscattered power vary for the different arrangements of clusters and for the different maximum displacements of clusters, when they have same arrangement inside the cloud volume. For instance, the vertical asymptotes for the p.d.f. in Fig. 7.6a approximately are the $P = 0.2\times10^{-8}$ and $P = 0.95\times10^{-8}$, whereas the vertical asymptotes of p.d.f. in Fig. 7.6b, 7.6c and 7.6d are $\{P = 0.4\times10^{-8},\ P = 2.45\times10^{-8}\}$, $\{P = 0.15\times10^{-8},\ P = 4.25\times10^{-8}\}$ and $\{P = 0,\ P = 8\times10^{-8}\}$ respectively. In addition, for the same type of arrangement, the p.d.f. has slightly different asymptotes when the maximum displacement of the second cluster is increased compared to the case of {Both clusters-150μm}. Thus, the vertical asymptotes of Fig. 7.7a and 7.7b are slightly displaced compared to the p.d.f. in Fig. 7.6b. In detail, the vertical asymptotes of p.d.f. in Fig 7.7a and 7.7b are approximately $\{P = 0.4\times10^{-8},\ P = 2.6\times10^{-8}\}$ and $\{P = 0.3\times10^{-8},\ P = 2.75\times10^{-8}\}$ respectively. The step length parameter α of Eq. (4.2.3) defines the exact asymptotes of the p.d.f. The consistency between the theoretical curve resulting from the theory of two-step random walk and the actual p.d.f. of power in case of 2 cluster arranged in alignment with X-axis is illustrated in Fig. 7.8. The impact of the initial conditions on the shape of p.d.f for the case of 2 clusters is investigated in Appendix II. All in all, under different initial conditions, only the scale of the p.d.f. may change but the shape will still be consistent with the 2-step random walk theory.

7.3.2 Particles distributed into three clusters

Computational tests similar to the ones for 2 clusters have been made for a lower degree of correlation, the case of 3 clusters. Initial positions of droplets are the same for all the following computational tests to investigate the impact of clusters' arrangement on the backscattered electric field and power. Clusters are able to move towards any random direction within the same maximum displacement of 150μm. The following Fig. 7.9 and 7.10 illustrate the electric field pattern and the corresponding power distribution, respectively, for all possible arrangements. The patterns for random and X-axis alignment are similar with comparable statistical properties (i.e., mean value and standard deviation) for the electric field magnitude while the pattern for Y- and Z-axis alignment occupies larger area in the complex plane (i.e., larger mean value with a larger standard deviation of the magnitude). Table 7.3 gives the statistical mean and standard deviation for magnitude of electric field. The mean electric field magnitude for the case of X-axis alignment is 15% larger than the one for the random arrangement. For the case of Y- and Z-axis alignment, the mean magnitude is about 2.5 times the magnitude of the random arrangement case. Standard deviations of magnitude for the first two arrangements (i.e., random, X-axis aligned) are almost equal, while the standard deviation of magnitude in Y- and Z-axis alignment case is respectively 2.5 and 3 times larger than any of the first two cases. Hence, the pattern of Fig. 7.9c and Fig. 7.9d looks respectively 2.5 and 3 times larger than the patterns of Fig. 7.9a and Fig. 7.9b. Therefore, clusters' arrangement affects the scattered field pattern and results to wider scattered patterns for the Y- and Z-axis alignment cases.

The p.d.f. of coherent power for the different types of arrangement are illustrated in Fig. 7.10. The power resulting from coherent summation of electric fields appears lower than the power from incoherent summation in the random arrangement case as illustrated in Fig. 7.10a. In particular, the mean value of coherent power is 63% lower than incoherent power. This is evident through the statistical properties of power distribution given in Table 7.3. For the X-axis alignment case shown in Fig. 7.10b, there is much probability that coherent power appears lower than incoherent power since, only in 60 out of the total 1000 realisations, coherent power has higher value than incoherent power. The discrepancy between mean coherent and incoherent power has been decreased to 16% for the X-axis alignment case compared to the random arrangement case. The other arrangements have resulted in higher values for the backscattered

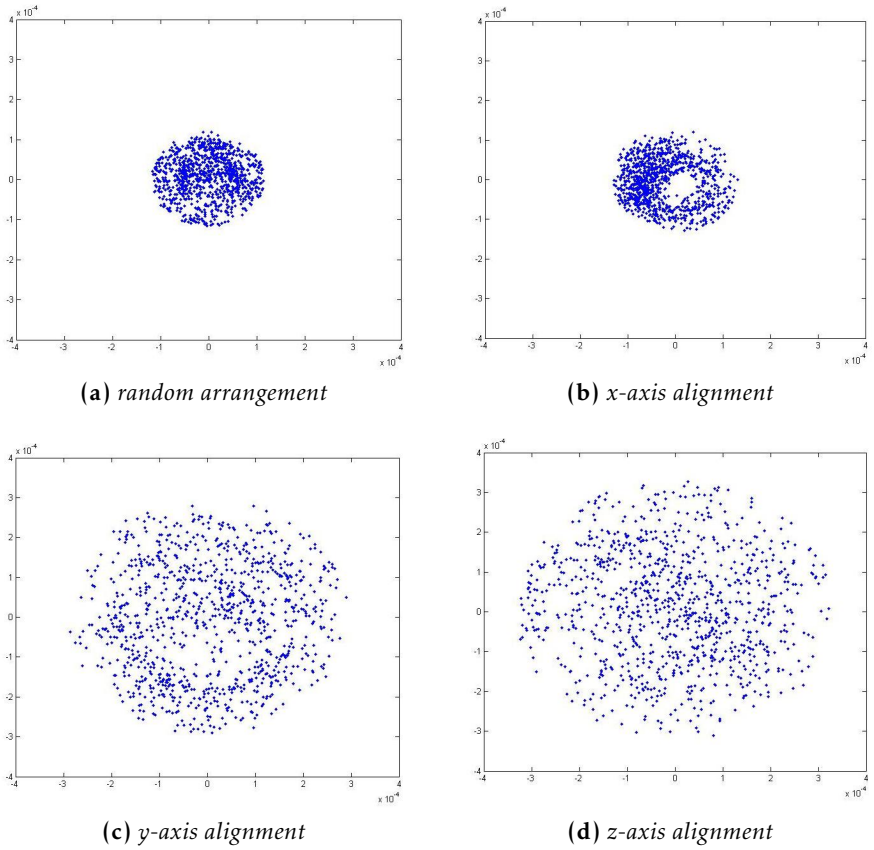

(a) *random arrangement* **(b)** *x-axis alignment*

(c) *y-axis alignment* **(d)** *z-axis alignment*

Figure 7.9: *Scattered electric field by three clusters. All clusters have been moved towards any random direction in 3-Dimensional space within the same maximum displacement of* 150μm. *(a), (b) Random arrangement, X-axis alignment: the mean value and standard deviation of electric field's magnitude have similar values. (c) Y-axis alignment: mean value and standard deviation of magnitude is about 2.5 times larger than case (b). (d) Z-axis alignment: the mean value of magnitude is 2.5 times larger than case (b) while the standard deviation is 3 times larger than case (a); this pattern occupies the largest area in the complex plane.*

coherent power. Indeed, the mean coherent power is 130% higher than the incoherent power for the Y-axis arrangement case, depicted in Fig. 7.10c. Nevertheless, the highest discrepancy is observed for the Z-axis arrangement case presented in Fig. 7.10d. For this type of arrangement, the mean power resulting by the coherent summation of individual fields is 160% higher than the expected incoherent power. In the last two arrangements (i.e., Y-, Z-axis alignment), it is likely that the coherent power has higher value than incoherent power. The characteristic shape of power p.d.f. for the cases of random arrangement, X-axis alignment and Y-axis alignment is further discussed in section 7.3.2.1. P.d.f. of power in case of Z-axis alignment has different shape. This is not a general conclusion for any test with 3 clusters aligned to Z-axis but it only refers to the specific initial conditions. Under some other initial conditions, p.d.f. of power for 3 clusters aligned to Z-axis showed consistency with the 3-step random walk. Nevertheless, it was observed that for other initial conditions, the p.d.f. of power may follow an exponential distribution from the case of 3 clusters already.

Apart from the influence of clusters' arrangement inside the cloud volume on the measured backscattered power, which was discussed above, the impact of cluster' maximum displacement on power distribution is investigated here. For these computational tests, clusters are aligned to X-axis. Initial positions of droplets are considered constant so as the results will be compared with the basic case of {Three clusters-150μm} shown in Fig. 7.10b. The following two scenarios are explored:

1. First cluster moves within a 150μm maximum displacement. Second and third cluster moves within 300μm and 450μm maximum displacement respectively.

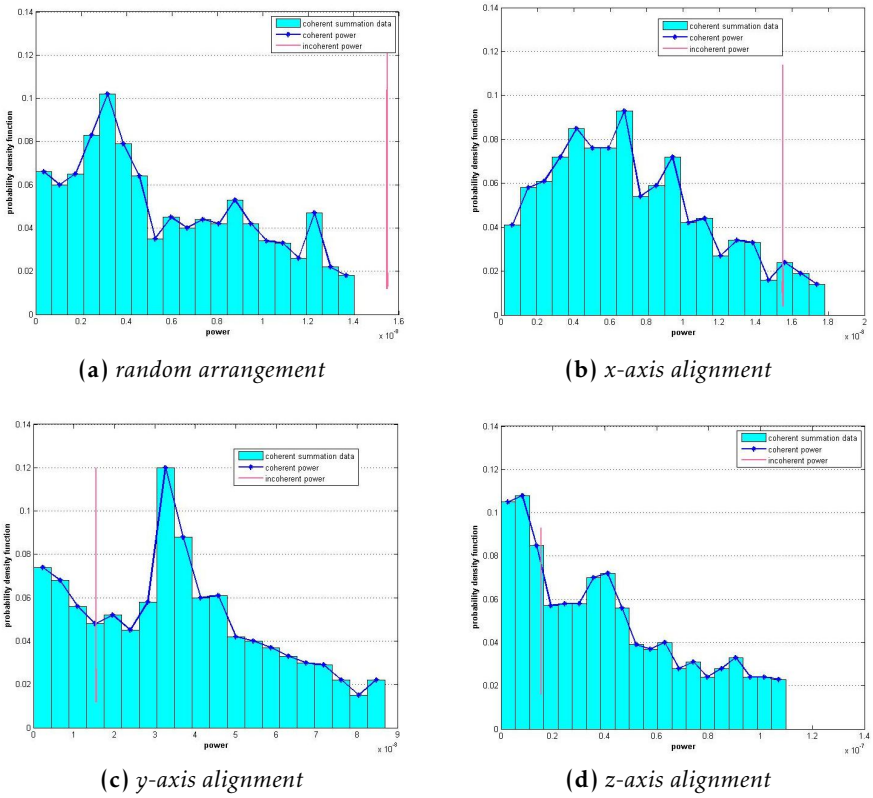

(a) *random arrangement* **(b)** *x-axis alignment*

(c) *y-axis alignment* **(d)** *z-axis alignment*

Figure 7.10: *P.d.f. of the power backscattered by three clusters. Clusters move in 3-Dimensional space within the same maximum displacement of* $150\mu m$*. (a) Random arrangement: coherent power is lower than incoherent power. (b) X-axis alignment: the mean coherent power is lower than incoherent power; their discrepancy is the lowest among the different arrangements. (c) Y-axis alignments: mean coherent power is higher than incoherent power (d) Z-axis alignment: mean coherent power is ever higher than incoherent power; their discrepancy is the highest observed among the different cases.*

2. First cluster moves within a $150\mu m$ maximum displacement. Second and third cluster moves within $450\mu m$ and $750\mu m$maximum displacement respectively.

Table 7.4 gives a comparison for the statistical properties of backscattered power in the aforementioned scenarios. The results are comparable with the initial experiment of {Three clusters-$150\mu m$} depicted in Fig. 7.10b. From the values in Table 7.4, one can conclude that the effect of displacement is negligible since the mean values of coherent power are very much the same (i.e., ∼0.7e-08) and, thus, discrepancies between mean coherent and incoherent power appear almost unchanged (i.e., around 0.8e-08) in all considered cases. The shape of power distributions for the scenarios $\{1^{st} - 150\mu m, 2^{nd} - 300\mu m, 3^{rd} - 450\mu m\}$ and $\{1^{st} - 150\mu m, 2^{nd} - 450\mu m, 3^{rd} - 750\mu m\}$ are shown in Fig. 7.11 and both shapes look pretty much the same with the one of Fig. 7.10b.

7.3.2.1 Consistency with the isotropic three-step random walk

The shape of p.d.f. of backscattered power remains the same for the three clusters case when the clusters are randomly arranged or aligned with X- or Y-axis in the cloud volume. The computational outcomes confirm that the p.d.f. of the power resulting from the coherent summation of backscattered electric fields is consistent with the probability density function of the distance from the origin $\psi_3(r)$ in an three-step isotropic Pearson's random walk over the two-dimensional phase space. The three-step random walk was discussed in section 4.2. However, even though the shape of p.d.f is always the same and consistent with Fig. 4.3, the vertical asymptote depends on the step length parameter α of Eq. (4.2.4). For instance, the vertical asymptote for the p.d.f. in Fig. 7.10a approximately is the $P = 0.3 \times 10^{-8}$, whereas the vertical

Table 7.3: *Comparative table for the different types of arrangement in 3 clusters case. The table provides the statistical properties for the magnitude and standard deviation of scattered electric field and the corresponding power. Clusters are able to move in 3-Dimensional space within the same maximum displacement of* $150\mu m$*. Power, when incoherent summation is considered, is equal to 1.55e-08*V^2m^{-2}.

	Mean magnitude $[Vm^{-1}]$	Std of magnitude $[Vm^{-1}]$	Mean power $[V^2m^{-2}]$	Std of power $[V^2m^{-2}]$	Discrepancy $[V^2m^{-2}]$
Random arrangement	7.0267e-05	2.7344e-05	5.6844e-09	3.7974e-09	9.8104e-09
X-axis alignment	8.0871e-05	2.6536e-05	7.2436e-09	4.2405e-09	8.2601e-09
Y-axis alignment	1.7658e-04	6.5722e-05	3.5497e-08	2.1933e-08	-1.9998e-08
Z-axis alignment	1.8262e-04	8.1829e-05	4.0040e-08	3.0202e-08	-2.4540e-08

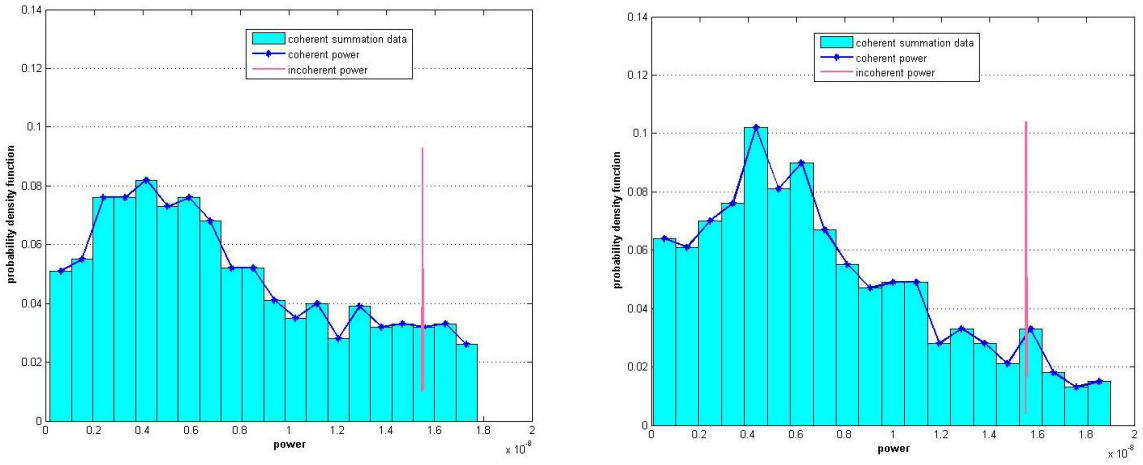

(a) $450\mu m$ *maximum displacement* **(b)** $750\mu m$ *maximum displacement*

Figure 7.11: *P.d.f of the power backscattered by three clusters moving within different displacements. Clusters are aligned parallel to X-axis. The power distribution has similar shape as in Fig. 7.10b and only the statistical properties slightly differ. (a)* $\{1^{st}-150\mu m, 2^{nd}-300\mu m, 3^{rd}-450\mu m\}$*, (b)* $\{1^{st}-150\mu m, 2^{nd}-450\mu m, 3^{rd}-750\mu m\}$*: mean value of coherent power is lower than incoherent power; the order of discrepancy remains almost constant (∼0.8e-08).*

asymptote of p.d.f. in Fig. 7.10b and Fig. 7.10c is $P = 0.6\times10^{-8}$ and $P = 3.5\times10^{-8}$ respectively. The vertical asymptote of Fig. 7.11a and Fig. 7.11b does not seem displaced in comparison with the asymptote of p.d.f. in Fig. 7.10b. Indeed, it is validated from the computational tests that the asymptote of p.d.f. for the power backscattered by three clusters when they are in alignment with X-axis is around $P = 0.6\times10^{-8}$. The consistency between the theoretical curve resulting from the theory of three-step random walk and the actual p.d.f. of power in case of 3 cluster arranged in alignment with X-axis can be identified by their illustration in Fig. 7.12. Any small discrepancy from this axis is reasonable due to the random motion that droplets undergo inside the cloud volume. Therefore, the vertical asymptote of the p.d.f. is unique (within a small margin) for constant initial conditions and same type of arrangement inside the volume. However, for random initial conditions, it is not possible to predict the asymptote for the p.d.f. of power. As a conclusion, the consistency with the theory of three-step random walk is upon the shape of p.d.f. and any conclusions about the statistical properties of power should refer to the same initial positions of cloud droplets inside the volume.

Table 7.4: *Comparative table for different maximum displacements in 3 clusters case. The table provides the statistical properties for the magnitude of scattered electric field and the corresponding power. Clusters are aligned to X-axis and more towards any random direction in 3-dimensional space. Power, when incoherent summation is considered, is equal to 1.55e-08* V^2m^{-2}.

Cluster(s)-Displacement [μm]	Mean magnitude [Vm^{-1}]	Std of magnitude [Vm^{-1}]	Mean power [V^2m^{-2}]	Std of power [V^2m^{-2}]	Discrepancy [V^2m^{-2}]
All-150	8.0871e-05	2.6536e-05	7.2436e-09	4.2405e-09	8.2601e-09
1^{st}-150 ,2^{nd}-300, 3^{rd}-450	8.1306e-05	2.9053e-05	7.4539e-09	4.7303e-09	8.0582e-09
1^{st}-150, 2^{nd}-450, 3^{rd}-750	7.9312e-05	2.9098e-05	7.1362e-09	4.6346e-09	8.3932e-09

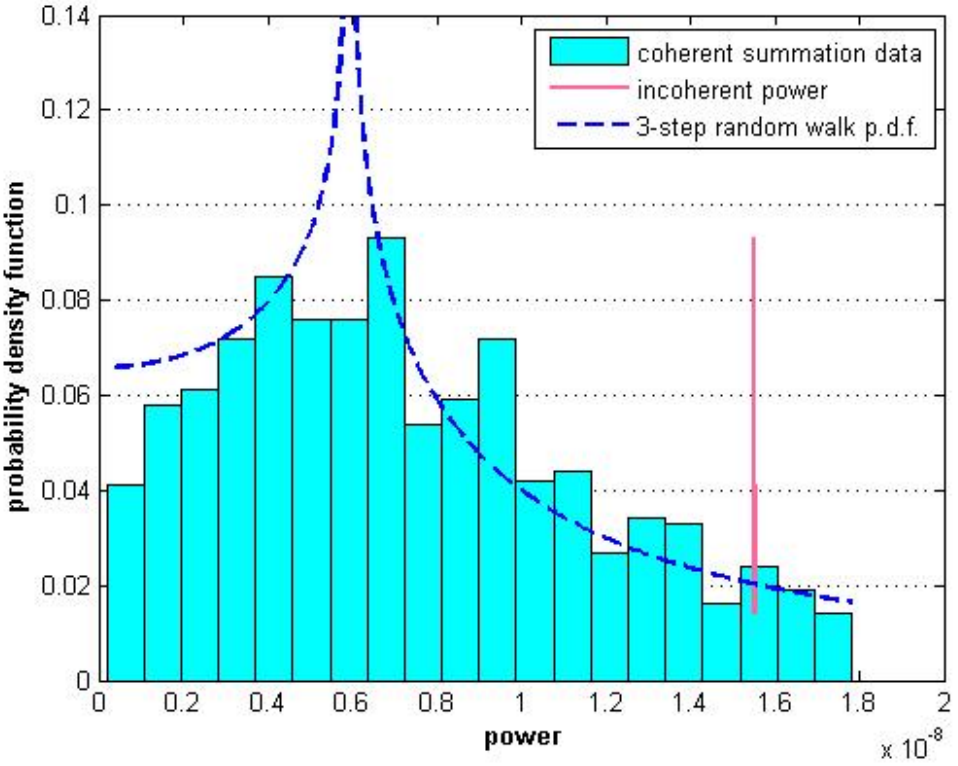

Figure 7.12: *P.d.f. of power for 3 clusters Vs. p.d.f. of distance from the origin in three-step random walk. The vertical asymptote is the* $P = 0.6 \times 10^{-8}$.

7.3.3 The impact of increasing the number of clusters

The impact of clustering on radar backscattered power has been shown for the case of n=1, 2, 3 clusters present in the cloud volume. Higher degrees of clustering, which denote lower correlation among droplets' positions, will be considered in this section. The effect of increasing the number of clusters on power distribution was explored for different initial positions of droplets. In all cases, clustering results in power distribution which deviates from the well-known exponential distribution for the uncorrelated case (i.e., absence of clustering) that was discussed in section 7.1. However, here, the initial conditions remain constant so as the statistical properties of backscattered power for the different degrees of clustering, shown

in Table 7.5, are comparable. Clusters are aligned to X-axis and move freely towards any random direction in 3-Dimensional space within a maximum displacement of $150\mu m$. Fig. 7.13 provides an illustration of the scattered power distribution when the total number of droplets N=62500 have been split into n=4, 8, 10, 13, 200, 500 clusters. In case of 4 clusters, each cluster contains 15625 droplets. For 8, 10, 13, 200, 500 clusters, each cluster contains 7813, 6250, 4808, 313, 125 droplets respectively. The power distribution resulting from a certain number of clusters is compared with the power distribution in the absence of cluster. In particular, Fig. 7.13a gives a comparison for the p.d.f. of power between the case of n=4 clusters present and the case of no cluster. Power resulting from the incoherent summation of scattered electric fields is supposed to be equal with the mean value of power when electric fields are coherently summed, and thus, the discrepancy between mean coherent and incoherent power is very low and negligible (~1.3294e-10) in the absence of clustering.

Table 7.5: *Comparative table for the different degrees of clustering. The table provides the statistical properties for the scattered power. Clusters are able to move in 3-Dimensional space within the same maximum displacement of* $150\mu m$*. The results of no clustering case are compared to the ones obtained when different number of clusters is considered. Power, when incoherent summation is considered, is equal to 1.55e-08* V^2m^{-2}.

#clusters - #droplets/cluster	Mean power $[V^2m^{-2}]$	Median power $[V^2m^{-2}]$	Std of power $[V^2m^{-2}]$	Discrepancy $[V^2m^{-2}]$
4 - 15625	1.0125e-08	8.2296e-09	7.3717e-09	5.3795e-09
8 - 7813	1.3380e-08	1.0509e-08	1.0690e-08	2.1241e-09
10 - 6250	1.6047e-08	1.1864e-08	1.4002e-08	-5.4123e-10
13 - 4808	1.2976e-08	9.1774e-09	1.2694e-08	2.5266e-09
200 - 313	1.3417e-08	9.4229e-09	1.3144e-08	2.0846e-09
500 - 125	1.5897e-08	1.2230e-08	1.3609e-08	-3.9503e-10
none - 62500	1.5369e-08	1.0547e-08	1.4620e-08	1.3294e-10

The statistical properties of power for the different degrees of clustering are analysed here. The mean value of power, when droplets are split into 4 clusters, is 35% lower than the incoherent power and, hence, almost 35% lower than the mean value of power in perfect randomness. The n=4 case gives the largest discrepancy between mean coherent power and incoherent power. However, the mean coherent power is not the only statistical property that characterises the power distribution. Thus, even if the discrepancy between coherent power and incoherent power decreases for larger number of clusters, the shape of p.d.f. differs, and hence, there is still a lot of chance that spatial correlation among droplets results to lower power than expected. This is obvious in Fig. 7.13a, 7.13b and 7.13c where the blue curve, representing the p.d.f. of power when droplets are spatially correlated, appears under the green curve of the exponential power corresponding to the perfect randomness. For the specified initial conditions and under the assumption that clusters are arranged in alignment with the X-axis, the p.d.f. of power for n=13 clusters converges to the exponential one of no cluster case. From the shape of the blue curve in Fig. 7.13d and the statistical properties of power distribution (for n=13) mentioned in Table 7.5, it is observed that the case of 62500 droplets distributed into n=13 clusters of 4808 droplets/cluster which are arranged in alignment with X-axis can be treated similarly to the case of 62500 droplets completely uncorrelated inside the cloud volume.

7.3.3.1 Convergence to the case of completely uncorrelated droplets

From the computational results discussed in section 7.3.3, it is shown that high degrees of clustering are prone to result in power distribution which is very much the same with the power scattered by completely uncorrelated droplets. The convergence to the perfect randomness case does not come at the same point

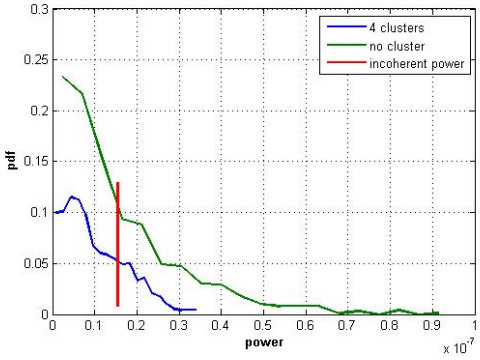

(a) *4 clusters*

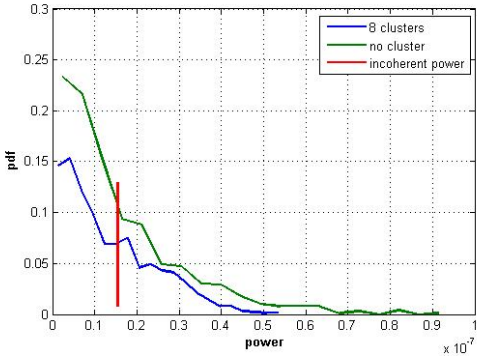

(b) *8 clusters*

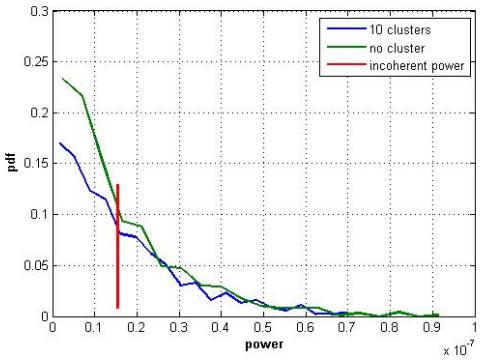

(c) *10 clusters*

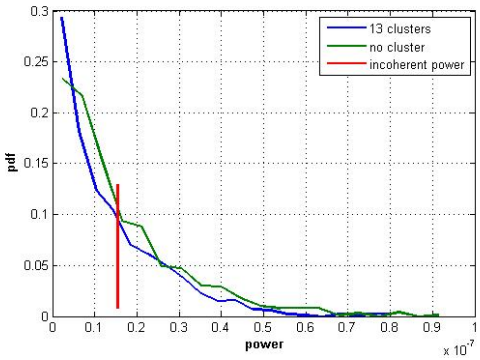

(d) *13 clusters*

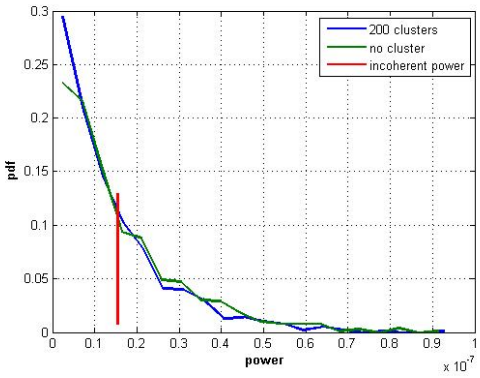

(e) *200 clusters*

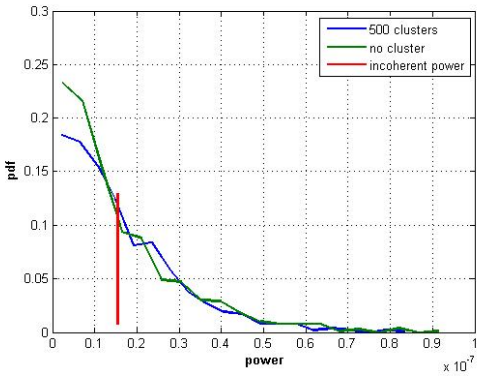

(f) *500 clusters*

Figure 7.13: *P.d.f. of backscattered power for more clusters Vs. p.d.f. for the case of uncorrelated droplets. The shape for the p.d.f. of power for n=4,8,10,13,200,500 is compared with the well-known exponential distribution of power when droplets are totally uncorrelated (i.e., no cluster case). The red line, which denotes the power resulting from incoherent summation of electric fields, lie on the mean value of the exponentially distributed power scattered by uncorrelated droplets.*

in any conditions. Therefore, even though for the initial positions of droplets considered for the computational tests of section 7.3.3, the convergence appeared for n=13 clusters when these were aligned to X-axis, this conclusion is absolutely dependent on the specific initial conditions. Hence, for different initial positions or other type of arrangement (random, Y-axis alignment, Z-axis alignment), the convergence to the case of perfect randomness may come at different degree of clustering.

As it was already mentioned before, the convergence to the case of uncorrelated droplets may occur at different degree of clustering depending on the type of arrangement and the initial conditions. For instance, in case of Z-axis alignment the clusters backscatter more power than in the other three type of arrangements. From Fig. 7.10d, one can notice that for Z-axis alignment, the power p.d.f. is already exponentially distributed from the 3 clusters case. Nevertheless, the statistical properties of power backscattered by 3 clusters differ from the properties of power in absence of clustering. All in all, convergence to the uncorrelated case will probably occur at lower degree of clustering than for the case of random, X- or Y-axis alignment.

8 Conclusions and Recommendations

The motivation of this thesis was to explore the clustering effect of turbulence which is probably responsible for the observed radar discrepancy in the case of water clouds. Aiming to understand the impact of clustering on the backscatter electric field and the relevant power, the radar illuminated cloud volume was simulated by a cube of $(5 \times 5 \times 5)cm$ filled with 62500 spheres representing the water droplets. The turbulent eddies of various spatial scale induce different types of motion. The simulated movements consider large-scale eddies, which result in horizontal, vertical or 3-dimensional displacements of clusters, and small-scale eddies which make the clusters rotate. The impact of the introduced types of motion on the backscattered electric field was investigated for the case of one cluster present inside the cloud volume.

Coherent summation of individual electric fields is considered. The contribution of each droplet's backscattered electric field in the total measured electric field at the receiver location is represented by a vector in the complex plane. This vector corresponds to one component of the electric field. The vector sum of all individual electric fields consists of a *random walk* in the 2-dimensional phase space. Thus, each snapshot gives a random walk. The end points of these random walks form the pattern of backscattered electric fields. The computational tests performed on one cluster showed that the pattern of backscattered electric field in the complex plane depends on the induced turbulence. The scale of turbulence as well as the relevant position of cluster inside the eddy implies how the cluster moves and the intensity of turbulence implies what is cluster's maximum displacement. In particular, the results showed that when cluster moves horizontally, the backscattered electric fields form a dot, a line or an arc in the complex plane depending on the maximum displacement. Patterns of backscattered electric field are similar for the vertical and 3-dimensional motion. For small maximum displacements, the end points of random walks form arcs while for larger maximum displacements, end points form rings around the origin. The width of the rings depend on the exact position of cluster inside the eddy and the intensity of eddies.

The second version of 3D motion with fixed direction can give an answer or whether the cluster moves far from the radar or closer to it. By looking into the pattern of backscattered electric field or the shape of the p.d.f. of backscattered power, the direction of motion is recognisable. In particular, when cluster moves closer to the radar, the p.d.f. of power is an ascending curve, whereas when cluster moves away from the radar, power p.d.f. has a descending trend.

For small-scale eddies comparable with the *cm*-scale of the cloud volume, rotation of cluster results

into different patterns of backscattered electric fields. The pattern depends on the position of rotation axis and maximum angular displacement, *angle of rotation*. The deterministic rotation about a fixed vertical axis result into separate points in the complex plane. The number of points is equal to the ratio $2\pi/(angle\ of\ rotation)$. For the random rotation about a vertical axis which slightly shifts between snapshots, the pattern of backscattered electric fields also consists of separate points in the complex plane but larger in number compared to the deterministic rotation. For small angular displacements, the rotation is visible in the pattern. In both rotations, the backscattered power versus the total number of snapshots is a periodic function.

After the understanding of the impact of motion on the pattern of backscattered electric field for the case of one cluster, various degrees of spatial correlation among droplets were explored. For the computational tests, the 3-dimensional motion with a maximum displacement of $150\mu m$ was considered. In the case of totally correlated particles, forming a single cluster, the p.d.f. of backscattered power is a delta dirac function in consistency with the p.d.f. of distance from the origin in a single-step Pearson's random walk in phase space. The cases of partially correlated droplets, forming 2 or 3 clusters, showed that result into different backscattered power distributions depending on the way clusters are arranged inside the cloud volume.

In 2 clusters case, the p.d.f. of backscattered power is consistent with the p.d.f. of distance from the origin in two-step Pearson's random walk in the phase space. However, even though the shape of power p.d.f. is predictable by the analytical expressions of the random walks theory, the statistical properties of backscattered power differ for the different types of arrangement. The impact of clusters' arrangement in the cloud volume on the statistics of backscattered power was investigated under the same initial positions of droplets. For instance, the mean power for the random arrangement of clusters is the lowest among the introduced four types of arrangement. On the other hand, the mean power for the Z-axis alignment case is the largest among the different arrangements. It was found that the effect of maximum displacement on power distribution is negligible.

In 3 clusters case, the shape of power p.d.f. is consistent with the p.d.f. of distance from the origin in three-step Pearson's random walk in the phase space when clusters are randomly arranged inside the cloud volume or aligned to X-axis or Y-axis. The backscattered power for Z-axis alignment is almost exponentially distributed. Under the same initial conditions, the mean value of coherent power is lower than the incoherent power for the cases of random arrangement or X-axis alignment, whilst for the Y-axis and Z-axis alignment, mean coherent power is higher than the incoherent power. The effect of maximum displacement on power distribution is negligible as in case of 2 clusters.

The high degrees of spatial correlation, for n=1,2,3 clusters present in the cloud volume, showed that there is discrepancy between the power resulting from the coherent summation of electric fields and the power resulting from the incoherent summation. The power distribution depends on the number of clusters and how these are arranged in the cloud volume. Therefore, it is very important to form a clear picture on how the clusters are arranged in cloud volume because different arrangements will most probably result into different backscattered power distributions. The impact of clustering on the backscattered power distribution was explored for higher number of clusters. Under constant initial positions of droplets, by increasing the number of clusters inside the cloud volume, the power p.d.f. converges to the well-known exponential distribution of the uncorrelated droplets case. The computational tests for the case of uncorrelated droplets showed that the magnitude of the first component of backscattered electric field follows a Gaussian distribution and, thus, the corresponding power follows an exponential distribution. The exact number of clusters, where the convergence to the non-correlation case first appears, strongly depends on the initial conditions. Here, at the computational results shown in this report, convergence occurred for 13 clusters. Nevertheless, as a general conclusion one can refer that convergence is often observed around the number of 10 clusters (i.e., sometimes convergence occurs for 9 clusters, sometimes convergence occurs for 13 clusters).

As an overall conclusion, clustering of water droplets inside the cloud volume result into backscattered power distribution which deviates from the predicted one by the standard Rayleigh incoherent scattering

theory. The observed systematic discrepancies between the mean coherent power and the mean expected incoherent power denote that the radar reflectivity sensitivity of a ground-based cloud radar may not be sufficient for detecting backscattered signals from water clouds.

Based on the aforementioned conclusions, some recommendations for future work can be proposed:

- The current scale of the cloud volume is in the order of cm^3. One suggestion would be to simulate a larger scale of the cloud volume and thus, the total number of droplets will be increased if the same concentration of 500 droplets per cm^3 is considered, which is very good approximation for liquid water clouds.

- The drop diameter used in the computational tests was constant and equal to $12\mu m$. A spectrum of drop sizes can be implemented, like a drop size distribution with a defined minimum and maximum drop diameter.

- The droplets are considered as point droplets in the model. A consideration of droplets' volume will improve the representation of droplets inside the cloud volume since the possibility of finding two droplets at a distance smaller than one drop diameter will be totally eliminated.

- The clusters have been all considered of the same size. Thus, for a total number of 62500 droplets, if 5 clusters are present in the volume, each cluster contains 12500 droplets. The model can be extended by containing clusters of different size.

- An improvement in the turbulence model to reach the Kolmogorov scale of turbulence. The existing turbulent model considers a random velocity field $\mathbf{v}(\mathbf{x},t) = \frac{d\mathbf{x}(t)}{dt}$, which results into a displacement vector:

$$\mathbf{x}(t+\Delta t) = \mathbf{x}(t) + \frac{d\mathbf{x}}{dt}\Delta t + \frac{d^2\mathbf{x}}{2dt^2}\Delta t^2. \tag{8.0.1}$$

  An improved turbulent model will consider a random force field $\mathbf{F}(\mathbf{x},t) = m\frac{d^2\mathbf{x}(t)}{dt^2}$, where m is the mass of a droplet. The turbulent model results into the following displacement vector:

$$\mathbf{x}(t+\Delta t) = \mathbf{x}(t) + \frac{\Delta t^2}{m}\Big(\mathbf{F}(\mathbf{x},t) + \mathbf{F}(\mathbf{x},t+\Delta t)\Big) + \frac{1}{2}\frac{\Delta t^2}{m}\mathbf{F}(\mathbf{x},t). \tag{8.0.2}$$

  The new turbulence model (8.0.2) is expected to simulate eddies at the Kolmogorov scaling [Jensen et al., 2008].

Bibliography

B. A. Baker. Turbulent entrainment and mixing in clouds: A new observational approach. *J. Atmos. Sci.*, 49:387–404, 1992.

P. Bartello, B. J. Devenish, J. D. Haigh, and J. C. Vassilicos. Clouds and turbulence. *Bull. Amer. Meteor. Soc.*, 91:1087–1089, 2010.

Louis J. Battan. *Radar Observation of the Atmosphere*. Chicago : University of Chicago Press, 2nd edition, 1973.

K. V. Beard. Terminal velocity and shape of cloud and precipitation drops aloft. *Journal of the Atmospheric Sciences*, 33:851–864, 1976.

P. Beckmann and A. Spizzichino. *The scattering of electromagnetic waves from rough surfaces*. Artech House Radar Library, 1st edition, 1987.

R. Boers, H. Russchenberg, J. Erkelens, V. Venema, A. van Lammeren, A. Apituley, and S. Jongen. Ground-based remote sensing of stratocumulus properties during clara, 1996. *J. Appl. Meteor.*, 39:169–181, 2000.

Encyclopaedia Britannica. atmospheric turbulence. `http://www.britannica.com/EBchecked/topic/41528/atmospheric-turbulence`, accessed April 18, 2012.

Neil V. Budko. Lectures notes on computational electromagnetics: The volume integral equation method. Laboratory of Electromagnetic Research, Faculty of Electrical Engineering, Mathematics and Computer Science, Delft University of Technology, 2005-2008.

CAA. Good aviation practice - wake turbulence. Technical report, Civil Aviation Authority of New Zealand, 2007.

E. E. Clothiaux, M. A. Miller, B. A. Albrecht, T. P. Ackerman, J. Verlinde, D. M. Babb, R. M. Peters, and W. J. Syrett. An evaluation of a 94-GHz radar for remote sensing of cloud properties. *Journal of Atmospheric and Oceanic Technology*, 12:201–229, 1995. ISSN 0739-0572.

C. Dullemond. Atmospheric turbulence and effect of observations. online material, 2011.

J. S. Erkelens, S. Jongen, H. Russchenberg, and M. Herben. Estimation of cloud droplet concentration from radar, lidar and microwave radiometer measurements. In *Proc. symp. Remote Sensing of Cloud Parameters*, 1999.

Federal Aviation Administration FAA. *The religious experience of mankind*. FAA Handbooks, 1st edition, 1975.

Thomas Foken. *Micro-meteorology*. Springer-Verlag, Berlin Heidelberg, 2008.

R. Fraile and M. Fernández-Raga. On a more consistent definition of radar reflectivity. *Atmósfera*, 22: 375–385, October 2009.

C. N. Frankin. Turbulence effects on clouds, precipitation formation and the organization of stratocumulus and shallow cumulus convection. In *9th Inter. Conf. on Southern Hemisphere Meteorology and Oceanography*, 2009.

C. N. Franklin, P. A. Vaillancourt, and M. K. Yau. Statistics and parameterizations of the effect of turbulence on the geometric collision kernel of cloud droplets. *Journal of the atmospheric sciences*, 64:938–954, June 2006.

A. S. Frisch, B. E. Martner, I. Djalalova, and M. R. Poellot. Comparison of radar/radiometer retrievals of stratus cloud liquid water content profiles with in situ measurements by aircraft. In S. R. Anderson and P. Kiparsky, editors, *Ninth ARM Science Team Meeting Proceedings*, San Antonio, Texas, 1999. Holt, Rinehart & Winston.

V. P. Ghate, B. A. Albrecht, and P. Kollias. Vertical velocity structure of non-precipitating continental boundary layer stratocumulus clouds. *J. Geophys. Res.*, 115(13), 2010.

C. M. Grinstead and J. L. Snell. *Introduction to probability*. American Mathematical Society, 2nd edition, 1997.

E. Huffman. Calculation of scattering intensities for the interaction of light with a cluster of dielectric objects. University of Washington REU Program, 2011.

Barry D. Hughes. *Random Walks and Random Environments: Random Walks (Vol.1)*. Clarendon Press, Oxford, New York, 1st edition, 1995.

Akira Ishimaru. *Wave Propagation and Scattering in Random Media*. IEEE Press, Oxford University Press, 2nd edition, 1997.

E. Jakeman and R. J. A. Tough. Non-gaussian models for the statistics of scattered waves. *Advances in Physics*, 37:5:471–529, 1988.

A. R. Jameson and A. B. Kostinski. Partially coherent backscatter in radar observations of precipitation. *J. Atmo. Sci.*, 67:1928–1946, 2009.

A. R. Jameson and A. B. Kostinski. Partially coherent backscatter in radar observations of precipitation. *Journal of the Atmospheric Sciences*, 67:1928–1946, 2010.

M. H. Jensen, K. Sneppen, and L. Angheluta. Kolmogorov scaling from random force fields. *EPL (Europhysics Letters)*, 84(1):10011, 2008.

H. Kanda. Laminar-turbulent transition: Calculation of minimum critical reynolds number in channel flow. *RIMS Kokyuroku Bessatsu B1*, pages 199–217, 2007.

P. Kollias, E. E. Clothiaux, M. A. Miller, B. A. Albrecht, G. L. Stephens, and T. P. Ackerman. Millimeter-wavelength radars: new frontier in atmospheric cloud and precipitation research. *American Meteorological Society*, 88:1608–1624, 2007.

A. N. Kolmogorov. The local structure of turbulence in incompressible viscous fluid for very large reynolds numbers. In *Series A - Mathematical and Physical Sciences*, volume 434, pages 9–13, London, 1991. Proceedings Royal Society.

A. V. Korolev, G. A. Isaac, J. W. Strapp, and A. N. Nevzorov. In situ measurements of effective diameter and effective droplet number concentration. *Journal of Geophysical Research*, 104:3993–4003, 1999.

A. B. Kostinski and A. R. Jameson. On the spatial distribution of cloud particles. *Journal of the atmospheric sciences*, 57(7):901–915, April 2000.

A. B. Kostinski and R. A. Shaw. Scale-dependent droplet clustering in turbulent clouds. *J. Fluid Mech.*, 434: 389–398, 2001.

A. S. Koziol and H. G. Leighton. The effect of turbulence on the collision rates of small cloud drops. *Journal of the Atmospheric Sciences*, 53(13):1910–1920, 1996.

L. D. Landau, E. M. Lifshits, and L. P. Pitaevskii. *Statistical physics*. Pergamon Press, 1st edition, 1980.

H. J. Liebe, G. A. Hufford, and T. Manabe. A model for the complex permittivity of water at frequencies below 1thz. *International Journal of Infrared and Millimeter Waves*, 12(7):659–675, 1991.

E. Linacre and B. Geerts. Cloud liquid water content, drop sizes and number of droplets. `http://www-das.uwyo.edu/~geerts/cwx/notes/chap08/moist_cloud.html`, 1999. retrieved 2012/04/01.

Keigo Matsuda, Ryo Onishi, Ryoichi Kurose, and Satoru Komori. Turbulence effect on radiative transfer in clouds. Technical report, Kyoto University, Japan Agency for Marine-Earth Science and Technology, Japan, 2011.

B. Mayer, M. Schröder, R. Preusker, and L. Schüller. Remote sensing of water cloud droplet size distributions using the backscatter glory: a case study. *Atmospheric Chemistry and Physics*, 4(5):1255–1263, 2004. doi: 10.5194/acp-4-1255-2004. URL `http://www.atmos-chem-phys.net/4/1255/2004/`.

Peter Meischner. *Weather radar: principles and advanced applications*. Springer, 2004.

K. Moran, S. Pezoa, C. Fairall, C. Williams, T. Ayers, A. Brewer, S. de Szoeke, and V. Ghate. A motion-stabilized w-band radar for shipboard observations of marine boundary-layer clouds. *Boundary-Layer Meteorology*, 143:3–24, 2012. ISSN 0006-8314. URL `http://dx.doi.org/10.1007/s10546-011-9674-5`. 10.1007/s10546-011-9674-5.

N. Nguyen and S. T. Wereley. *Fundamentals and applications of microfluidics*. ARTECH HOUSE, 2002.

M. K. Ochi. *Applied Probability and Stochastic Processes*. Wiley-Interscience, 1st edition, 1990.

A. Overeem. Verification of clear-air turbulence forecast. Technical report, Royal Netherlands Meteorological Institute (KNMI), 2002.

Athanasios Papoulis. *McGraw Hill Series in Systems Science: Probability, Random Variables and Stochastic Processes*. McGraw-Hill Book Company, 1st edition, 1965.

M. B. Pinsky and A. P. Khain. Turbulence effects on droplet growth and size distribution in clouds - a review. *J. Aerosol Sci.*, 28(7):1177–1214, 1997.

A. Protat, C. Tinel, and J. Testud. Dynamic properties of clouds and dynamic/ microphysical interactions from 94GHz cloud radar and lidar. In *Proceedings of ERAD*, pages 155–160, 2002.

M. Quante. The role of clouds in the climate system. *Journal de Physique Iv*, 121:61–86, 2004.

F. Reif. *Fundamental of Statistical and Thermal Physics*. MA: McGraw-Hill, Boston, 1st edition, 1980.

James Reynolds. The hidden dangers of mountain wave turbulence. Technical report, National Oceanic and Atmospheric Administration's National Weather Service, 2011.

R. R. Rogers. *A short course in cloud physics*. Pergamon Press, 2nd edition, 1979.

H. Russchenberg, U. Löhnert, C. Brandau, and K. Ebell. Radar scattering by stratocumulus: often much lower than expected. Why? Technical report, Delft University of Technology, Institut für Geophysik und Meteorologie, Universität zu Köln, 2009.

R. A. Shaw, A. B. Kostinski, and M. L. Larsen. Towards quantifying droplet clustering in clouds. *Q. J. R. Meteorol. Soc.*, 128:1043–1057, 2002.

Raymond A. Shaw. Particle-turbulence interactions in atmospheric clouds. Technical report, Department of Physics, Michigan Technological University, Houghton, Michigan, 2003.

Susan Stellin. The inevitability of bumps. *The New York Times*, 2007.

J. W. Telford. A new aspect of coalescence theory. *Journal of Meteorology*, 12:436–444, 1955.

V. P. Tishkovets, E. V. Petrova, and M. I. Mishchenko. Scattering of electromagnetic waves by ensembles of particles and discrete random media. *J QUANT SPECTROSC RA.*, 112:2095–2127, 2011.

M. Tokuno. Operational system for extracting cloud motion and water vapor motion winds from gms-5 image data. In *Third International Winds Workshop*, 1996.

Leung Tsang and Kung-Hau Ding. *Scattering of electromagnetic waves: Theories and Applications*. John Wiley Sons, Inc., 1st edition, 2000.

D. D. Turner, A. M. Vogelmann, R. T. Austin, J. C. Barnard, K. Cady-Pereira, J. C. Chiu, S. A. Clough, C. Flynn, M. M. Khaiyer, J. Liljegren, K. Johnson, B. Lin, C. Long, A. Marshak, S. Y. Matrosov, S. A. McFarlane, M. Miller, Q. Min, P. Minnis, W. O' Hirok, Z. Wang, and W. Wiscombe. Thin liquid water clouds: Their importance and our challenge. *American Meteorological Society*, 88:177–190, 2007.

Victor K. C. Venema. *Cloud measurements with radar*. PhD thesis, Delft University of Technology, 2000.

J. Wallace and P. Hobbs. *Atmospheric Science: An Introductory Survey*. Elsevier Academic Press, Amsterdam, 2nd edition, 2006.

Zhien Wang and Kenneth Sassen. Cloud type and macrophysical property retrieval using multiple remote sensors. *Journal of Applied Meteorology*, 40:1665–1681, 2001.

Markus Weber. A parameterization for the turbulent fluxes over melting surfaces derived from eddy correlation measurements. In *Proceedings Alpine * Snow * Workshop, National Park Berchtesgaden, Research Report 53*, pages 138–149, 2007.

APPENDIX I: RADAR REFLECTIVITY FACTOR

The reflectivity factor Z of a unit volume containing particles is estimated from the received power P_r. The meteorological radar equation gives a mathematical expression for the averaged power measured by the receive antenna [Fraile and Fernández-Raga, 2009]:

$$P_r = C\frac{\eta}{L^2 r^2}, \tag{A-1}$$

where,

C ..... is the constant related to technical specifications of the radar,
L ..... is the attenuation factor between the radar and the target (dependent on the propagation conditions),
r ..... is the radar resolution volume center,
η ..... is the scattering cross section per unit volume (dependent on the number of scatterers inside the cloud volume).

$$\eta = \frac{\pi^5}{\lambda^4}|K|^2 Z, \tag{A-2}$$

where,

$|K|^2$ ..... is a constant related to the relative permittivity of particles (equal to 0.93 for water).

Under the Rayleigh approximation (i.e., drop diameter much smaller compared to the operational wavelength λ), the reflectivity factor depends only on the number of scatterers and their sizes. It is analytically expressed by the continuous form:

$$Z = \int_{D_{min}}^{D_{max}} n(D)D^6 \mathrm{d}D, \tag{A-3}$$

where,

$n(D)$ ..... is the drop-size distribution per unit volume,
D_{min} ..... is the minimum diameter in the unit volume,
D_{max} ..... is the maximum diameter in the unit volume.

By convention, the reflectivity factor is measured in $mm^6 m^{-3}$ since it represents the scattering cross section of the hydrometeors present in one cubic meter. Due to the large dynamic range of observed reflectivity factors, logarithmic units ($dBZ = 10\log[Z/(mm^6 m^{-3}]$) are mostly used [Meischner, 2004].

APPENDIX II: Additional results

In this appendix, some additional computational results are presented as a try to answer the following questions:

1. What would be different if the second or third component instead of the first component of backscattered electric field was shown in the complex plane?
2. What would be different if the computational tests of Chapter 6 had been performed under the same initial conditions?
3. What would be different if the computational tests of 2 clusters case in Chapter 7 had been performed under random initial conditions?

What would be different if the second or third component instead of the first component of backscattered electric field was shown in the complex plane? For the illustration of the electric field patterns, only the first component was shown in the figures of Chapters 6 and 7. The reason is that the first component of electric field is the one which contributes mostly in the total scattered electric field. The amplitude of the other two components is much smaller compared to the amplitude of the first component. However, the patterns of end points remain the same for any electric field's component. Indeed, from Fig. 1 the end points for the second and third component of backscattered electric field result into similar patterns. The computational tests refer to the case of one cluster moving towards any direction in space and thus the results can be compared with the ones shown in Fig. 6.3. For small maximum displacement (i.e., $6\mu m$), end points for the second and third component form arcs in the complex plane. For larger maximum displacement, the backscattered electric fields result into rings which their width depends on the maximum displacement, exactly as in the pattern for the first component of total backscattered electric field. Nevertheless, one should observe the difference in the magnitude among the several components of scattered electric field. The magnitude of the first component is in the order of 10^{-4}, while the magnitude of second and third component is in the order of 10^{-10} and 10^{-7} respectively. The low values of magnitude of the second and third component compared to the first component validate the statement that spherical droplets do not change the polarization of incident electric field.

Table 1: *Comparative table for the different types of arrangement in 2 clusters case for other initial conditions. The table provides the statistical properties for the magnitude of scattered electric field and the corresponding power. Clusters are able to move in 3-Dimensional space within the same maximum displacement of* $150\mu m$*. Power, when incoherent summation is considered, is equal to 1.55e-08* V^2m^{-2}*.*

	Mean magnitude $[Vm^{-1}]$	Std of magnitude $[Vm^{-1}]$	Mean power $[V^2m^{-2}]$	Std of power $[V^2m^{-2}]$	Discrepancy $[V^2m^{-2}]$
Random arrangement	1.2912e-04	3.5872e-05	1.7958e-08	9.0582e-09	-2.4499e-09
X-axis alignment	1.2113e-04	4.5560e-05	1.6746e-08	1.0219e-08	-1.2436e-09
Y-axis alignment	1.4131e-04	4.4791e-05	2.1972e-08	1.1298e-08	-6.4746e-09
Z-axis alignment	2.6360e-04	9.4159e-05	7.8343e-08	4.6987e-08	-6.2845e-08

What would be different if the computational tests of Chapter 6 had been performed under the same initial conditions? In Chapter 6, the initial positions of droplets inside the cloud volume were not the same in the tests. This is the reason why any comparison between the intensities of backscattered electric fields for several maximum displacements is not valid. Such a comparison can be made if the initial conditions are constant for the computational tests. The impact of the initial conditions on the results was investigated for the case of one cluster moving in 3-dimensional space. The tests for several maximum displacements have been performed under the same initial conditions. The initial conditions have no impact on the shape of the pattern of backscattered electric field but only affect the scale of the pattern, thus the magnitude of the backscattered electric field. As it can be noticed in Fig. 2a where the same maximum displacements as in Fig. 6.3 were tried for the case of 3D motion of a cluster towards any random direction in space, the backscattered points for $6\mu m$ maximum displacement, which form an arc in the complex plane, are also part of the rings which are formed when the cluster can move within a maximum displacement of $100\mu m$, $450\mu m$ or $1.5mm$. The same maximum displacements were used for performing the computational tests of one cluster's 3D motion towards fixed direction, so as the patterns of Fig. 2b can be compared with the patterns in Fig. 6.4. For small maximum displacement (i.e., $6\mu m$) the end points of scattered electric field in the complex plane, forming a ring, are also part of the wider rings which are formed when the cluster can move within a maximum displacement of $100\mu m$ or $450\mu m$. Therefore, when the initial conditions remain the same, the end points of the total backscattered electric field in the complex plane for the different maximum displacements. The width of the rings increases while the maximum displacement increases. Therefore, the maximum displacement affects the standard deviation of the backscattered electric field magnitude.

What would be different if the computational tests of 2 clusters case in Chapter 7 had been performed under random initial conditions? By considering initial conditions different from the ones in Fig. 7.5, the pattern of backscattered electric field is illustrated in Fig. 3. The shape of the patterns has not changed since the end points still form rings. However, the scale of backscattered electric field may vary. For instance, in the random arrangement case, the pattern shown in Fig. 4a occupies more space in the complex plane than the pattern of Fig. 7.5a which was produced under different initial conditions. From the patterns of Fig. 3, it is observed that the pattern corresponding to the random arrangement occupies the smallest space, the patterns for X-axis and Y-axis alignments occupy comparable[1] space and the pattern for Z-axis alignment occupies the largest space in the complex plane. The proportion of space occupied by the patterns for the different arrangements can be also seen from the p.d.f. of backscattered power in Fig. 4. Indeed, the standard deviation of power for the random arrangement case is the lowest, the highest

[1] pattern in Y-axis alignment case is slightly increased compared to the pattern in X-axis alignment case

standard deviation of power appears for the Z-axis alignment and the standard deviations of power for the X-axis and Y-axis alignment have values somewhere in between the other two. Therefore, in the case of 2 clusters, the impact of initial conditions on the backscattered power is only a possible change in scale but not in the shape, since this is always described by the analytical expressions of the walker's position p.d.f. in 2-step random walk.

However, the impact of initial conditions on the pattern of backscattered electric field and the p.d.f. of power for the 3 clusters case is not only a change in the scale of the pattern or the range of the power p.d.f. It was observed that under some initial conditions, the consistency of power p.d.f. with the 3-step random walk is violated and the p.d.f. converges directly to the exponential distribution. This is mostly the case for the Z-axis alignment. Therefore, it is very important to form a clear picture on how the clusters are arranged in cloud volume because different arrangements will probably result into different backscattered power distributions.

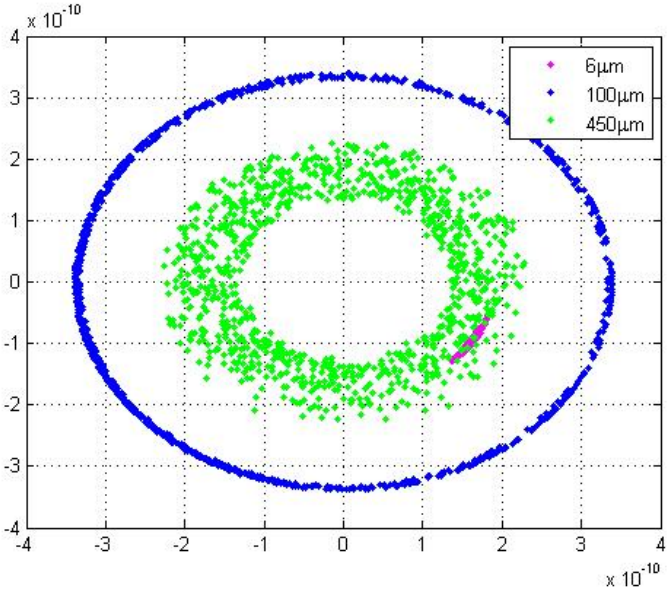

(a) *second component*

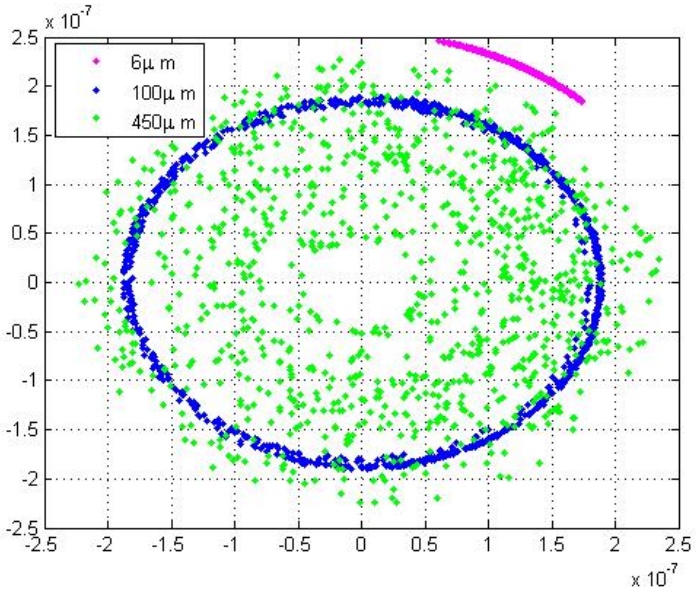

(b) *third component*

Figure 1: *Pattern for the second and third component of backscattered electric field. For small maximum displacement (i.e., 6μm) points for the second and third component form arcs in the complex plane. For larger maximum displacement, the backscattered electric field result into rings which their width depends on the maximum displacement, exactly as in the pattern of the electric field's first component.*

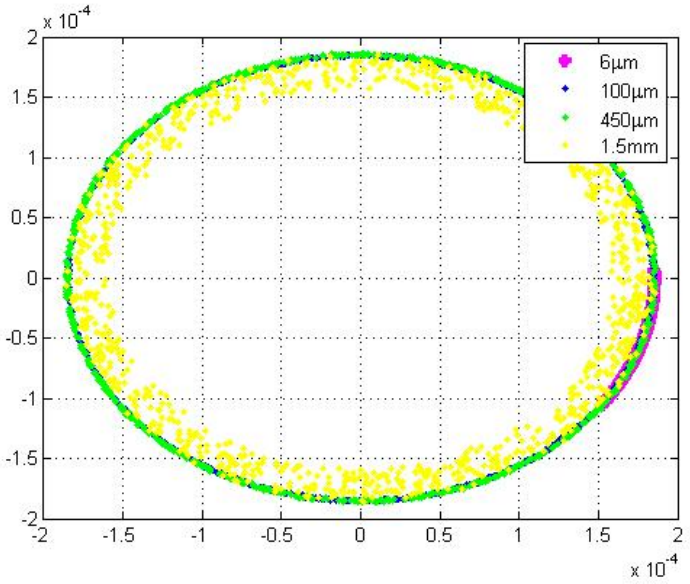

(a) *3D motion, random direction*

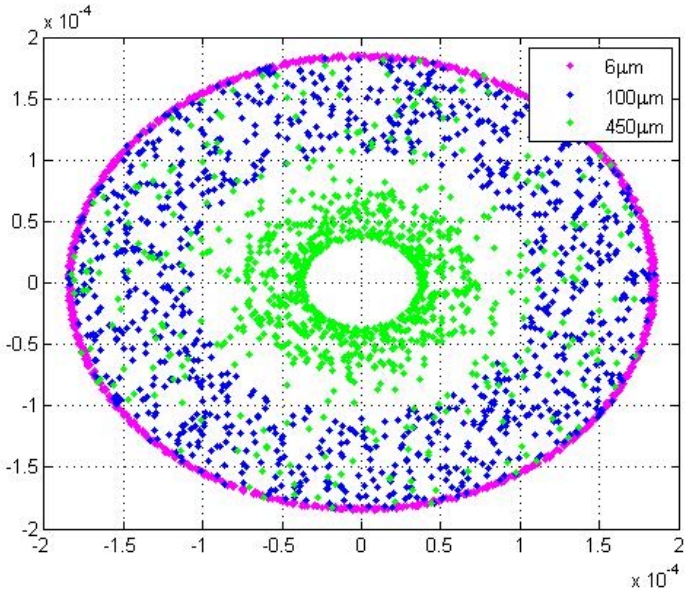

(b) *3D motion, fixed direction*

Figure 2: *Pattern for the first component of backscattered electric field when initial conditions are constant for the computational tests. If the initial conditions remain the same, the end points for the different maximum displacements overlap. (a) For small maximum displacement (i.e., 6μm) the end points of scattered electric field in the complex plane, forming an arc, are also part of the rings which are formed when the cluster can move within a maximum displacement of* $100\mu m$, $450\mu m$ *or* $1.5mm$. *(b) For small maximum displacement (i.e.,* $6\mu m$*) the end points of scattered electric field in the complex plane, forming a ring, are also part of the wider rings which are formed when the cluster can move within a maximum displacement of* $100\mu m$ *or* $450\mu m$.

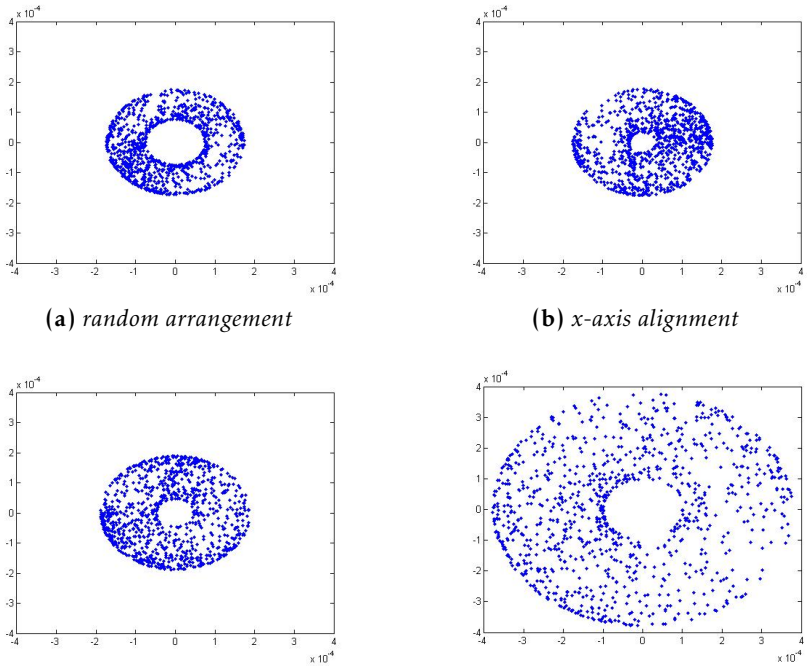

(a) *random arrangement* **(b)** *x-axis alignment*

(c) *y-axis alignment* **(d)** *z-axis alignment*

Figure 3: *Scattered electric field by two clusters for other initial conditions. The patterns of electric field are similar to patterns of Fig. 7.5. The initial conditions can only change the scale of the pattern for 2 clusters case but not the shape.*

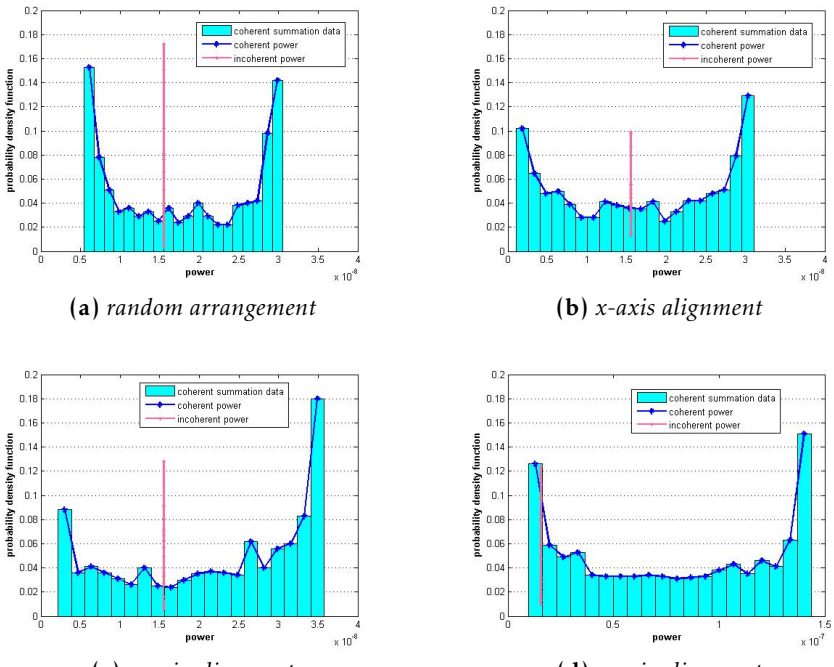

(a) *random arrangement* **(b)** *x-axis alignment*

(c) *y-axis alignment* **(d)** *z-axis alignment*

Figure 4: *P.d.f. of the power backscattered by two clusters for other initial conditions. The shape of power distribution resulting from coherent summation is similar for any initial conditions. However, the statistical properties of power, like the mean value and the standard deviation, may vary for different initial conditions.*